Dipl.-Ing. Dilek Halici

Damage analysis in a gamma TiAl alloy during hot working

DOCTORAL THESIS

to achieve the university degree of

Doktor der technischen Wissenschaften

submitted to

Graz University of Technology

Supervisor

Assoc. Prof. Dr. techn. Cecilia Poletti

Institute of Materials Science and Welding

Graz, August 2015

Contents

AFFIDAVIT

I declare that I have authored this thesis independently, that I have not used other than the declared sources/resources, and that I have explicitly indicated all material which has been quoted either literally or by content from the sources used. The text document uploaded to TUGRAZonline is identical to the present doctoral thesis.

Date   **Signature**

Acknowledgements

This work is dedicated to the memory of my grandpa Ömer Faruk Halici.

Abstract

Intermetallic γ-TiAl are attractive materials for high temperature applications in aerospace as well as in automotive industries. The advantages of the 3rd generation materials are their high specific strength together with a high oxidation- and corrosion resistance up to 750°C. Their disadvantages are their limited ductility and low fracture toughness. On the other hand, hot forming of titanium aluminides is characterised by ductile damage and a narrow processing window.

The hot deformation behaviour of a TNM alloy has been analysed in this study. Hot compression tests and heat treatments on lab-scale were carried out by the thermomechanical simulator Gleeble®3800. Metallographic analysis of the material was performed by means of light optical and scanning electron microscopy and electron backscatter diffraction. The hot deformation behaviour of the alloy was modelled under different processing conditions based on experimental flow curves. Microstructural investigations were used to describe and model the softening behaviour of the studied alloy after hot deformation.

It was proved that the softening of the material was provoked by discontinuous dynamic recrystallisation of the γ phase, self-heating, dynamic phase transformations and flow localisation. Flow localisation produced wedge cracks, pores, kinked lamellae and shear bands. Stable flow behaviour at high temperatures was due to the restoration processes such as dynamic recovery of the β and α phases.

Processing maps based on dynamic material models were produced to discuss and critically scrutinise their physical meaning and to compare their predictions with other models. The dissipation efficiency of Prasad η_P is interpretable in the same way as the strain rate sensitivity parameter m, because it is related to m. The predictions by m and η_P were in good agreement with the microstructural observations. High m and η_P values characterise thermally activated processes such as dynamic recrystallisation, recovery and phase transformations.

The predictions of flow instabilities were made comparing dynamic material models, flow localisation parameter α_{SJ}, strain rate sensitivity m and macromechanical damage models. The instability criterions based on dynamic material models could not sufficiently predict the observed instabilities produced during hot deformation. In contrast to the dynamic material models m, α_{SJ} and the macromechanical damage models predicted well the instabilities in the material.

Kurzfassung

Intermetallische γ-TiAl sind attraktive Materialien für Hochtemperaturanwendungen in der Luft- und Automobilindustrie. Die Vorteile dieser Materialien der 3. Generation sind ihre hohe spezifische Festigkeit in Kombination mit einer hohen Oxidations- und Korrosionsbeständigkeit bis zu einer Temperatur von 750°C. Ihre Nachteile sind limitierte Duktilität und niedrige Bruchzähigkeit. Zusätzlich ist die Warmverformung von Titanaluminiden durch duktile Schädigung und ein enges Verformungsfenster charakterisiert.

Das Warmverformungsverhalten der TNM Legierung wurde im Rahmen dieser Arbeit untersucht. Die Druckversuche und Wärmebehandlungen im Labormaßstab wurden mit dem thermomechanischen Simulator Gleeble®3800 durchgeführt. Für die metallographische Analyse des Materials wurde Licht- und Rasterelektronenmikroskopie sowie Elektronenbeugung im Rasterelektronenmikroskop verwendet. Basierend auf den erhaltenen Fließkurven konnte das Warmverformungsverhalten unter verschiedenen Prozessbedingungen analysiert werden. Die Gefügeuntersuchungen wurden herangezogen, um das Entfestigungsverhalten der analysierten Legierung nach der Warmverformung zu beschreiben und zu modellieren.

Es konnte bewiesen werden, dass das Entfestigungsverhalten des Materials durch diskontinuierliche dynamische Rekristallisation der γ Phase, adiabate Erwärmung, dynamische Phasenumwandlungen und Fließlokalisierung verursacht wurde. Die Fließlokalisierung produziert keilförmige Risse, Poren, geknickte Lamellen und Scherbänder. Stabiles Fließverhalten trat bei hohen Temperaturen durch Restorationsprozesse wie dynamische Erholung der β und α Phase auf.

Auf dynamischen Materialmodellen basierende „processing maps" wurden berechnet um ihre physikalische Bedeutung und ihre Voraussagen mit anderen Modellen zu vergleichen. Die Dissipationseffizienz η_P nach Prasad ist vergleichbar mit dem Dehnratenempfindlichkeitsparameter m, da η_P auf m basiert. Die Voraussagen, welche mit Hilfe von m und η_P getroffen wurden, sind in guter Übereinstimmung mit den mikrostrukturellen Beobachtungen. Hohe m und η_P Werte sind charakteristisch für thermisch aktivierte Prozesse, wie dynamische Rekristallisation, Erholung und Phasenumwandlungen.

Die Voraussagen der Fließinstabilitäten wurden an Hand von dynamischen Materialmodellen, dem Fließlokalisierungsparameter α_{SJ}, Dehnratenempfindlichkeitsparameter m und makromechanischen Schädigungsmodellen, durchgeführt. Die Instabilitätsmodelle nach den dynamischen Materialmodellen konnten die beobachteten Instabilitäten jedoch nicht gut voraussagen. Im Gegensatz dazu konnten m, α_{SJ} und die makromechanischen Schädigungsmodelle die Fließinstabilitäten besser voraussagen.

Abbreviations and Symbols

Abbreviation	Meaning
bcc	Body centred cubic
BSE	Backscatter electron mode
cDRX	Continuous dynamic recrystallisation
CI	Confidence index
dDRX	Discontinuous dynamic recrystallisation
DP	Duplex microstructure
DMM	Dynamic material model
DRV	Dynamic recovery
DRX	Dynamic recrystallisation
EBSD	Electron backscatter diffraction
EDM	Electron discharge machining
EDS	Energy dispersive spectroscopy
fcc	Face centred cubic
fct	Face centred tetragonal
FEG-SEM	Field emission gun scanning electron microscope
FEM	Finite element method
FL	Fully lamellar microstructure
gDRX	Geometric dynamic recrystallisation
HAGB	High angle grain boundary
HIP	Hot isostatic pressing
IPF	Inverse pole figure
IQ	Image quality
JC	Johnson Cook
LAGB	Low angle grain boundary
LOM	Light optical microscopy
MCU	Mobile conversion unit
NG	Near gamma microstructure
NL	Nearly lamellar microstructure
OIM	Orientation imaging microscopy
PAM	Plasma arc melting
PID	Proportional-integral-derivative
SEM	Scanning electron microscopy

SFE	Stacking fault energy
TANH	Hyperbolic tangent model
TNM	3rd generation γ-TiAl based alloys with Nb, Mo and B
TZM	Titanium zirconium molybdenum anvils
VAR	Vacuum arc melted
VIM	Vacuum induction melting
XCT	X-ray computed tomography

Symbol	Meaning	Units
A	Cross-sectional area	mm^2
A_0	Initial cross-sectional area	mm^2
A_1	Yield strength (JC model)	MPa
B	Hardening modulus (JC model)	MPa
C	Strain rate sensitivity coefficient (JC model)	-
D	Ductile damage	-
D_c	Critical damage	-
d	Diameter	mm
d_0	Initial diameter	mm
E_{app}	Apparent Youngs modulus	GPa
fs	Frictional stress	MPa
k	Shear yield stress	MPa
l	Length	mm
l_0	Initial length	mm
m_s	Shear friction factor	
T_{eu}	Eutectoid temperature	°C
T_γ	Gamma solvus temperature	°C
T_m	Melting temperature	°C
T_r	Room temperature	°C
α	Disordered hexagonal TiAl phase	-
$α_2$	Ordered hexagonal TiAl phase	-
$α_{SJ}$	Flow localisation parameter (Semiatin and Jonas)	-
β	Bcc disordered TiAl phase	-
$β_o$	Bcc ordered TiAl phase	-
γ	Tetragonal TiAl phase	-
γ'	Softening parameter (Semiatin and Jonas)	-
$γ_H$	Instability criterion (Hart)	-

ΔT	Temperature increment	°C
ε	Plastic true strain	-
ε_c	Critical plastic true strain	-
$\bar{\varepsilon}_f$	Fracture true strain	-
$\dot{\varepsilon}$	Strain rate	1/s
η	Taylor-Quinney parameter	
η_P	Coefficient of dissipation efficiency (Prasad)	-
η_{MR}	Coefficient of dissipation efficiency (Murty and Rao)	-
K	Instability parameter (Murty and Rao)	-
K_j	Instability parameter (Poletti)	-
ξ	Instability parameter (Prasad)	-
σ	Flow stress	MPa
$\sigma_{1,2,3}$	Principal stress components	MPa
σ_H	Hydrostatic flow stress	MPa
σ^H	Flow stress of uncorrected flow curve	MPa

1 Introduction

Intermetallic γ-TiAl based alloys are high-temperature materials for light-weight applications in aerospace and automotive industries. These alloys have the potential to replace the twice as heavy nickel based superalloys in high temperature applications due to their excellent combination of mechanical and physical properties. Replacement of Ni-based superalloy applications would reduce structural weight as well as stresses in rotating parts [1]. These materials exhibit properties such as a high melting point of 1460°C, density of 3.9-4.2g/cm³, high specific strength, good resistance against oxidation and high creep and corrosion resistances. Furthermore, γ-TiAl shows high ignition resistance ("titanium fire") in comparison to conventional titanium alloys [2,3,4,5,6]. Figure 1 shows a comparison of the specific strength as a function of temperature of several materials. TiAl exhibit higher specific strength at high temperatures than conventional titanium alloys and superalloys [7].
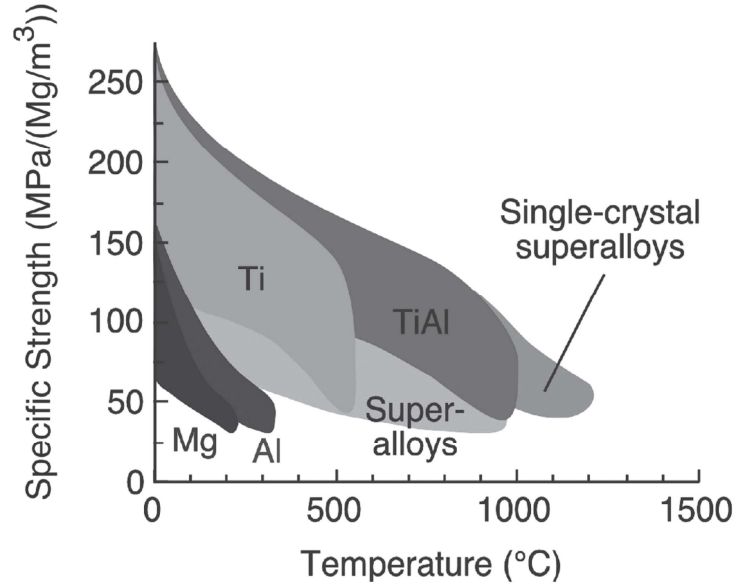
Figure 1: Specific strength as a function of temperature for several materials [7].

These outstanding properties make γ-TiAl attractive for applications at elevated temperatures. The first commercial application of γ-TiAl was reported in 1999, when Mitsubishi introduced the Lancer Evolution VI series automobiles equipped with γ-TiAl turbocharger into the market. Intensive research has been performed on γ-TiAl for turbocharger wheels in combustion engines, valves in sports and racing cars and low pressure turbine blades in jet engines [8]. On the other hand TiAl alloys are expensive materials. Their high costs are related to their complex processing and hinder the application in new domains such as in chemical and energy industries [9].

However, the main disadvantages of the intermetallic TiAl are their low ductility and toughness at room- and service temperatures [10]. Therefore, extensive researches on the optimisation of ductility have been performed during the last few years, and some improvements have been achieved by combining thermomechanical processing with the use of ternary elements. Ternary elements such as Nb, Mo, Cr and V allow the formation of better

deformable phases [11,12]. In this way, the 3rd generation of γ-TiAl alloys called TNM has been developed, which consists of Ti and Al with additions of Nb, Mo and B that stabilise the ductile bcc β phase at processing temperatures.

Additions of B facilitate grain refinement [13], whereas Mo and Nb are β phase stabilisers. The TNM alloy is characterised by the improved hot workability due to the presence of considerable amounts of the easily deformable β phase. The disordered bcc β phase provides a sufficient number of independent slip systems in γ-TiAl based alloys. A Nb content between 5-10% improves the room temperature ductility as well as the creep and oxidation resistances [14,15]. In the TNM alloys the volume fraction of the β phase can be controlled by choosing appropriate forging and/or heat treatment temperatures [7].

During hot deformation several dynamic processes can occur, which can strongly impact the hot deformation behaviour of γ-TiAl. These dynamic processes such as dynamic recrystallisation, ductile damage and phase transformations can cause softening. The flow instabilities during hot deformation can cause catastrophic failure of the workpiece, limiting production.

The **objectives** of this work are to study the hot deformation behaviour of a TNM alloy by determining the relationship between the thermomechanical processing parameters and the microstructure. Especially the ductile damage behaviour under different processing conditions is analysed and modelled. Various approaches for the modelling of the hot deformation behaviour such as processing maps and constitutive equations are used to identify the optimum hot working conditions to manufacture low-pressure turbine blades based on γ-TiAl. The prediction of flow instabilities is performed by existing instability criteria based on DMM, the flow localisation parameter α_{SJ}, the strain rate sensitivity parameter m and the continuum damage models coupled to FEM. The predictions of the instability models used are correlated with microstructural investigations of the deformed specimens.

2 Literature Review

2.1 Intermetallics

Intermetallics show different crystal structures and properties compared to their parent metals [16]. Mainly intermetallic compounds display metallic bonding with ionic and covalent characteristics, thus showing properties between metals and ceramics. The chemical ordering in ordered intermetallics causes a good stability of superlattice crystal structures, low atomic mobility at high temperatures and reduced dislocation mobility [17]. However, this ordering is an obstacle for plastic deformation and therefore intermetallics are characterised by low ductility, complex machining and handling [4]. However, at elevated temperatures intermetallics like γ-TiAl behave as metal and show good deformation behaviour [18,19,20]. Some examples of intermetallic compounds are TiAl, Ti_3Al, $TiAl_3$, Ni_3Al, FeAl and Co_3Ti.

2.1.1 Gamma titanium aluminides

Conventional γ-TiAl are composed by α_2-Ti_3Al and γ-TiAl phases. The binary phase diagram of TiAl is shown in Figure 2. Apart from these two phases, several intermetallic phases such as $TiAl_2$ and $TiAl_3$ occur. The Al content in the α_2 phase ranges between 22-39 at% and in the γ phase between 48.5 and 66 at%. A mixture of α_2 and γ is at Al contents between 37-49% [21]. Only α_2-Ti_3Al and γ-TiAl are of technical interest, since the two other phases ($TiAl_2$ and $TiAl_3$) are too brittle. Technical alloys lie in the range between 44-48% Al. The α_2 phase is characterised by good strength and low ductility at service temperatures. Both α_2 and γ phases are brittle. However, the two phase alloys (α_2+γ) provide a good ductility due to the solubility of minor elements in the α_2 phase, thus increasing the ductility of the γ phase [16,22].
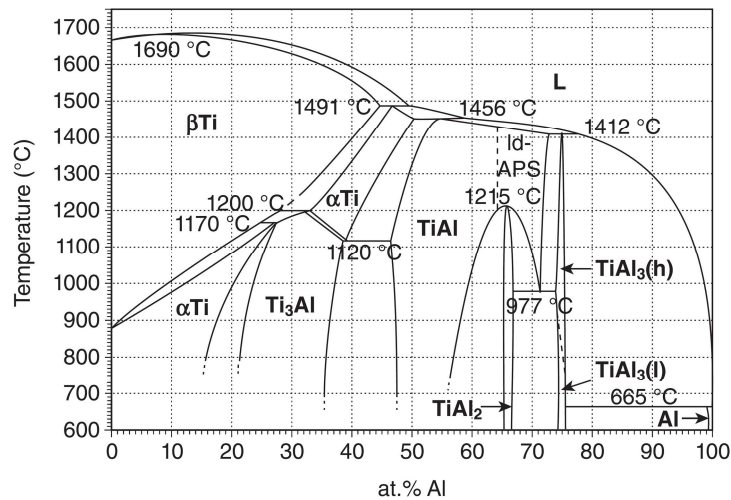
Figure 2: Binary Ti-Al phase diagram according to Schuster and Palm [23].

In γ-TiAl alloys several phase transformations can occur during cooling from high temperature regions or during subsequent heat treatments. The alloy composition can change the solidification path drastically [24]. The solidification can be either through the β phase for Al concentrations up to around 44 at% Al or peritectically for higher Al concentrations through the α phase. The solidification reaction for higher Al concentrations between 45-48%

is characterised by the formation of primary β dendrites and growth preferentially along the direction of the heat flow. After reaching the peritectic temperature, the α phase nucleates at the interface between the primary β phase and the melt. Upon subsequent cooling, the α phase decomposes based on the reaction α→α+γ→α2+γ or α→α2→ α2+γ [25]. The γ lamellae precipitate from α or α2 grains and form the α2+γ lamellae [26]. At Al concentrations above 49% the α phase is the first formed phase, which then transforms into the γ phase. From the single α phase field many phase transformations are feasible depending on the cooling rate. At the highest cooling rate, the α phase transforms into the ordered α2 phase. By decreasing the cooling rate, several phase transformations can occur: composition invariant massive α→γ transformation or lamellae γ phase formation. Low cooling rates cause the formation of γ grains. The crystallographic orientation relationship between α2 and γ phases, is called the Blackburn [27] orientation relation. The two planes $(111)_\gamma$ and $(0001)_{\alpha_2}$ as well as the two directions $\langle 1\bar{1}0]_\gamma$ and $\langle 11\bar{2}0\rangle_{\alpha_2}$ are parallel to each other

$$(111)_\gamma \| (0001)_{\alpha_2} \text{ and } \langle 1\bar{1}0]_\gamma \| \langle 11\bar{2}0\rangle_{\alpha_2}.$$

Directional solidification processing can be used to influence the texture of cast alloys by selecting different solidification paths through relatively small variations of the alloy composition [28]. The semi binary phase diagram in Figure 3 shows the range of Al from 30-60 at% in a constant value of 8 at% Nb. The advantages of using Nb are due to the fact that it reduces the stacking fault energy, retards diffusion processes and modifies the structure of the oxidation layer [4]. Furthermore, Nb additions cause an increase of 60-100°C in the melting temperature and a decrement of the β transus temperature. Therefore, the β phase region is extended to higher Al concentrations. Another effect of Nb is a decrease in α transus temperature, which means that the α phase region becomes narrow and shifts to higher Al concentrations. The low temperature phase region (α2+γ) is replaced by the (α2+γ+β$_o$) ternary phase region if Nb content exceeds 10% [29].
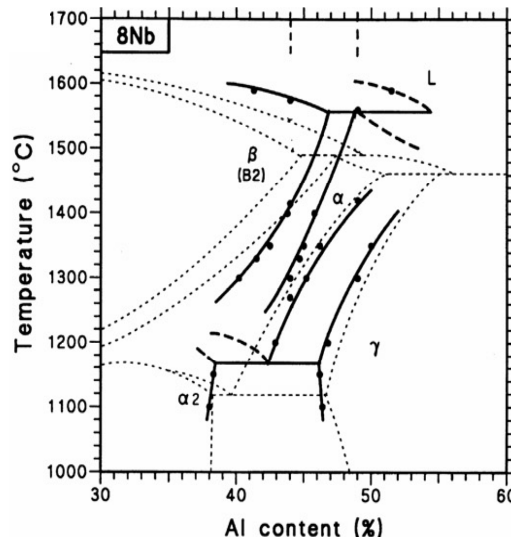
Figure 3: Ti-Al-Nb system with 8 at% Nb [14].

The 2nd generation alloys were developed in the 1990s and are characterised by a higher concentration of trace elements. One example for this generation is the GE alloy Ti-48Al2(Cr or Mn)-2Nb [2]. 2nd generation alloys are composed by a lamellar grain refined microstructure and show improved ductility, strength, and oxidation resistance. However, the demand for

better hot working properties has led to the development of 3rd generation γ-TiAl alloys with more additional ternary elements and the reduction of Al concentration to 44 at%. The addition of Al or Nb increases the strength and C, Si and N are responsible for a better creep resistance and high temperature performance. Other elements like Ta, Mo and W improve oxidation resistance. B forms borides during solidification, which can refine the microstructure of the ingot by pinning the growth of α grains upon heating in α phase field [30]. The addition of B causes a slight increase in eutectoid- and α-transus temperatures [31]. An improved ductility is achieved by the addition of Cr, V, Mn and Si, while at the same time reducing the oxidation resistance.

In this work the use of 3rd generation alloy TNM is described in [33,34]. The composition range for TNM alloys is Ti(42-44Al)(3-5Nb)(0.1-2Mo)(0.1-1B). The stabilisation of the β phase is performed by Nb and Mo, due to the fact that Mo has a four times higher stabilising effect than Nb. At elevated temperatures the material goes through the disordered β-TiAl phase, which then transforms into the ordered $β_o$-TiAl with a B2 structure at low temperatures. The composition of the TNM alloy is marked in the diagram (see Figure 4 (a)). The phase fraction diagram for the chemical composition of Ti−43.67Al−4.08Nb−1.02Mo−0.1B is shown in Figure 4 (b). The solidification pathway of the TNM alloy is:

L→L+β→β→β+α→β+α+γ→α+β+$β_o$+γ→α+$β_o$+γ→α+$α_2$+$β_o$+γ→$α_2$+$β_o$+γ [34].

It shows that there is no occurrence of a single α phase field region. Solidification via the β phase allows an equiaxed and texture-free microstructure with low microsegregation [35]. The experimentally determined phase transition temperature for Ti-43.67Al-4.08Nb-1.02Mo-0.1B alloy is 1160°C for the eutectoid temperature (T_{eu}). The ordering reaction of the α phase occurs between 1160-1170°C and the γ solvus temperature ($T_γ$) is 1260°C. The ordered β phase transforms into the disordered structure between 1175-1205°C, which is beneficial to deformation due to its independent slip systems [36]. At temperatures above 1415°C the alloy is in the single phase β region [37].
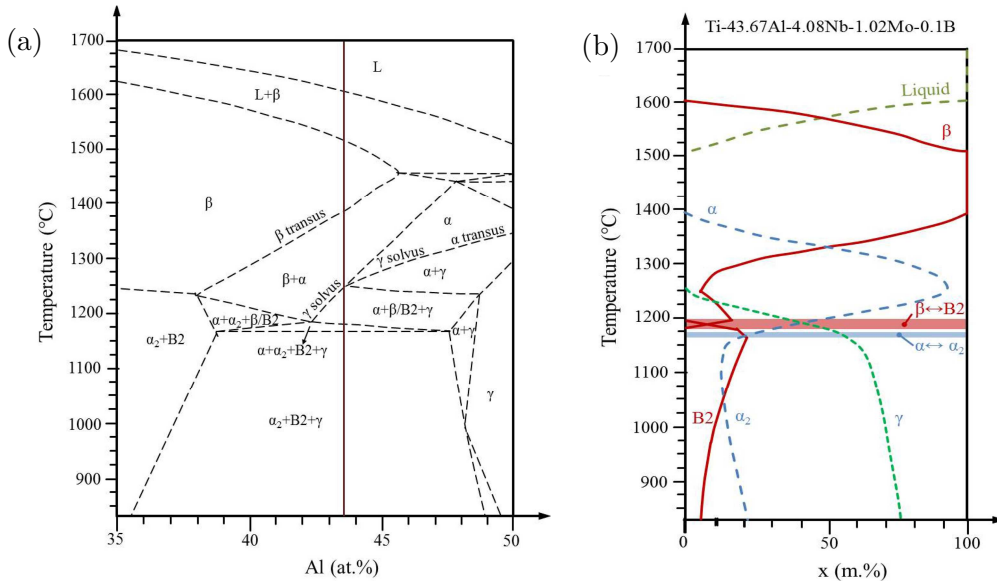
Figure 4: (a) Experimental phase diagram of the Ti−×Al−4Nb−1Mo−0.1B and the Al content of the investigated alloy is indicated as a vertical line and (b) phase fraction of the alloy with the chemical composition of Ti-43.67Al-4.08Nb-1.02Mo-0.1B [35,38].

The crystal structures of the phases present in the TNM alloy are shown in Figure 5. The γ-TiAl exhibits a face-centred tetragonal $L1_0$ structure [5] with a Pearson sign of TP4 and a lattice space group of P4/mmm. The γ phase consists of a layered arrangement of alternating Ti- and Al atoms in c direction [38] and therefore the unit cell exhibits a small tetragonality with a c/a ratio of about 1.02. The higher the Al content, the larger is the tetragonal distortion [39]. The hexagonal crystal structures α-Ti(Al) and α_2-Ti$_3$Al are strongly related with each other and they are in the same space group. Below the eutectoid temperature the disordered α-Ti(Al) with its A3 structure transforms into the ordered α_2-Ti$_3$Al with a $D0_{19}$ structure. At elevated temperatures the material consists of the disordered β (bcc)-TiAl phase. At low temperatures the disordered β phase transforms into ordered β_o-TiAl with a B2 structure [38]. The TNM alloy exhibits the ordered structure β_o/B2-TiAl at service temperature (600-750°C).
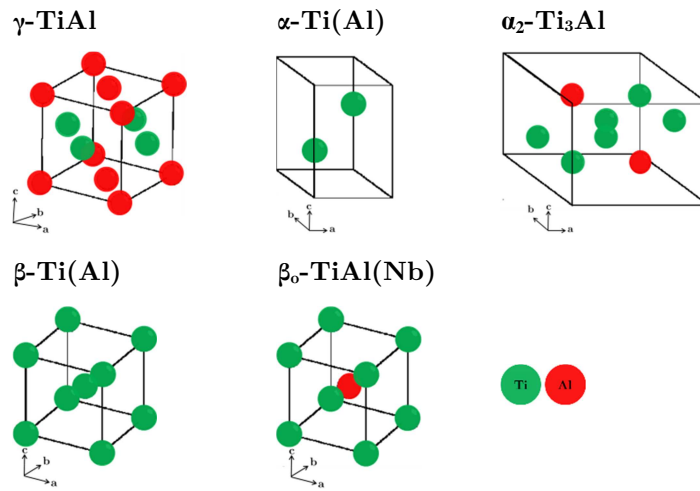
Figure 5: Schematic illustration of crystal structures of the phases present in the TNM alloy [38].

2.1.2 Microstructures

Microstructure and the composition of the alloy have an essential influence on the properties of the final product. The different heat treatments facilitate to achieve the microstructures and these are the following:

- fully lamellar,
- nearly lamellar,
- duplex,
- near gamma.

By applying a heat treatment **above the eutectoid temperature** (T_{eu}) the formation of near gamma microstructure takes place and is marked as T1 (see Figure 6). The near gamma microstructure consists of globular γ-TiAl and α_2-Ti$_3$Al grains.

Duplex structure consists of γ grains and lamellar α_2/γ grains and is the result of the heat treatment in the **α+γ region**. The cooling rate influences the volume fraction of the lamellar

colonies and the average spacing of lamellae. An increased cooling rate decreases spacing of lamellae, because the time for diffusion is shorter than at high cooling rates (marked as T2 see Figure 6).

A heat treatment **below the γ-solvus temperature** leads to the formation of a lamellar microstructure of α_2/γ, as marked with T3 in Figure 6.
On the triple points and at grain boundaries there is a small volume fraction of fine γ grains and these hinder the rapid grain growth of the prior globular α grains. Boron forms Ti borides that decrease the growth rate of α_2 grains.

A heat treatment **above the γ-solvus temperature** in the single α phase region leads to the formation of a fully lamellar microstructure, consisting of α_2/γ lamellar colonies (as marked with T4 in Figure 6). The lamellar microstructure can coarsen unhindered, because there are no γ_g grains that can act as obstacles. However, these coarse-grained fully lamellar microstructures present an extremely low tensile ductility at room temperature.

Near gamma (NG) and duplex (DP) microstructures reveal good strength and ductility properties, in spite of their moderate creep resistance and low fracture toughness. Fully lamellar (FL) and nearly lamellar (NL) microstructures show the highest creep resistance, but suffer from poor ductility at low temperatures [42]. The lamellar microstructures exhibit higher fracture toughness and crack propagation resistance compared to duplex microstructures [41]. Colony spacing and size have a significant influence on the mechanical properties [44,45,46]. For example the tensile elongation at room temperature depends mainly on the colony size, a decrease of which leads to an increase in ductility [43].

Figure 6: Binary TiAl phase diagram marked with different temperatures and resulting microstructures at room temperature (adapted from [45]).

2.2 Hot deformation

Appel et al. [26] have summarised the major concerns involved in hot working of γ-TiAl alloys. γ-TiAl shows high plastic anisotropy, because of the lack of independent slip systems. In addition the material is characterised by low dislocation mobility. The softening mechanisms such as recrystallisation are retarded due to the low diffusivity and low grain boundary mobility [46].

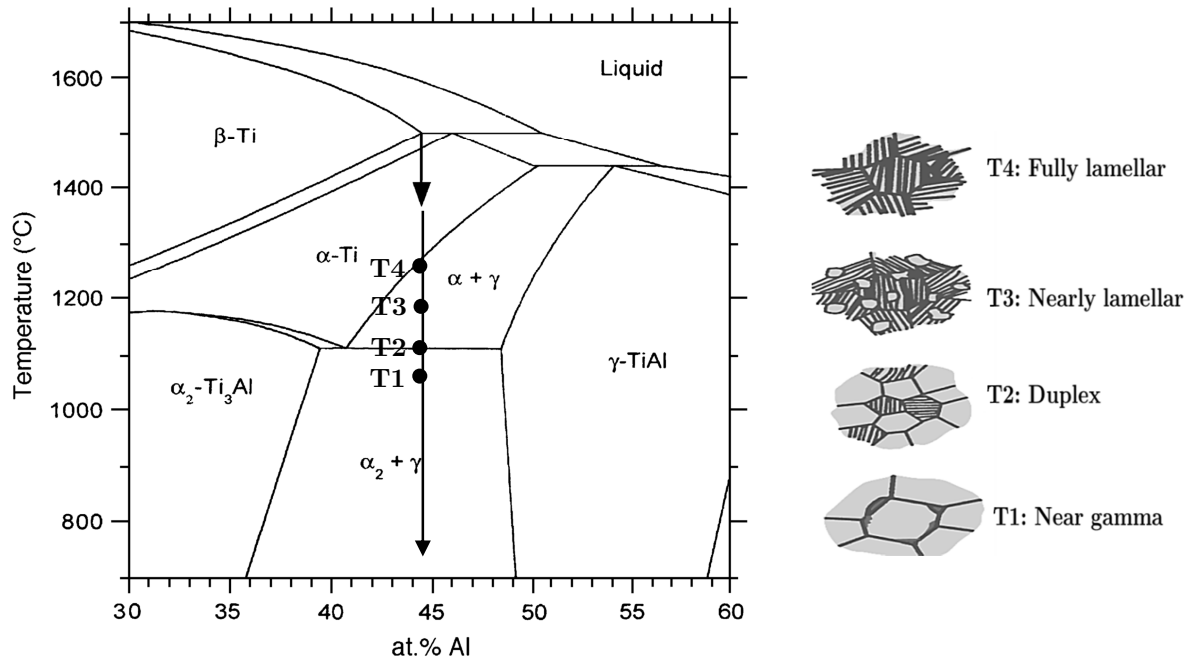The main obstacle for a wide industrial application of wrought γ-TiAl based alloys is their low ductility even at high temperatures, which also limits their workability. Their poor formability is due to the intermetallic bonding in the γ-TiAl and α_2-Ti$_3$Al phases. On the other hand, cast materials show a coarse columnar structure, sharp casting texture and dendritic segregation. Therefore, the TNM alloying concept is a promising design strategy to overcome brittleness and to improve hot workability. TNM alloys present a wider forging window in comparison with conventional γ-TiAl [8]. The Al content together with a third alloying element, the deformation temperature and the purity of the material have strong influence on the deformation mode. High temperatures facilitate both, the activation of more slip systems and the formation of the β phase. Furthermore, high temperatures enhance dislocation climb, causing restoration or dynamic recovery (DRV) or dynamic recrystallisation (DRX). However, high temperatures produce contamination and oxidisation, and a protective atmosphere or coatings should be used during processing. The oxygen enrichment of Ti leads to the stabilisation of the α phase, and α-case layer is formed. This α layer is very brittle and the depth of the α-case layer depends on temperature and duration [47].

2.2.1 Deformation mechanisms in γ-TiAl alloys

In single phase γ alloys the deformation at room temperature occurs by twinning and superdislocations in contrast to two phase alloys. In two phase alloys the low ductility of the α_2 phase is attributed to the solid solution hardening as a result of oxygen dissolution from the γ phase. Thereby the dislocations in the γ phase can move without any obstacle and due to this the γ phase has a better deformability than the α_2 phase. The γ-TiAl alloys have a large plastic anisotropy at room temperature, which decreases at elevated temperatures. Appel et al. [3] have reported that the deformation behaviour of γ-TiAl is closely related to its L1$_0$ crystal structure. Addition of Nb reduces the stacking fault energy in the γ phase and increases the ratio of c to a of the γ unit cell, resulting in a faster mobility of superdislocations. In summary, alloys with Nb exhibit a deformation mechanism dominated by a combination of super-, ordinary and twin dislocation motion at room- and elevated temperature [51,52].

The most dominant deformation modes in the **γ phase** are ordinary dislocations, ordered twinning and superdislocations. At room temperature the deformation is carried out by gliding on {111} γ planes along the <110> directions [50], as shown in Figure 7 (a). The possible Burgers vectors for ordinary dislocations are b1=<010] and b2=1/2<110]. However, occasionally deformation is performed at room temperature by means of superdislocations [51]. The slip systems are summarised in Table 1.

Table 1: Slip systems in γ-TiAl with the deformation types super (s) or ordinary (o) dislocation glide. The morphology of γ lamellar phase is longitudinal (l), mixed (m), or transversal (t) [52].

No	Slip plane	Slip direction	Type	Morphology
1		$[011]$	s	t
2	$(11\bar{1})$	$[101]$	s	t
3		$[1\bar{1}0]$	o	m
4		$[0\bar{1}1]$	s	m
5	$(\bar{1}11)$	$[\bar{1}0\bar{1}]$	s	t
6		$[\bar{1}\bar{1}0]$	o	t
7		$[011]$	s	t
8	$(1\bar{1}1)$	$[10\bar{1}]$	s	m
9		$[110]$	o	t
10		$[01\bar{1}]$	s	l
11	(111)	$[10\bar{1}]$	s	l
12		$[1\bar{1}0]$	o	l

In addition, order twinning occurs along $1/6\langle 11\bar{2}\rangle\{111\}$, as shown in Figure 7 (b). The dislocation with Burgers vector $b3=1/6[11\bar{2}]$ is called true twinning, because it does not change the order of γ-TiAl. Partial dislocations with Burgers vectors $b1=1/6[\bar{2}11]$ and $b2=1/6[1\bar{2}1]$ change the order of γ in a pseudo twinning [53]. In contrast to fcc metals, there is only one distinct true twinning direction per $\{111\}$ plane that does not alter the ordered $L1_0$ structure. Nevertheless, in TiAl alloys the von Mises criterion [54] for a general plastic shape change is satisfied in principle, because the $L1_0$ structure provides more than five independent slip systems. However, the relative ease and propensity of these deformation modes depend on the Al concentration, the content of ternary elements and the deformation temperature [46]. Many researchers suggest that the alloying elements Mn and Cr decrease the covalent nature of bonding in γ-TiAl thus reducing the tetragonality of the $L1_0$ structure and leading to an increase in the number of deformation modes.
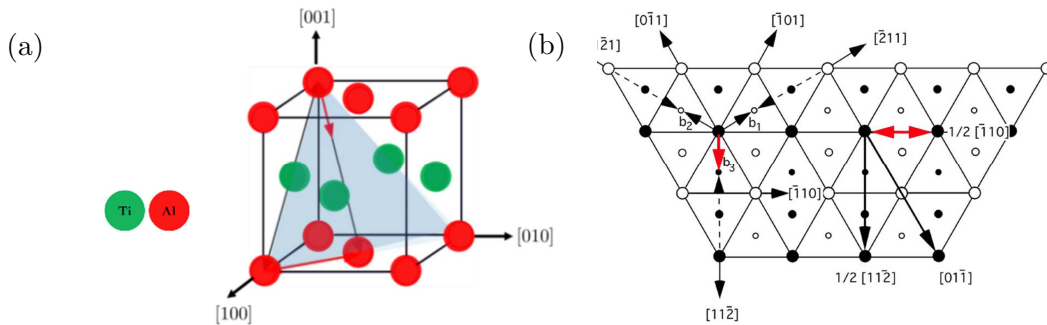
Figure 7: Schematic graphic dominant glide directions in the γ phase with $L1_0$ crystal structure (a) unit cell and (b) three-layer sequence of Ti and Al atoms on the (111) plane and the dislocations with Burgers vectors [4]. Open and shaded circles represent the Ti and Al atoms, respectively.

In the **α₂-Ti₃Al** phase the slip occurs on the prismatic, basal and pyramidal planes. The deformation is carried out by the slip dislocations 2\3 $[11\bar{2}0]$ on the basal $[11\bar{2}0]$ (0001), prismatic $[11\bar{2}0]$ $(1\bar{1}00)$ and pyramidal $[\bar{1}\bar{1}26]$ $(11\bar{2}1)$ systems as shown in Figure 8. The pyramidal slip systems is activated above 700°C [20].

Table 2: Slip systems in the α₂ phase [52].

No	Slip plane	Slip direction	Type
1		$[\bar{2}110]$	
2	(0001)	$[1\bar{2}10]$	basal
3		$[11\bar{2}0]$	
4	$(1\bar{1}00)$	$[11\bar{2}0]$	
5	$(01\bar{1}0)$	$[\bar{2}110]$	prismatic
6	$(10\bar{1}0)$	$[1\bar{2}10]$	
7	$(11\bar{2}1)$	$[\bar{1}\bar{1}26]$	
8	$(1\bar{2}11)$	$[\bar{1}2\bar{1}6]$	
9	$(\bar{2}111)$	$[2\bar{1}\bar{1}6]$	pyramidal
10	$(\bar{1}\bar{1}21)$	$[11\bar{2}6]$	
11	$(\bar{1}2\bar{1}1)$	$[1\bar{2}16]$	
12	$(2\bar{1}\bar{1}1)$	$[\bar{2}116]$	

High temperature deformation (700-800°C) occurs mainly in the γ phase and climbing of dislocations is active in contrast to room temperature. As known from literature, twinning is commonly observed at low temperatures, but in the two phase alloys there is a high activation of mechanical twinning in the γ phase. At elevated temperatures the α₂ phase is more ductile than at room temperature.
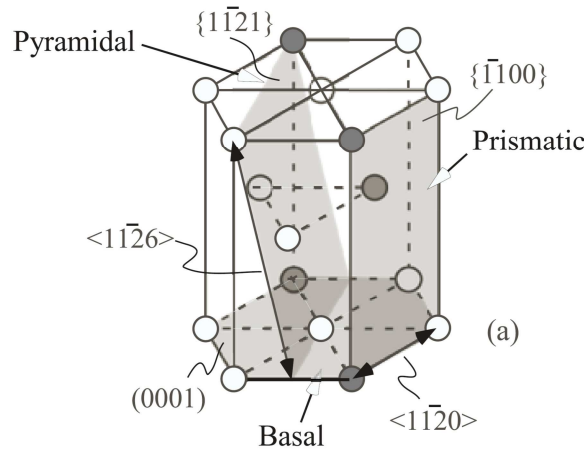
Figure 8: Schematic graphic dominant glide directions in the α₂ phase [55].

Literature doesn't provide much information about the deformation behaviour of the ordered and disordered **β phases**. The disordered β phase reveals independent glide and twinning systems. Gliding in the high temperature β phase occurs in <111> directions on {110}, {112} and {123} planes [36]. In the three phase alloys plastic deformation occurs mainly on the bcc β phase.

2.2.1 Restoration mechanisms

Hot plastic deformation of metals takes place with an increase of dislocation density (strain hardening) that is continuously counteracted by softening processes. These softening processes occur during deformation and are referred to as dynamic restoration processes such as DRV and DRX. The softening processes which occur during heat treatments are termed static recovery and recrystallisation [59,60].

2.2.1.1 Recovery

Recovery is a restoration process that occurs in materials with high stacking fault energy (SFE), such as ferritic steels, β-titanium and many others. High SFE implies that the stacking faults cannot easily be formed during plastic deformation thus allowing the more or less free movement of dislocations. Recovery involves two main processes: annihilation of dislocations and their rearrangement into low angle grain boundaries (LAGB). The target of recovery is to decrease energy configuration, meaning the density of dislocations [61,62]. These two processes take place as a consequence of glide, climb and cross-slip of dislocations. At low and medium temperatures the most dominant recovery mechanism is dislocation glide and cross-slip. Dislocations with opposite signs (antiparallel) can annihilate if they are on the same glide plane. A recovery process occurs due to climbing of dislocations, which requires thermal activation [60]. Dislocations with equal signs cannot annihilate by glide and form LAGB in order to minimise their energy. This process is referred to as polygonization [59].

Deformation causes an increment of the stored energy due to the increment of dislocations. This stored energy depends on deformation parameters such as temperature, strain and strain rate and on material characteristics, especially SFE, grain size and the presence of second phases. The stored energy difference (ΔE) among grains is the driving force for both recovery and recrystallisation [59].

At the beginning of hot deformation an increase in flow stress occurs, due to the interaction and multiplication of dislocations. The increase in dislocation density and thus, in the driving force, result in an increase of the dynamic recovery rate. During this time LAGBs are formed. After achieving a dynamic equilibrium between work hardening and recovery rate the dislocation density remains constant and a steady-state flow stress is obtained. Figure 9 illustrates the flow curve and microstructural change correlations during DRV. McQueen et al. suggested that DRV is a sufficient restoration mechanism in high temperature deformation to provide the steady state substructure in Al and in α-Fe alloys [61].
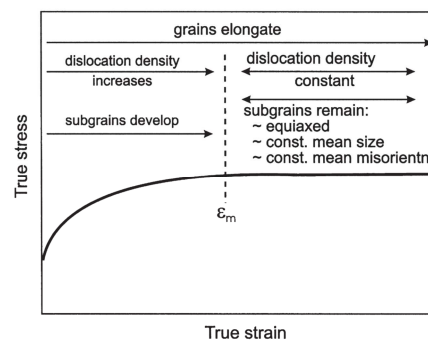

Figure 9: Summary of the microstructural changes and flow evolution during dynamic recovery [59].

2.2.1.2 Recrystallisation

Recrystallisation is characterised by the forming of new grains in highly deformed zones by formation and migration of high angle grain boundaries (HAGB) [62]. HAGBs are characterised by a misorientation larger than 15° [58]. The driving force for boundary migration is the stored energy difference by dislocations [57].

Dynamic recrystallisation provides a unique opportunity to control the microstructure and the properties of materials unter hot working. Dynamic recrystallisation occurs in materials with low SFE. Low SFE materials are for instance Ni-base superalloys, austenitic steels and copper [63]. Two types of DRX are reported in literature. One is the discontinuous dynamic recrystallisation (dDRX) i.e. the classical recrystallisation that proceeds with nucleation and grain growth. The second mechanism is the continuous dynamic recrystallisation (cDRX), which operates by the transformation of low angle grain boundaries into high angle grain boundaries by lattice rotation [64].

dDRX is the classical recrystallisation mechanism that occurs during hot working of metals and alloys of low to medium SFEs. These are materials with relatively low rates of DRV due to the low mobility of dislocations, allowing a retention of large amounts of stored energy [59]. Large grain boundary migration rates are observed in dDRX due to high local dislocation density gradients. The grain boundary migration rates for dDRX are 10 to 100 times larger than for cDRX [65]. The dDRX occurs by nucleation and grain growth. Nucleation sites for recrystallisation are typical areas with high misorientation such as pre-existing high angle grain boundaries [66,67,68,69].

The characteristic stress-strain curves during hot deformation present a peak that indicates the occurrence of dDRX. The DRX begins before achieving the strain of the peak stress at a strain called the critical strain ε_c. When the critical strain is achieved, nucleation takes place. The critical strain is influenced by the chemical composition, the initial grain size and the deformation parameters [70,71]. The critical strain decreases with increasing temperature and decreases with strain rate and grain size [71]. Furthermore, the original grain size has a large influence on the DRX: the larger the original grain sizes, the slower the rate of recrystallisation [72]. The flow curves are characterised by single or multiple peak stresses. Single peaks are correlated to grain refinement and multiple peaks are observed when sequential grain refinement and coarsening occurs [73,58].

The **cDRX** starts with a DRV process and occurs at large strains. In contrast to the dDRX the cDRX mechanism does not involve nucleation and growth. cDRX is usually caused by progressive lattice rotation and the geometric DRX (gDRX) by the fragmentation of the initial grains. Many authors claim that cDRX should be referred to as a form of recovery, because it is a combination of work hardening, DRV and HAGB migration. cDRX is observed in many metals as in Al alloys, ferritic stainless steels and microalloyed steel. It is a useful mechanism for grain refinement, when deformation at large strains is involved. cDRX is characterised by much slower kinetics compared to dDRX and the microstructure requires remarkable larger strains [64].

A comparison of the characteristics of dDRX and cDRX are summarised in Table 3. A significant difference between dDRX and cDRX is that the microstructure recrystallised by cDRX shows a less invariant crystallographic texture.

Table 3: Comparison of the characteristics of dDRX and cDRX [59,74].

	dDRX	**cDRX**
Strain	Strain beyond ε_c (<1)	Large strains (ε>>1)
Stacking fault energy	Low and medium	High
Flow stress behaviour	Steady-state flow following single or multiple peak stress	Pseudo steady-state flow following gradual strain softening and final steady state
Effect of temperature (T/T_m) or strain rate $\dot{\varepsilon}$	Thermally activated flow assisted by lattice diffusion	Mixed athermal and thermal behavior
Dynamic recovery	Weak	Strong
High angle grain boundary	Rate of migration is high	Rate of migration is low
Characteristics of the dislocation substructures	Substructures vary from grain to grain and develop inhomogeneously (weak texture)	A strong crystallographic texture formed [75]
Dislocation distribution	Inhomogeneous	Homogeneous

The cDRX is characterised by the **progressive accumulation** of dislocation networks that form subgrain structures with LAGB. The subgrains are driven to rotate progressively. With increasing misorientation during further straining, the subgrains transform into high angle grain boundaries. There is a misorientation gradient between edge and centre of the grains that results in a partially recrystallised structure. With increasing strain a fully recrystallised structure can be formed [59].

The **geometric dynamic recrystallisation** (gDRX) is a further cDRX process. gDRX has been observed in many materials such as Al and Mg alloys at large strains and at elevated temperatures. During hot compression or hot rolling the cross section of the material is largely reduced, whereas the original grains become flattened. With increasing strain the fraction of HAGB increases and the boundaries become serrated. Large strains can cause impingement of HAGB, producing a microstructure of HAGB. The texture of the formed new grains is similar to the deformed texture. A further characteristic of this mechanism is the limited HAGB migration [59].

2.2.2 Flow instabilities and flow localisation

The hot workability of γ-TiAl is limited by flow localisation, flow instability and damage due to its complex microstructure and low ductility of the phases [76].

Flow instabilities can be divided in geometric or intrinsic instabilities. Geometric instabilities mean that a load state is necessary to form instabilities. Intrinsic instabilities are caused mainly by microstructural changes in the material, which means they are based on the physical material properties [77]. The models to predict intrinsic instabilities are based on the dynamic constitutive flow behavior of the material [78]. These dynamic material models will be discussed in the following sub-chapters. Flow instabilities produce pores and cracks. At low strain rates many scientists report that wedge cracks are commonly initiated at grain boundaries and triple points, when the stress cannot be released by grain boundary migration. At higher strain rates wedge cracks are mainly formed due to the intersection of slip band or deformation twins with grain boundaries [7].

Flow localisation is mainly produced by non-uniform plastic flow due to localised flow softening, friction or chilling effects during hot deformation [79]. Metallurgical weakness is referred to local variations in the grain orientation (texture), grain size and precipitation state. High friction and a low height to diameter ratio increases barrelling and the magnitude of flow localisation, that appears in form of necking in tension and bulge formation or shear bands in compression [76]. The strain at which flow localisation starts and ends, depends on strain rate sensitivity of the material. Strain rate sensitive materials show that flow localisation initiates earlier and terminates later in contrast to rate insensitive material [80].

Flow localisation can appear in form of shear bands, which are narrow, nearly planar zones characterised by high deformation [81]. The non-crystallographic shear bands caused by shear stresses appear in polycrystals at an angle of 45° with respect to the uniaxial compression direction. A specific type of shear bands is the so called adiabatic shear band (ASB). ASB occur at high strain rates, where the material does not have enough time for heat transport to the environment. As a consequence there is a significant localisation of temperature in this region and this causes unstable deformation zones i.e. shear bands [80,81,87]. At very large strains the shear bands can be seen on the macroscopical level. These formed shear bands can act as nucleation sites for further damage [85]. In γ-TiAl alloys flow localisation is observed mainly when deforming lamellar microstructures. Semiatin et al. [86] have reported that cracks have formed along shear bands in extruded Ti-45Al-8Nb-0.2C alloy.

In forging presses a temperature gradient between the workpiece and the colder tools develops along the workpiece and produces a non-uniform distribution of temperatures, strain rates and strains. As the flow stress is influenced by temperature, the workpiece area in contact with the tools will not deform as easily as the bulk of the workpiece. These transition zones can cause further failure in the workpiece. Without any friction and temperature gradient the deformation takes place uniformly and the stress is constant across the diameter and along the sample [87].

The material instability can cause a **localisation of strain** [88] and strain localisation can occur at low or large strains [89]. Strain localisation can be manifested as macroscopic or microscopic. The macroscopic strain localisation can be seen with the naked eyed and their shape is determined by geometry and boundary conditions. The microscopic strain

localisation can appear as shear band or narrow bands at lower strains [89]. It can be attributed to the local plastic flow instabilities and temperature gradients. Strain localisation can cause local softening of the material [90]. It is reported that in titanium alloys strain is localised at the centre of the specimen due to the chilling effect [91].

2.3 Modelling

2.3.1 Modelling of flow stress

In literature there are numerous empirical flow stress models such as Hollomon, Ludwik, Johnson-Cook, Spittel-Hensel, Voce and Zerilli-Armstrong models. Physical models take the strain rate and thermal history effects into account by introducing internal state variables such as dislocation densities (Mecking and Kocks, Follansbee and Kocks). The present study does not consider physical based models, and it focusses on optimising empirical models.

As an example of phenomenological models, **Hollomon** equation is used to describe the hardening behaviour of the material during plastic deformation as [92]:

$$\sigma = K_H \, \varepsilon^{n_H}$$

<div align="right">Eq. 1</div>

where K_H and ε^{n_H} are material dependent constants. In the Hollomon equation flow stress is regarded as a function of strain, so that this approach is only an empirical consideration of the measured flow curves. The n parameter in the equation above is a function of temperature and strain rate [92].

An extension on Eq. 1 is performed by **Ludwik** and this model considers the yield strength [93], as shown in Eq. 2.

$$\sigma = \sigma_0 + K_L \, \varepsilon^{n_L}$$

<div align="right">Eq. 2</div>

The **Voce** equation also describes the flow behaviour of the material and this model considers the fact that material cannot harden indefinitely, and introduces a saturation parameter in addition [94].

$$\sigma = \sigma_s + (\sigma_0 - \sigma_S) \exp\left(-\frac{\varepsilon}{K_v}\right)$$

<div align="right">Eq. 3</div>

where σ_0, σ_S and K_v have to be adjusted.

One of the best known phenomenological material constitutive models is the **Johnson and Cook** model (JC) as already applied to many materials. The advantages of this model are its simplicity to determine the material constants, easy implementation into many FE software codes and the availability of its parameters in literature [98,99]. Therefore, the model is already used in many commercial FE packages [95]. The JC model is expressed as:

$$\sigma = [A + B\varepsilon^n]\left[1 + C ln\left(\frac{\dot{\varepsilon}}{\dot{\varepsilon}_0}\right)\right]\left[1 - \left(\frac{T - T_r}{T_m - T_r}\right)^p\right]$$

<div align="right">Eq. 4</div>

where σ is the equivalent flow stress, ε is the equivalent plastic strain, $\dot{\varepsilon}$ is the equivalent plastic strain rate, $\dot{\varepsilon}_0$ is the reference equivalent plastic strain rate, T is the workpiece

temperature, T_m is material melting temperature and T_r is room temperature. A, B, n, C and p are material parameters that are determined from flow stress data [99]. The parameter n represents the strain hardening index, the parameter p describes the thermal softening and C refers to strain rate sensitivity.

One main limitation of the model is that this approach does not involve any thermal or strain rate history effects [92,93]. The JC model describes well the material behaviour up to strain rates of $10^3 s^{-1}$. During deformation at large strains the material is subjected to dynamic softening such as restoration processes, damage or phase transformations. The JC model is not suitable for materials, that soften during deformation [85,88,104,105].

Calamaz et al. [104] and Özel et al. [105] have introduced a strain softening term into the JC model. This model is called **hyperbolic tangent** (TANH) and is suitable for materials with flow softening [103].

$$\sigma = \left[A_1 + B\varepsilon^n \left(\frac{1}{exp\varepsilon^a} \right) \right] \left[1 + Cln\frac{\dot{\varepsilon}}{\dot{\varepsilon}_0} \right] \left[1 - \left(\frac{T-T_r}{T_m-T_r} \right)^p \right] \underbrace{\left[D + (1-D) \, tanh \left(\frac{1}{(\varepsilon+S)^c} \right) \right]}_{} \qquad \text{Eq. 5}$$

$$\underbrace{\phantom{\sigma = \left[A_1 + B\varepsilon^n \left(\frac{1}{exp\varepsilon^a} \right) \right] \left[1 + Cln\frac{\dot{\varepsilon}}{\dot{\varepsilon}_0} \right] \left[1 - \left(\frac{T-T_r}{T_m-T_r} \right)^p \right]}}_{\text{Johnson Cook}} \qquad \underbrace{\phantom{\left[D + (1-D) \, tanh \left(\frac{1}{(\varepsilon+S)^c} \right) \right]}}_{\text{Strain softening term}}$$

$$\text{With } D = 1 - \left(\frac{T}{T_m} \right)^d \text{ and } S = \left(\frac{T}{T_m} \right)^b$$

The strain softening term is dependent on temperature and strain. This model also includes modifications to the strain hardening part of the JC model. The constants a, b c and d are materials parameters.

Semiempirical models can represent the flow stress dependency on T, ε, $\dot{\varepsilon}$ within a given range using limited number of experimental data [84,85,86,87].

One of the most widely used models for summarising and extrapolating experimental data is the hyperbolic-sine Arrhenius type approach of **Sellars and Tegart** [108], as used for modelling of γ-TiAl by Schwaighofer et al. [109] The strain rate is expressed as a function of temperature and flow stress as shown in Eq. 6.

$$\dot{\varepsilon} = Asinh(\alpha\sigma)^n e^{\frac{-Q}{RT}} \qquad \text{Eq. 6}$$

Where A is a material constant, α is the stress level of power-law breakdown, n the stress exponent, Q the activation energy (work hardening, DRV, DRX and dynamic phase transformations), R is the gas constant and T is the absolute temperature. The experimental data from the flow curves are used for the determination of the parameters n and Q. This equation is valid for a constant strain.

2.4 Deformation maps

Deformation mechanism maps are useful tools to present the dominant deformation mechanisms for given test conditions in one diagram. Frost and Ashby [110] proposed deformation mechanism maps suitable for low strain rates based on creep mechanisms [110]. These maps were developed for pure metals or simple alloys under steady-state creep conditions.

Raj [111] worked on the concept of Ashby's map to construct a damage map suitable for pure metal and dilutes alloys. Prasad et al. [112] proposed the processing maps based on their theory called dynamic materials model (DMM). These processing maps were developed to design and optimise hot deformation processes. They describe microstructural evolution mechanisms and flow instability domains under certain conditions providing optimum deformation temperature and strain rate ranges [112]. In spite of their wide spread use, processing maps theory lacks scientific rigorousness [111,112,113,114]. In this work, the theory is presented and the maps are constructed. Their application and meaning are discussed in chapter 5.3.

2.4.1 Dynamic material model and processing maps

Prasad et al. [112] developed the dynamic materials model (DMM), based on the fundamental principles of continuum mechanics of large plastic deformation. DMM is essentially a continuum model and it is developed from:

1. The continuum mechanics at large plastic flow, where the material is considered to be a **dissipator of power** and not a storage element. This is true at high temperatures and large deformations, where steady state or softening occurs [117].
2. The relation between flow stress and strain rate is **non-linear** for a wide range and therefore the workpiece is considered as a non-linear dissipator of power. The power content and co-content concepts for dissipator elements are applied to mechanical, electrical and magnetic systems after Wellstead [118].
3. The system is considered as **dynamic**, which means it depends on strain rate as an independent variable [119].
4. The system is **not in equilibrium conditions** because the strains are not imposed in infinitesimally small increments and the strain rates applied in metal forming are large.
5. The concepts of **irreversible thermodynamics must be applied**, where the rate of entropy production is used to characterise the behaviour of irreversible processes [119]. The system is considered to be irreversible because the workpiece undergoes large plastic deformation.

The entropy production rate during hot deformation of a workpiece consists of two parts: "internal" and "external" entropy rate. Malvern [120] has shown that the total power dissipation P is related to the internal entropy production rate which is positive for irreversible processes such as plastic deformation.

$$P = \sigma\dot{\varepsilon} = \frac{d^i S}{dt}T \geq 0 \qquad \text{Eq. 7}$$

Where σ is the effective stress, $\dot{\varepsilon}$ is the effective strain rate and $\frac{d^i S}{dt}$ is the rate of internal entropy production. The power dissipates in the material as heat due to microstructural changes.

In the DMM the power of dissipation P is separated into two contributors, G and J, expressed for uniaxial compression as:

$$P = \sigma\dot{\varepsilon} = \int_0^{\dot{\varepsilon}} \sigma d\dot{\varepsilon} + \int_0^{\sigma} \dot{\varepsilon} d\sigma = G + J \qquad \text{Eq. 8}$$

G co-content dissipator has been interpreted as the thermal transport across the sample due to the plastic deformation, and J co-content the dissipation due to microstructural changes. In the DMM microstructural changes include recovery, recrystallisation, material damage, phase transformations, cavity formation and superplastic flow [121].

Figure 10 (a) shows the relationship of G and J for an ideal linear dissipator (J=G) and (b) for a non-linear dissipator for constant strain and temperature.
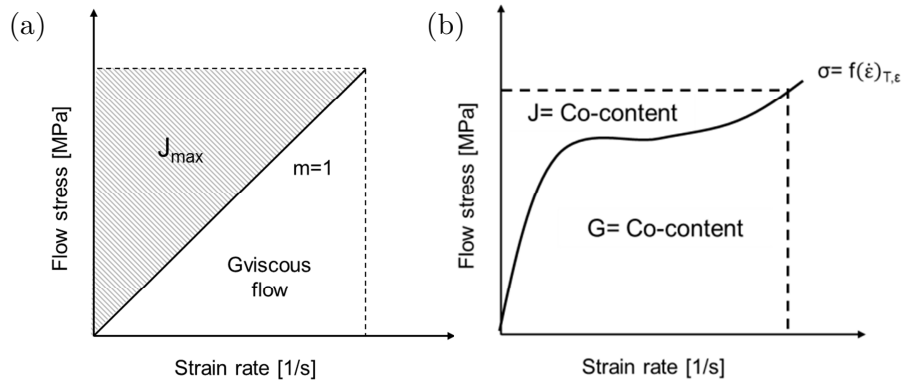
Figure 10: Schematic diagram of P divided into the contributors G and J (a) m=1 and (b) m<1.

The strain rate sensitivity m can be expressed as a function of G and J:

$$m = \left(\frac{\partial J}{\partial G}\right)_{\varepsilon,T} = \left[\frac{\partial(\ln\sigma)}{\partial(\ln\dot{\varepsilon})}\right]_{\varepsilon,T} = \frac{\partial\sigma}{\partial\dot{\varepsilon}}\frac{\dot{\varepsilon}}{\sigma} \qquad \text{Eq. 9}$$

At a constant temperature and strain, the dynamic response of the workpiece under hot deformation can be represented by the power law as follows [112]:

$$\dot{\varepsilon} = K'\sigma^{\left(\frac{1}{m}\right)} \qquad \text{Eq. 10}$$

The integration of J using the power law and considering m as a constant results in the following equation:

$$J = \frac{\sigma m \dot{\varepsilon}}{m+1} \qquad \text{Eq. 11}$$

The maximal J value (J_{max}) that a material can achieve occurs when it behaves as a linear dissipator, meaning when m=1. In this case J_{max} is equal to P/2, as shown in Figure 10 (a).

The processing maps consist of two superimposed maps: the efficiency map and the instability map at a constant strain value and as a function of temperature and strain rate. A good hot formability of the material is indicated by high values of power dissipation efficiency and lack of instabilities.

2.4.2 Efficiency of power dissipation

The ratio between J and J_{max} is defined as the efficiency of power dissipation η_P. Using Eq. 10 and Eq. 11, η_P developed by Prasad et al. [122] is calculated by:

$$\eta_P = \frac{J}{J_{max}} = \frac{2m}{m+1} \qquad \text{Eq. 12}$$

Variation of η_P with temperature and strain rate constitutes the power dissipation map.

Murty and Rao proposed [123] a modification to the η_P calculation, because the strain rate sensitivity m cannot be considered as constant with respect to temperature and strain rate. Therefore J cannot be calculated based on Eq. 11 [118,82]. The calculation of η_{MR} is performed by calculating G, using $\dot{\varepsilon}_{min}$ as the minimum strain rate measured experimentally.

$$G = \int_0^{\dot{\varepsilon}_{min}} \sigma d\dot{\varepsilon} + \int_{\dot{\varepsilon}_{min}}^{\dot{\varepsilon}} \sigma d\dot{\varepsilon} \qquad \text{Eq. 13}$$

The first integral is estimated by using the power law and m equal constant:

$$\int_0^{\dot{\varepsilon}_{min}} \sigma d\dot{\varepsilon} = \int_{\dot{\varepsilon}_{min}}^{\dot{\varepsilon}} K\dot{\sigma}^m d\dot{\varepsilon} = \left[\frac{\sigma\dot{\varepsilon}}{m+1}\right]_{\dot{\varepsilon}=\dot{\varepsilon}_{min}} \qquad \text{Eq. 14}$$

Then η_{MR} is calculated by Murty and Rao [121] by means of equations 12, 13 and 14.

$$\eta_{MR} = \frac{2J}{P} = \frac{2(P-G)}{P} \qquad \text{Eq. 15}$$

2.4.3 Flow instability modelled using DMM

Instability maps are developed on the basis of an instability criterion derived from the extreme principle of irreversible thermodynamics and applied to continuum mechanics at large plastic flow.

Flow instability is determined by the maximum entropy production during deformation, expressed by the Ziegler instability criterion [125]:

$$\frac{\partial D}{\partial \dot{\varepsilon}} < \frac{D}{\dot{\varepsilon}} \qquad \text{Eq. 16}$$

In this case D is the dissipation function. When D=P, which means both, G and J, contribute to the dissipation, instability is given by m<0 as pointed out in [126].

When J and G can be decoupled and D=J could represent the microstructural dissipation, unstable flow occurs when $\frac{\partial J}{\partial \dot{\varepsilon}} < \frac{J}{\dot{\varepsilon}}$. Therefore the dimensionless instability parameter ξ was developed by Prasad et al. [127] as a function of T and ε̇. Instability is predicted when:

$$\xi = \frac{\partial ln[m/(m+1)]}{\partial ln\dot{\varepsilon}} + m < 0 \qquad \text{Eq. 17}$$

Based on the same assumption (D=J), Rao and Murty proposed flow instabilities, when K is negative:

$$K = \frac{2m}{\eta} + m < 0 \qquad \text{Eq. 18}$$

One the other hand Poletti et al. [128] used Eq. 19 to predict flow instabilities

$$K_J = \frac{\partial lnJ}{\partial ln\dot{\varepsilon}} - 1 < 0 \qquad \text{Eq. 19}$$

2.4.4 Processing maps of TiAl

Many researchers [105,106,107,108,109] used DMM to calculate processing maps for different TiAl alloys. Schwaighofer et al. [109] have calculated processing maps for a TNM–C–Si alloy deformed at temperatures 1150-1300°C and strain rates 0.005-0.5s^{-1}. They have reported that instabilities such as wedge cracks are formed at processing conditions of 1150-1200°C and 0.05-0.5s^{-1}. According to them, stable flow behaviour can be observed at temperatures between 1250 and 1300°C and at strain rates between 0.005-0.05s^{-1}, where DRX occur in α and γ phases [109].

Liu et al. [130] have calculated processing maps after Prasad for a Ti-45Al-7Nb-0.4W-0.15B alloy in the as-cast state at a true strain of 0.7. The calculated processing map with the correlated microstructure images is shown in Figure 11. They have reported that high power dissipation values can be found at temperatures between 1000 and 1200°C and a strain rate range of 0.05-0.001s^{-1}. High strain rates of 0.1-1s^{-1} show a low power dissipation range. The specimen deformed at 1000°C and a strain rate of 1s^{-1} revealed cavities at grain boundaries and inside the lamellae. They suggested that under these deformation conditions the stress can only be released by crack formation. They also found cavities between boundaries and lamellar colonies and at the β phases. At temperatures above 1200°C no cracks were found in the surrounding area of the β phase, due to good deformation of the β phase and therefore cracks were prevented. High strain rates are furthermore characterised by lamellar kinking. High power dissipation efficiency is correlated to DRX and globularization of γ lamellae. In summary they have proposed that optimal processing conditions are in the low strain rate ranges [130].
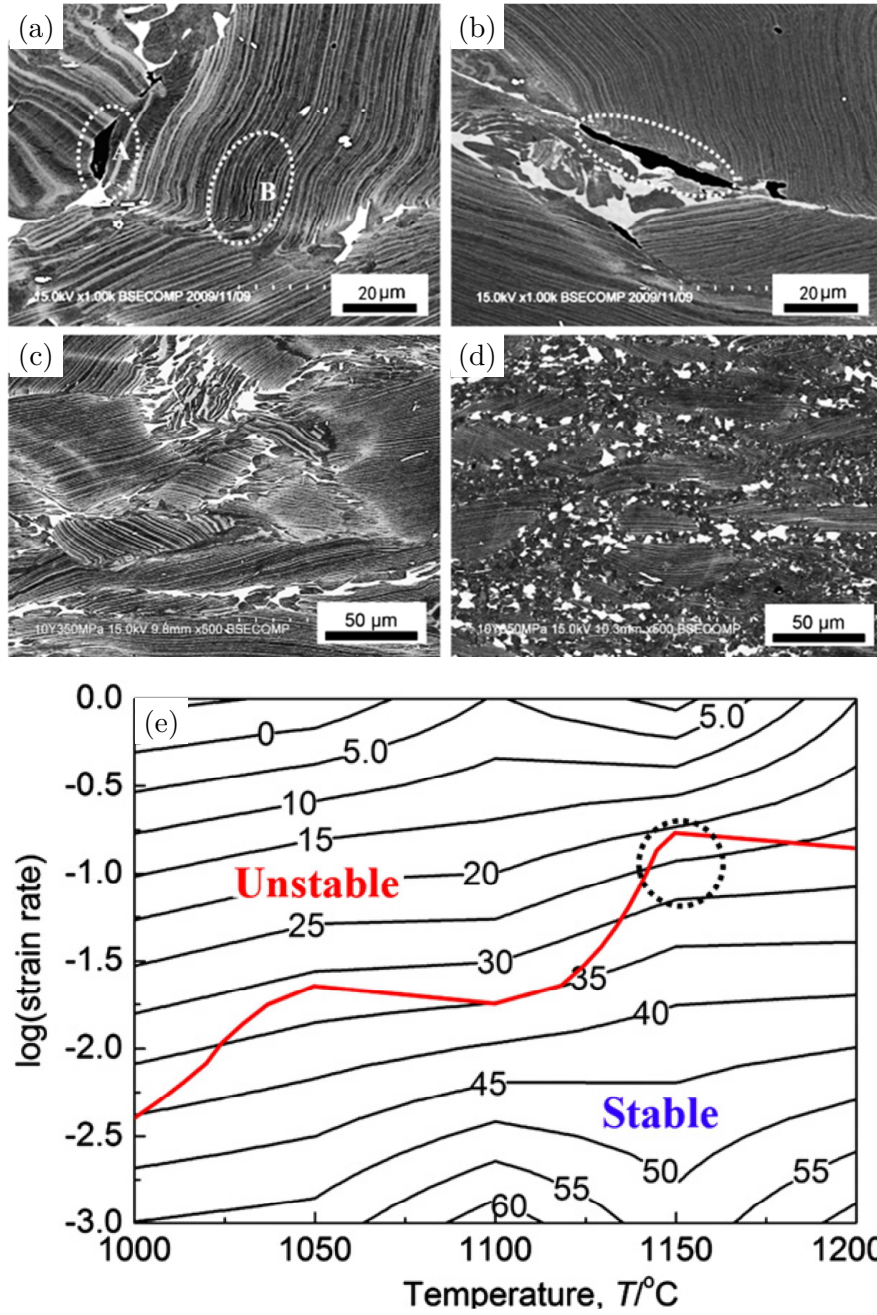
Figure 11: SEM images of Ti-45Al-7Nb-0.4W-0.15B alloy deformed at (a) 1000°C, 1s^{-1}, (b) 1050°C, 1s^{-1}, (c) 1200°C, 1s^{-1} and (d) 1200°C, 0.001s^{-1} and (e) processing map calculated after Prasad at a true strain of 0.7 [130].

2.5 Flow localisation models

The first plastic instability criterion was proposed by **Considère** [133] in 1885. This criterion facilitates to determine the onset of flow instability due to the neck formation in tensile specimens. During deformation the dislocation density increases as well as work hardening and thereby the force on the sample increases and the cross sectional area decreases. The start of flow localisation i.e. necking is defined as the point where the strain hardening rate is equal to the stress.

$$\gamma_c = \frac{\partial \sigma}{\partial \varepsilon} = \sigma \qquad \text{Eq. 20}$$

Many researchers [133,134] have shown that this criterion is only suitable for materials with continuously work hardening.

Hart [136] proposed to modify the Considère criterion in order to consider visco-plastic behaviour, i.e. strain rate sensitivity. The deformation is defined to be stable when:

$$\gamma_H + m > 1 \qquad \text{Eq. 21}$$

Semiatin and co-workers [87] suggested a flow localisation parameter α_{SJ} based on strain hardening and strain rate sensitivity. The parameter α_{SJ} is based on the Hart and Considères criterion. The axial force F through the cylindrical specimen is constant, when there are no inertial effects, which means that dF/dx=0 with x as the axial coordinate. In axial stress conditions the axial force is F=σA with A being the cross-section area of the workpiece and σ_1 the axial principal stress. At any time t, force equilibrium requires that:

$$\left(\frac{\partial lnF}{\partial x}\right)\Big|_t = 0 = \left(\frac{\partial lnA}{\partial x}\right)\Big|_t + \left(\frac{\partial ln\sigma}{\partial x}\right)\Big|_t \qquad \text{Eq. 22}$$

The normalised gradient in the cross section at any given time can be expressed in terms of the variation in initial cross section A_0 and the total strain ε at any point using the constant volume assumption.

$$\left(\frac{\partial lnA}{\partial x}\right)\Big|_t = \left(\frac{dlnA_0}{dx}\right) - \left(\frac{\partial \varepsilon}{\partial x}\right)\Big|_t \qquad \text{Eq. 23}$$

A_0 can be considered as constant, when there are no geometric or machining imperfections.

A dependence $\sigma = \sigma(\dot{\varepsilon}, \varepsilon, T)$ is assumed, where the influence of each of $\dot{\varepsilon}$, ε and T can be described as independent of the other two. Any variation in flow stress of the material, dσ, is considered to be:

$$d\sigma = \left(\frac{\partial \sigma}{\partial \varepsilon}\right)\Big|_{T,\dot{\varepsilon}} d\varepsilon + \left(\frac{\partial \sigma}{\partial \dot{\varepsilon}}\right)\Big|_{\varepsilon,T} d\dot{\varepsilon} + \left(\frac{\partial \sigma}{\partial T}\right)\Big|_{\varepsilon,\dot{\varepsilon}} dT \qquad \text{Eq. 24}$$

The effect of deformation parameters on flow localisation can be determined by Eq. 24. The first term is destabilising at hot working temperatures if flow softening occurs. The second term is usually stabilising because it represents the strain rate sensitivity. If low localisation

starts, material tends to deform faster, strain rate increases and therefore stress increases. The third term is typically destabilising due to thermal softening. The strain and the thermal terms are assembled together and a normalised, constant strain hardening rate γ' (softening parameter) is defined as:

$$\gamma' = \left(\frac{1}{\sigma}\frac{d\sigma}{d\varepsilon}\right)\bigg|_{\dot{\varepsilon}} = \frac{\left(\frac{\partial\sigma}{\partial\varepsilon}\right)\big|_{\dot{\varepsilon},T} d\varepsilon + \left(\frac{\partial\sigma}{\partial T}\right)\big|_{\varepsilon,\dot{\varepsilon}} dT}{\sigma d\varepsilon}$$

Eq. 25

The second term on the right hand side of Eq. 22 is found to be:

$$\left(\frac{\partial ln\sigma}{\partial x}\right)\bigg|_t = \gamma'\left(\frac{\partial\varepsilon}{\partial x}\right)\bigg|_t + m\left(\frac{\partial ln\dot{\varepsilon}}{\partial x}\right)\bigg|_t$$

Eq. 26

The combination of equations in Eq. 22, Eq. 23 and Eq. 26 results in:

$$m\left(\frac{\partial ln\dot{\varepsilon}}{\partial x}\right)\bigg|_t = \left(\frac{\partial\varepsilon}{\partial x}\right)\bigg|_t (1 - \gamma') - \frac{dlnA_0}{dx}$$

Eq. 27

The last expression combines the axial strain rate and strain gradients to the material properties and A_0 (x) which can be formulated as:

$$m\delta ln\dot{\varepsilon} = (1 - \gamma')\delta\varepsilon - \delta lnA_0$$

Eq. 28

The flow localisation parameter α_{SJ} is defined as:

$$\alpha_{SJ} = -\frac{\delta ln\dot{\varepsilon}}{\delta\varepsilon} = \frac{\gamma' - 1}{m}$$

Eq. 29

The parameter α_{SJ} can be used to determine the tendency of a material under different conditions to form flow localisation. This parameter is solely a function of the material properties, γ' and m, which are related to $\dot{\varepsilon}$, ε and T. Generally, materials that show strain hardening or exhibit low flow softening are resistant to flow localisation. Semiatin and his co-workers [86] determined that flow localisation occurs in titanium and its alloys, when α_{SJ} exceeds the value of 5. In general, when α_{SJ} >0.

2.6 Ductile damage models

Ductile fracture can limit the forming processes, and is influenced by the microstructure of a material as well as the process conditions such as deformation rate, strain, temperature, lubrication and friction. Several other factors such as chemical composition and surface conditions can affect ductile failure [137].

The objective of the fracture criterion is to describe the degree of damage during deformation and to predict when fracture occurs. All ductile failure models presented in this work are based on continuum approaches, therefore the defects (pores, precipitates, phases) are considered as homogeneously distributed in the material [138]. Ductile failure models can be divided in macromechanical criteria and micromechanical criteria.

This work focusses on macromechanical damage criteria implementation in the FEM software. Although these models were firstly developed for cold working processes, they are now applied more and more for damage predictions in hot forming processes [139].

These macromechanical models are mostly so-called one parameter criteria, which calculate an accumulated damage value that can be denoted as the critical value at fracture strain. Damage occurs when the damage factor D exceeds the critical damage value D_c, usually determined experimentally.

$$D \geq D_c$$

Cockcroft and Latham model is the most widely used model in metal forming. Cockcroft and Latham [140] proposed that ductile fracture occurs when the integral of the maximum positive principal stress σ_{max} with respect to the equivalent plastic strain ε reaches the critical damage variable D_c.

$$D_c = \int_0^{\overline{\varepsilon_f}} \sigma_{max}\, d\varepsilon \qquad\qquad \text{Eq. 30}$$

The integral represents the internal plastic energy necessary to deform the material until fracture strain $\overline{\varepsilon}_f$ is reached. The material loses its stress-carrying capacities when a critical value of the criterion (D_c) is reached. The expression σ_{max} is equivalent to σ_1. The disadvantage of this model is that the influences of the second and third principal stresses are neglected and thereby the proper damage prediction suffers. In addition the workpiece damage is not only dependent on tensile stresses.

Normalised Cockcroft and Latham: The Cockcroft and Latham criterion is only suitable, when the stress state is purely tensile. Because of this, a normalised version is expressed as:

$$D_c = \int_0^{\overline{\varepsilon_f}} \frac{\sigma_{max}}{\sigma}\, d\varepsilon \qquad\qquad \text{Eq. 31}$$

Freudenthal [141] proposed a formulation based on the plastic work of deformation, calculated using equivalent stress σ instead of the first principal component in contrast to Cockcroft and Latham. Freudenthal criterion is based on von Mises stress and strain values.

$$D_c = \int_0^{\overline{\varepsilon_f}} \sigma \, d\varepsilon \qquad \text{Eq. 32}$$

The model proposed by **Brozzo et al**. [142] (Eq. 33) is characterised by the explicit dependency of both levels of the first principal stress component and the hydrostatic stress σ_H (mean stress) by means of a modification of the Cockcroft and Latham criterion:

$$D_c = \int_0^{\overline{\varepsilon_f}} \left(\frac{2\sigma_{max}}{3(\sigma_{max} - \sigma_H)} \right) d\varepsilon \qquad \text{Eq. 33}$$

where the hydrostatic stress is defined as:

$$\sigma_H = \frac{1}{3}(\sigma_1 + \sigma_2 + \sigma_3) \qquad \text{Eq. 34}$$

The elements σ_1, σ_2 and σ_3 are the principal stresses.

Ayada [143] proposed a further fracture criterion, which is based on the equivalent stress as well as the mean stress.

$$D_c = \int_0^{\overline{\varepsilon_f}} \frac{\sigma_m}{\sigma} d\varepsilon \qquad \text{Eq. 35}$$

The advantage of these models is that they are simple and fast to implement into numerical simulations. The parameters can be easily derived from experimental investigations. The limitation is that when the state of stress or strain history is too different from experimental observations, these models cannot predict fracture accurately. A further disadvantage is that the macromechanical damage models concentrate on the continuum effects of the macroscopic processes leading to ductile fracture. They provide a simplified condition for fracture and do not consider the gradual increase of ductile damage during deformation [144]. Another disadvantage of these models is that the microstructural changes are not considered. These models should only be used for general damage estimation and considered as qualitative predictions [145].

2.7 Finite element simulation

Finite element is an approximation method for solving problems which are described by partial differential equations. The finite elements are useful for numerical solving of electrical, thermal, magnetic and coupled field problems (multiphysics), where it is nearly impossible to find an analytical solution. The method was developed approximately 60 years ago and it was first applied in aircraft design. In the area of forming the finite element method is used to optimise and develop processing technologies and component design. The method is primarily used to establish scalar and vectorial sizes such as temperature, stress and strains. An essential advantage of FE simulations is that it enables to reduce time and costs [146].

The main objectives of FEM simulations in forging are the development of appropriate die design and determine process parameters by preventing flow-induced defects (laps). The prediction of processing limits is necessary to avoid defects, temperatures to control properties, friction conditions and die wear.
A further objective is to improve product quality and complexity. This in turn could lead to a reduction of production costs by improvements in the microstructure as well as of die tests and lead times. As a minimum goal the analyses of forging load, energy, tool stresses and temperatures can be carried out to avoid tool failure. Moreover, adequate forging machines can be selected for a given application [147].

Nowadays many commercially available programmes such as ABAQUS, DEFORM, FORGE and Qform can be used for finite element simulations of massive deformation requirements. These finite element programs are mostly written in the programming languages FORTRAN or C [148]. When forging process simulations are carried out the following aspects have to be considered in order to avoid problems: friction, large deformations, mechanical properties change of metals, heat generation due to mechanical work and thermal exchange between workpiece and environment. These phenomena cause non-linearities in the system that make it difficult to solve appropriate the problems by mathematical modelling [149]. Furthermore limitations arise from the fact that in most simulations the tools are considered as rigid and die deformations and stresses are ignored. One general limitation of FEM is that the accuracy of the obtained solution is usually described as a function of the mesh resolution. The areas of highly concentrated stresses should be carefully analysed with the use of a refined mesh.

3 Methodology

This chapter gives an overview of the experiments, the models used and the finite element simulations. The focus is on the description of the investigated material, the metallographic methods and the compression tests. A wide range of experimental techniques were used for the microstructural characterisation including light optical microscopy (LOM), scanning electron microscopy (SEM), energy dispersive X-ray (EDX) analysis, X-Ray diffraction (XRD) and electron backscatter diffraction (EBSD). The thermomechanical treatments of the alloy and the flow data processing are delineated. The modelling sub-chapter outlines the modelling of the flow behaviour and the use of macro- and micromechanical damage models. The finite element (FE) part focusses on the characterisation of the 2D simulations set-up and the input data.

3.1 Investigated material

The investigated material was the TNM alloy with a nominal chemical composition of Ti-43.5Al-4Nb-1Mo-0.1B at%. It was provided by GfE Metalle and Materialien GmbH, Nuremberg and RTI International Metals LTD. The material provided by GfE was produced by vacuum arc re-melting (VAR) and then centrifugally casted into ingots. In order to ensure sufficient alloy homogeneity, the material was double melted. The residual casting porosity was reduced by hot isostatical pressing (HIPing) at 1205°C for four hours under a pressure of 175 MPa followed by furnace cooling. The material provided by RTI was produced by plasma arc melting (PAM), followed by vacuum induction melting (VIM) and finally hot isostatical pressed.

Figure 12 (a) shows the cross-section of the ingots. The cylindrical compression specimens of 10mm in diameter and 15mm in height were cut from ingots by electron discharge machining (EDM). Figure 12 (b) shows the compression sample arrangement in the longitudinal direction of the ingot.
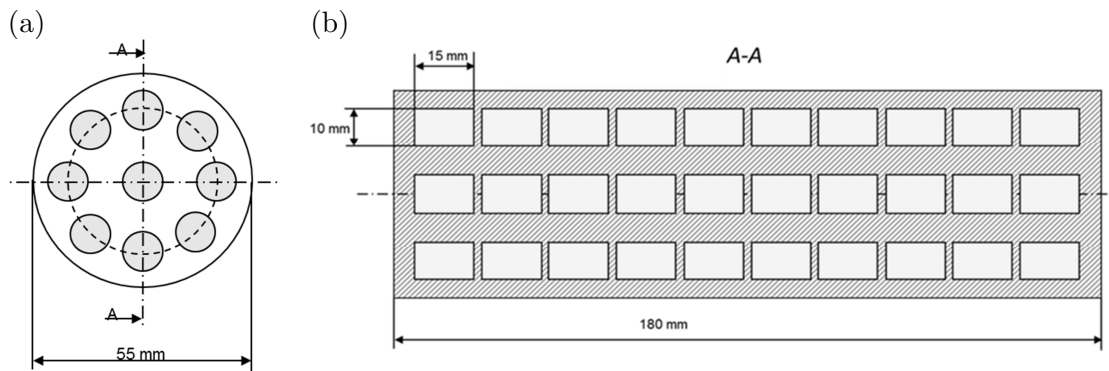

Figure 12: Sample arrangement of the ingot (a) cross-section and (b) in longitudinal direction.

3.2 Microstructural characterisation

3.2.1 Metallography

The deformed specimens were cut along their axis parallel to the direction of compression by means of a wet grinder and were warm embedded (DuroFast® epoxy resin) using the CitoPress20 device (Struers). Subsequently, grinding was performed by semi-automatically TegraPol 21 (Struers). The specimens were placed on a six sample holder, grounded flat with a silicon carbide grinder (grit 80) and then fine ground (80/force 120N, 120/force 100N, 320, 500/force 80N, 800, 1200/force 60N, 2000 and 2400/force 120N). They were cleaned with water and ethanol after each grinding step. The specimens were cleaned in an ultrasonic bath for 10min after the grinding procedure. They were mechanically polished using a colloidal silica solution (OP-S, Struers) for 5min with 30N on a MD-Chem polishing disk and subsequently cleaned in ultrasonic bath for 10min. After this procedure they were electro-etched using Ence and Margolin's etchant according to [150] and observed in LOM using polarised light illumination. The colour etchant permits to obtain information about the orientation of the phases. The chemical composition of the colour etchant was 420ml of ethanol 95vol.-%, 245ml of distilled water, 70ml of lactic acid, 35ml of ortho-phosphoric acid 85vol.-%, 35g of solid citric acid and 35g of solid oxalic acid. The electrolytically etching was carried out using a mask with an area of 2cm^2, a flow rate of 10, a voltage of 39V and an etching time of at least 10s. After applying the colour etching Ence and Margolin the α_2/γ colonies changed to a colour between brown and yellow, while the globular γ phase appeared between blue and violet. The β_o phase appeared in a light yellow colour.

An alternative preparation method, which was applied after mechanical grinding, was chemical-mechanical polishing with 90vol.-% Struers OP-S + 10vol.-% H_2O_2. The advantage of chemical-mechanical polishing in comparison to electrolytic polishing is that less material abrasion takes place and therefore the damage produced during hot deformation process could be investigated without adding any preparation artefact.

Scanning electron microscope samples were manually ground and polished by vibration using a colloidal silica suspension from LECO (Colloidal Silica CS005) in order to avoid pores closing by wear and material transport.

Deformed samples were prepared for metallographic investigations as shown in Figure 13. Figure 13 shows schematically (a) the specimen before deformation and force direction, (b) the cutting axis of the deformed specimen and (c) the analysed zones of compressed samples (marked by squares).
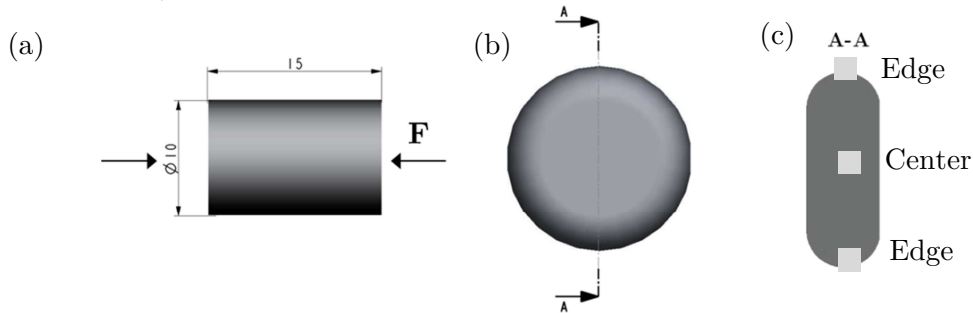

Figure 13: (a) Initial specimen and applied force direction (b) parallel cutting to the deformation direction and (c) analysed zones by LOM and SEM (marked by squares).

3.2.2 Microscopy

The investigations by optical microscopy focussed on the characterisation of phase morphology, TiB precipitates, as well as damage and flow localisation in the deformed specimens. For this purpose a fully motorised inverse light microscope from Carl Zeiss and the ZEISS AxioVision software were used.

Due to the limitations of LOM pores smaller than 1µm were hardly distinguishable from TiB precipitates, therefore a scanning electron microscope (LEO 1450VP, Zeiss) was used for a more detailed analysis. This device was equipped with a tungsten filament. The SEM was operated in back scattered electron mode (BSE) to achieve phase contrast. The BSE mode allows distinguishing between the three phases in the γ-TiAl alloy due to their chemical composition with different atomic numbers. Therefore, the β phase with the heaviest elements such as Nb and Mo appeared brighter than the two other phases with lower density elements (β>α>γ). The precipitates and micro cracks were further characterised using an In-lens detector to provide topographical information. As the distinction between the ordered and disordered β by means of SEM was not possible a field emission gun scanning electron microscopy was used because it provides higher resolution, higher brightness and lower energy spread in contrast to conventional SEM [151]. The investigations with high-resolution FEG-SEM were carried out using two different devices of Zeiss-Ultra-55 (FELMI Graz and HZG Germany). In order to gain information about local chemical composition EDX mapping was carried out.

3.2.3 X-Ray diffraction measurements

For X-Ray diffraction measurements (at room temperature) of the as-received and deformed specimens a Siemens D5005 diffractometer with Cu Kα radiation over a range of 25°<ϴ<70° was used. Measurements were performed in Bragg-Brentano geometry and the radiation used had a wavelength of 1.5406Å. The peaks of the phases were identified by means of literature data [133]. All measurements were performed at FELMI Graz.

3.2.4 Electron backscatter diffraction

Electron backscatter diffraction (EBSD) is an unique technique for characterising the crystallographic orientation, grain and substructure, local texture and orientation relations [152]. In contrast to conventional methods, EBSD provides the advantage of analysing the grain boundary types [153]. A schematic illustration of the EBSD measurement system is depicted in Figure 14. The accelerated and focused electron beam hits the tilted specimen and the Kickuchi diffraction patterns on phosphor screen are acquired with a CCD camera. Further investigations of the patterns are performed by means of an automatic routine [154].
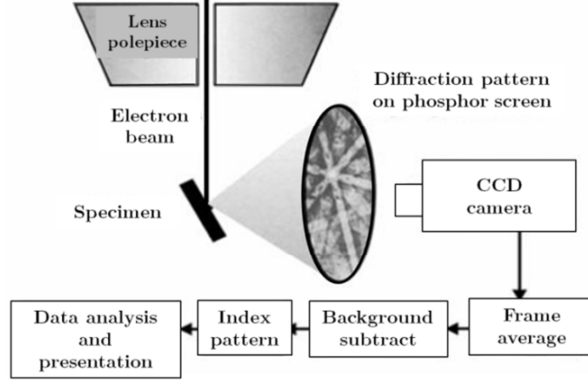
Figure 14: Schematic illustration of the EBSD measurement system [154].

In the present study, EBSD measurements were carried out using a Zeiss Ultra 55 FEG-SEM equipped with a CCD Digiview camera from EDAX-TSL. The EBSD measurements were performed on selected areas of hot deformed samples and on the as-received condition. The diffraction patterns were collected with a hexagonal grid at step sizes of 0.1, 0.3, 0.4 and 0.8µm. The size of the EBSD scanned areas were 40x40µm, 50x50µm, 60x65µm, 70x65µm, 70x70µm, 100x100µm and 250x250µm. The Kikuchi patterns were obtained using an acceleration voltage of 20kV and the specimens were tilted to 70°. The diffraction patterns were processed using EDAX-TSL OIM Data Collection 7 software. The used lattice constants to treat the Kickuchi patterns obtained from EBSD measurements are summarised in Table 4. The lattice parameters of the phases in the analysed nominal TNM alloy were established by means of X-Ray diffraction investigations described in 3.2.3. The latter were carried out to characterise the microstructure after thermomechanical treatment.

Table 4: Lattice constants of the phases in TNM alloy used for EBSD (see 4.2.4)

Phase	Space group	Structure	Pearson code	Lattice constants [Å]
α_2-Ti$_3$Al	P 63/m m c 194	D0$_{19}$	tP2	a=4.012 c=4.065
γ-TiAl	P 4/ m m m 123	L1$_0$	hP8	a=2.8 c=4.03
β_o-TiAl	P m-3 m 221	B2	cP2	a=3.2

At first the raw EBSD picture was rotated by 90° around the A3 axe and then 90° around the A1 axe. The data cleaning procedure was carried out using a combination of clean-up steps. Problems appeared during automatic indexing of the phase with tetragonal crystal structure. The EBSD data of TNM alloy were indexed with errors due to its cubic pseudo-symmetry. The c/a ratio of γ-TiAl is too close to the unity so the EBSD patterns of γ-TiAl exhibit a pseudo-cubic symmetry. Therefore the position of the c axis cannot be identified by standard algorithms [155]. Other studies often used a cubic crystal symmetry to index the TiAl phase, but this does not allow for a distinction between order variants [52].

Figure 15 shows the schematic illustration of the clean-up procedure for the γ-TiAl alloy on the basis of an exemplary EBSD data. Firstly, the raw data was corrected with a pseudo-symmetry clean-up of the γ phase with an angle of 90° with 1° tolerance and subsequently the clean-up procedure neighbour orientation correlation was applied. With this cleaning method, the misorientation within γ was lost. The neighbour orientation correlation method changes the orientation of a pixel to match the orientation to which the majority of its neighbours belong. After rotation and clean-up the maps were calculated.
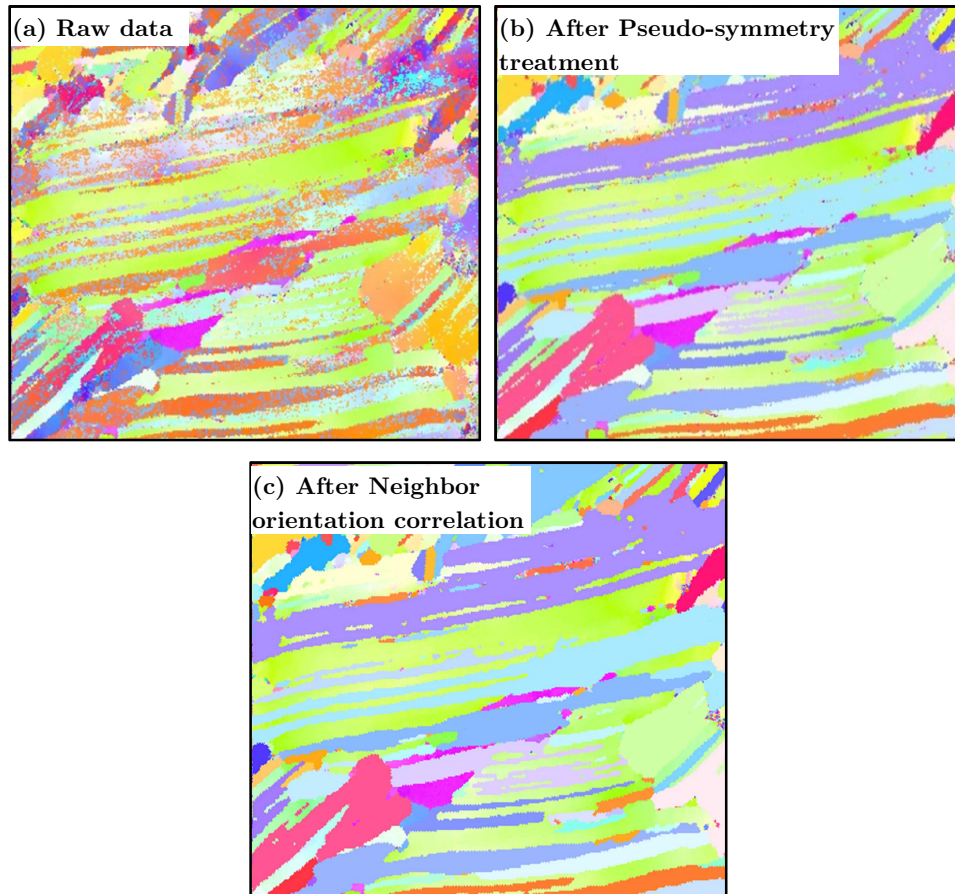

Figure 15: Illustration of the applied clean-up procedure of γ-TiAl (a) raw data, (b) pseudo-symmetry correction of γ-TiAl phase with 90° and the final step (c) neighbour orientation correlation.

3.2.5 Microstructural features quantification

The quantification of the phases in the as-received, heat treated and hot compressed conditions were carried out by means of scanning electron micrographs using the software Image J [156]. For quantitative analysis SEM micrographs were taken from two different positions of the specimen and the average value was calculated. An explicit quantification of the α_2 and γ colonies was not feasible by means of the software Image J. The methods for the quantification of the phases by Image J are described in [157].

3.3 Compression tests

The hot compression tests were carried out on a thermomechanical simulator Gleeble®3800. Gleeble®3800 is capable of performing deformation experiments under precisely controlled conditions of temperature, strain and strain rate.

By using the basic Mobile Conversion Unit (MCU) high heating rates and slow strain rates can be achieved. The pocket jaws are designed for tensile tests and there are limits for compression tests. In order to stop at a specific strain a hydraulic system was used to stop the piston. This causes a declaration period which affects the results. In contrast to the basic Module the Hydrawedge MCU provides a system for high strain rates up to 100/s with short interpass times and with an independent control of strain and strain rate. However, factors like load cell ringing can be a problem at strain rates above 50/s.

The Hydrawedge MCU is further limited by a heating rate of 5°C/s [158]. The compression test arrangement in the Gleeble® is schematically shown in Figure 16. The samples were placed between two anvils. The temperature of the specimen was measured and regulated by a type S (PtRh-10%/Pt) thermocouple of spot welded in the centre of the specimens. Another thermocouple was used 1mm from the edge of the sample to record the temperature gradient in the longitudinal direction. Resistance heating was used to attain the desired temperatures.

Many methods have been tried in order to reduce the effect of friction and thermal gradient on the specimen [87]. In order to reduce the effect of friction and thermal gradient, a combination of Ni based suspension and graphite and Mo foils was located between sample and anvils. Mo is characterised by poor thermal and electrical conductivities [159]. On the other hand, graphite decomposes at higher temperatures (>600°C) and Mo acts as a barrier for carbon diffusion into the sample.

In all performed hot compressions tests, deformation was measured in the length direction. The stroke includes both the length change of the specimen and the machine's maximum compliance. In this work the length change of the specimen was measured from one jaw to the other jaw by means of jaw-to-jaw transducer (L-Gauge) [158]. Axial compression force, temperature, L-Gauge and stroke were measured continuously during compression tests.
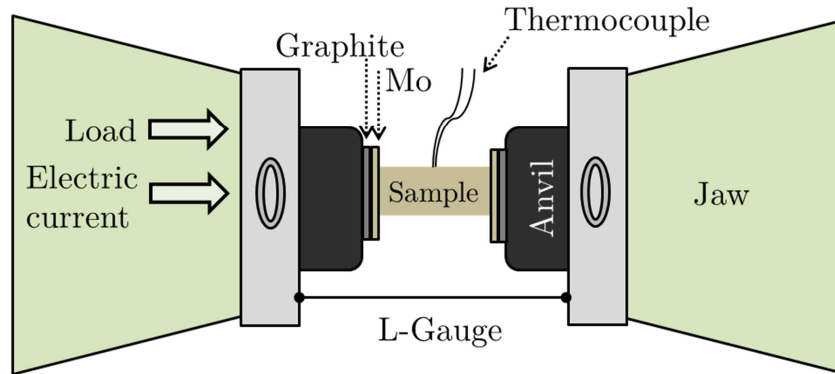

Figure 16: Scheme of the compression test arrangement in the Gleeble machine (MCU Hydrawedge).

Hot compression tests were carried out at deformation temperatures between 1140°C and 1340°C, at constant strain rates between 0.005s^{-1} and 1s^{-1} up to a total true plastic strain of 0.9 on cylindrical samples of 15mm length and 10mm diameter. Three thermal cycles were applied as a function of time and called *fast*, *slow* and *isothermal*, as shown in Figures 17. The *fast cycle* was carried out using the basic MCU in an evacuated chamber.

In the *fast cycle,* shown in Figure 17 a.1, the sample was heated at 17°C/s to 1300°C, cooled to the deformation temperature (7°C/s), held for 10s or 60s and deformed. After deformation, the specimens were cooled to room temperature by continuous cooling of 2.5°C/s. The temperature time profiles for the deformation temperatures 1300°C and 1340°C are shown in Figure 17 a.2 and a.3, respectively. Samples were heated at 17°C/s up to 1300°C or 1340°C and held for 10s or 60s. Deformation was followed by a controlled cooling at 2.5°C/s. The objective was to be far from equilibrium microstructure.

The *slow cycle* was performed in Hydrawedge in a protective Ar atmosphere. For the *slow cycle* a heating rate of 5°C/s to 1000°C was used, followed by 2°C/s to 1300°C to avoid overheating. At 1300°C, the samples were soaked for 60s to achieve homogeneous temperature distribution throughout the specimen. After a holding time of 60s at 1300°C the samples were cooled with 1°C/s to testing temperature, held 10s before deformation and subsequently free cooled under argon atmosphere with an average cooling rate of 10°C/s. The compression tests carried out at 1300°C and 1340°C, are illustrated in Figures 17 b.2 and b.3, respectively. The objective of the *slow cycle* was to simulate an industrial process.

The *isothermal cycle* was characterised by a heating rate of 5°C/s to the deformation temperature under Ar atmosphere in Hydrawedge. The schematic temperature time profile is shown in Figure 17 (c). Soaking times were 5min for testing temperatures between 1140-1220°C (Figure 17 c.1), 3min at 1260°C, 1.5min at 1300°C (see Figure 17 c.2) and 1min at 1340°C (see Figure 17 c.3). After deformation microstructure was frozen by water quenching at 1140-1260°C and air cooled at 1300°C and 1340°C. The objective of the *isothermal cycle* was to achieve phase equilibrium with a moderate grain size.
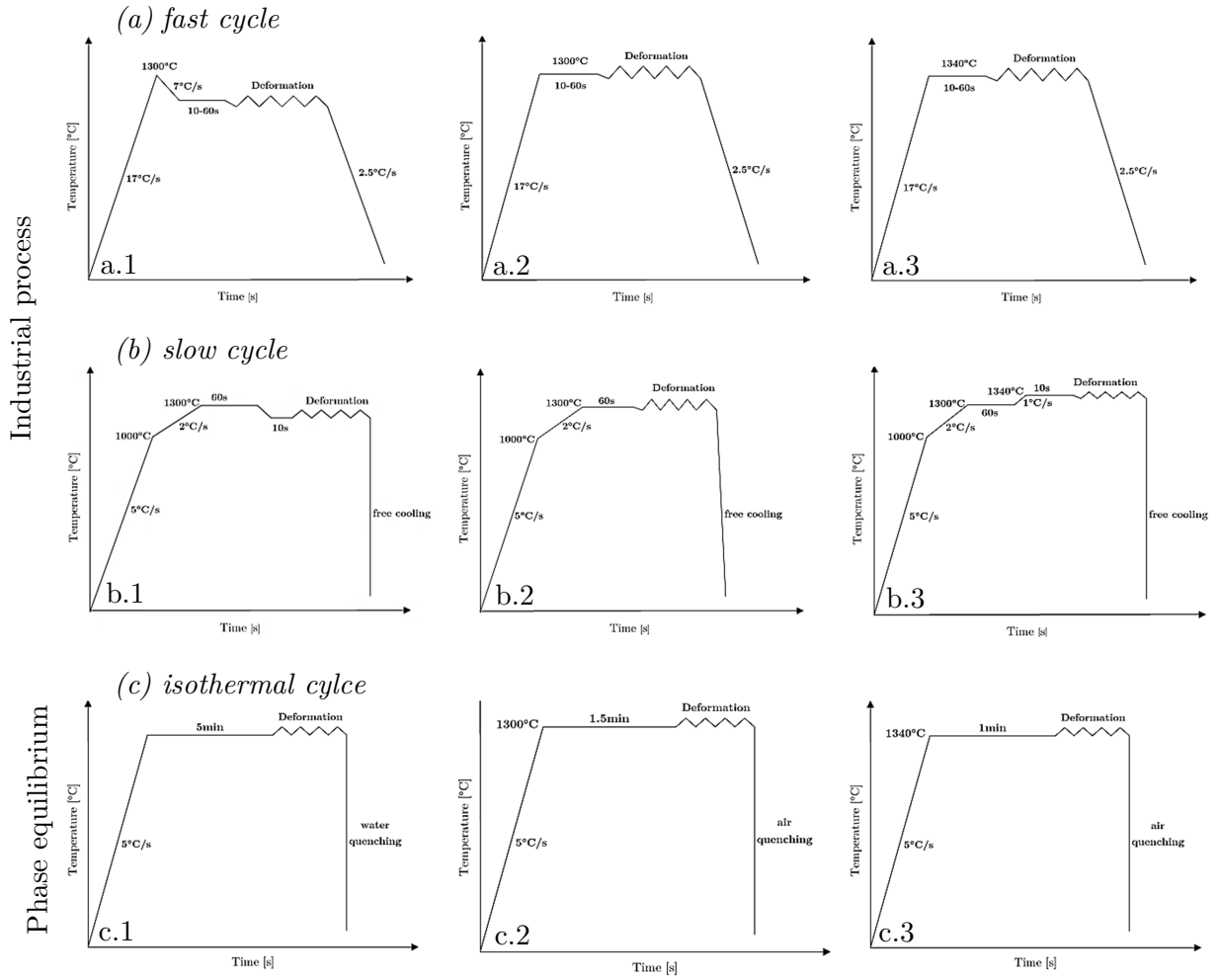
Figure 17: Schematic diagram of thermomechanical test conditions (a) *fast cycle*, (b) *slow cycle* and (c) *isothermal cycle*.

3.3.1 Challenges of working with TiAl

Hot compression tests of the TNM alloy were conducted at high temperatures and therefore many problems turned up, such as contamination of thermocouples, too slow cooling rates, low mechanical resistance of anvils, and incorrect temperature control.

As mentioned above, the *fast cycle* experiments were performed under vacuum. Due to the unexpected microstructures, the S thermocouples were analysed. It could be concluded that the S type thermocouples were contaminated during the tests under vacuum, as verified by EDX measurements. The EDX spectrum confirmed the contamination of the tip with Al. No Al peak was observed a few millimetres far from the tip. Therefore, the compression tests were carried out under Ar atmosphere and a few mm of the thermocouple were cut off the tip before starting every new experiment.

Another challenge when working at higher temperatures is the selection of anvil material, since the tungsten carbide anvils deform during compression tests and their surfaces were worn. TZM (titanium-zirconium-molybdenum) anvils give better results.

Temperature decreases abruptly and cannot be increased again fast enough was solved by modifying the proportional-integral (PI) controller parameters to control the thermal reaction of Gleeble®3800 before and during deformation. A certain amount of compression tests at

34

different testing conditions were carried out to determine the optimal P and I values for the material class used.

Figure 18 shows a comparison of temperature-time profiles under comparable conditions. The green curve was measured with the default settings and the red curve was achieved with P=2 and I=1. The temperature fluctuations with P control turned out to be lower in contrast to the thermal cycle with the default settings.

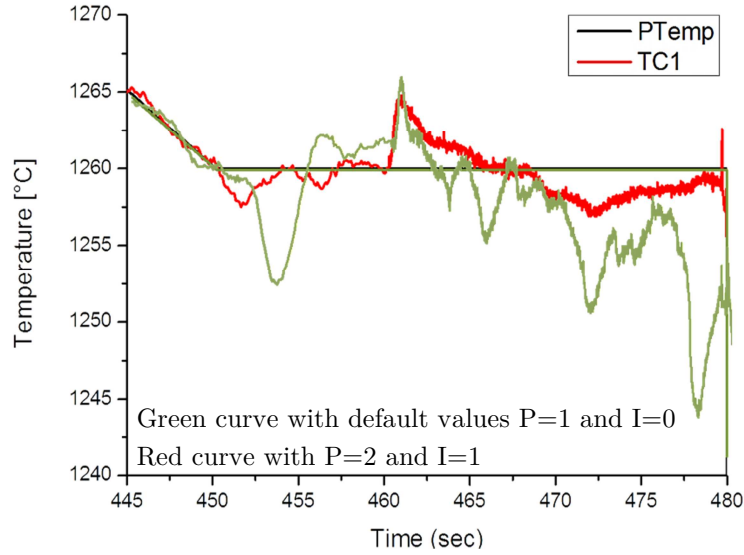Figure 18: Comparison of temperature time cycle (a) green curve with default settings P=1, I=0 control and (b) red curve with P=2 and I=1 control.

Figure 19 shows a comparison of the temperature-time profiles with two different P and I values. P and I controller has shown a dependency on the strain rate and temperature. For the TNM alloy the lowest temperature fluctuations were obtained for P=2 and I=1, as can be seen in Figure 19 (a). If P increases, the fluctuations increase (Figure 19(b)).
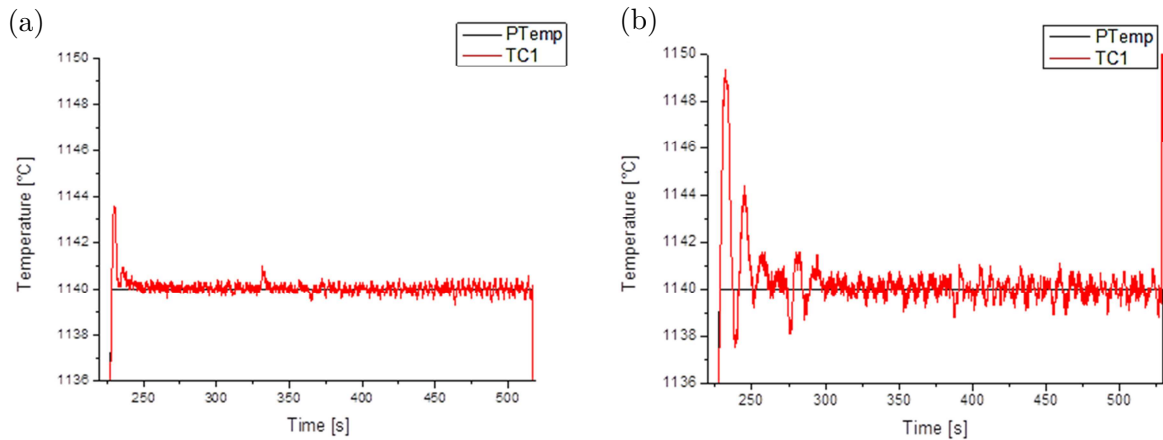

Figure 19: Comparison of temperature-time profiles gained by Gleeble with different temperature control parameters (a) P=2 and I=1 and (b) P=3 and I=1.

3.3.2 Flow curves calculation

The uniaxial compression tests carried out in the basic MCU of the Gleeble®3800 provided technical strain stress curves, because of the missing length measurement system. The calculation of the true strain and stress was done using the final change in length and in diameter of the specimens. Assuming that strain is homogeneous in the specimen, the true strain ε was calculated using the following expression:

$$\varepsilon = \ln\frac{l}{l_0} = \ln\frac{A}{A_0} = 2\ln\frac{d_{0f}}{d_0} = 2\ln\frac{\Delta d + d_0}{d_0} = \ln(e + 1) \qquad \Delta d = d_f - d_0 \qquad \text{Eq. 36}$$

where d_0 and l_0 are the initial diameter and length of the specimen, respectively and e is the engineering strain. Stress was calculated as relation of applied force (F) to cross sectional area (A) as shown in Eq. 37.

$$\sigma = \frac{F}{A} = \frac{4F}{\pi(\Delta d + d_0)^2} \qquad \text{Eq. 37}$$

The compression tests performed in the Hydrawedge MCU of the Gleeble®3800 were carried out using a L-Gauge measurement system, thus allowing the calculation of true stress vs. strain curves with equations 36 and 37. The constant strain rate is achieved due to the linearization of ΔL by L-Gauge. In order to obtain the plastic strain ε_p, the elastic strain region was removed from every stress-strain curve by using Eq. 38, where E_{ap} is the apparent young modulus corresponding to the initial slope of stress-strain curve.

$$\varepsilon_p = \varepsilon - \varepsilon_e = \varepsilon - \frac{\sigma}{E_{ap}} \qquad \text{Eq. 38}$$

The stress-strain curves have shown irregularities related to the test equipment parameters but not to material properties. In order to eliminate machine noises from the flow curves, common smoothing methods as Savitzky-Golay und adjacent-averaging were applied to the force and change in length data. Savitzky-Golay filters are based on a least-squares digital polynomial filter and the adjacent-averaging filter calculates the average of a number set of data points for each value. The adjacent-averaging smoothing delivered the best-fit shape in this study.

Figure 20 (a) shows a force curve vs. time as measured. The data was smoothed by an adjacent averaging filter, shown in Figure 20 (b). The smoothing techniques mentioned above were implemented in the software Origin®.
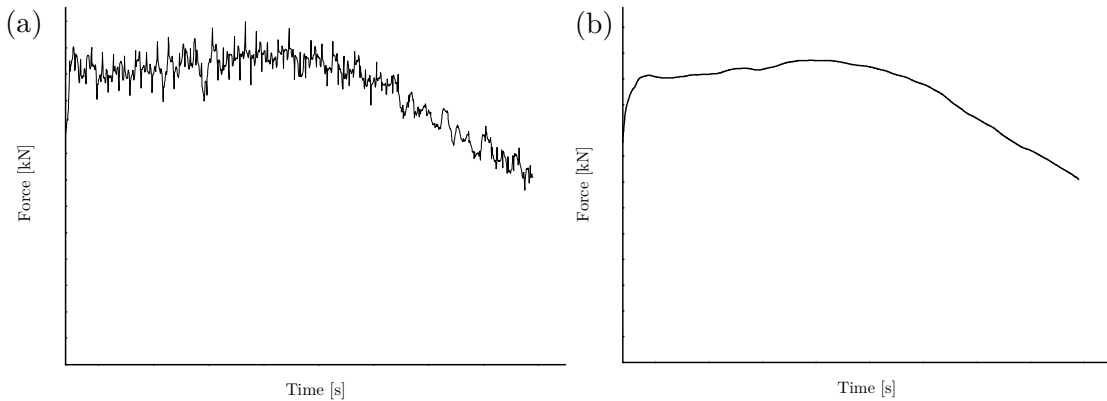

Figure 20: Comparison of (a) curve with machine noise and (b) with an adjacent-averaging smoothed curve.

3.3.3 Calculation of processing- and instability parameters

All parameters were calculated using the experimental flow stress data of the material obtained from *cycles fast*, *slow* and *isothermal*.

High strain rates cause an increment in temperature of the specimen that cannot be dissipated to the surrounding environment due to the short times. Therefore, the corrected flow stress σ^I can be calculated according to Eq. 39 [160].

$$\sigma^I (\varepsilon, \dot{\varepsilon}, T) = \sigma^H (\varepsilon, \dot{\varepsilon}, T) - \left. \frac{\partial \sigma^H (T)}{\partial T} \right|_{\varepsilon, \dot{\varepsilon}} \Delta T \qquad \text{Eq. 39}$$

Where σ^H is the flow stress of the uncorrected curve and ΔT corresponds to the temperature increment. For an adiabatic system, then the increment in the temperature ΔT could be calculated according to Eq. 40.

$$\Delta T = \frac{\eta \int_0^\varepsilon \sigma \, d\varepsilon}{\rho C p} \qquad \text{Eq. 40}$$

Where η, Taylor-Quinney parameter, is the efficiency of deformation heating, the integral corresponds to the area under the uncorrected stress-strain curve, ρ is the density and Cp the heat capacity of the material. η was considered equal to 0.9.

The maximum temperature increment due to self-heating measured for two temperatures and strain rates is illustrated in Table 5. The highest temperature increment was measured for the lowest temperature 1140°C and the highest strain rate 1s^{-1}. The temperature increment was also calculated based on Eq. 40. In general, the result of calculated temperature increment based on Eq. 40 is higher than the measured ones due to adiabatic assumptions and the selection of a constant Taylor-Quinney parameter η.

Table 5: Measured and calculated temperature increment during deformation.

Set temperature [°C]	Strain rate [1/s]	ΔT [°C]	
		Measured	Calculated
1140	1	20	39
1140	0.005	4	11
1220	1	10	20
1220	0.005	0.4	6

The strain rate sensitivity m was calculated based on Eq. 9. The ln σ versus ln $\dot{\varepsilon}$ for constant T and ε were plotted as a diagram and fitted with a cubic function for each temperature and strain. The cubic function was analytically derived with respect to $\dot{\varepsilon}$ to obtain the m values.

In order to calculate the normalised flow softening parameter γ' (Eq. 25), strain and temperature softening terms were determined. The strain softening term was obtained by fitting the flow curves by a polynomial function. This function was derived and multiplied by the strain. The calculation of the temperature softening term was performed by plotting the stress versus the temperature for every strain rate at a constant strain. This function was

derived and multiplied with the maximal temperature increment. The maximal temperature increment ΔT was measured for all testing condition using thermocouples during deformation.

The calculation of processing and instability maps was done by determining η_P, η_{MR}, ξ, K, K_j, P and J term. The efficiency of power dissipation η_P (see Eq. 12) was calculated from a set of m values at a constant strain.

The instability parameter ξ (see Eq. 17) was determined by plotting $\ln(m/m+1)$ versus $\ln\dot{\varepsilon}$. The curve was fitted by a polynomial function and derived subsequently.

The second term of G (Eq. 13) was obtained by plotting the area under the stress vs strain rate curve as integrated by Origin® software.

The instability parameter K_j (Eq. 19) was subsequently obtained by plotting $\ln J$ versus $\ln\dot{\varepsilon}$. The curve was then fitted by a polynomial function and derived.

All calculated parameters (m, γ, α, η_P, η_{MR}, ξ, K and K_j) were plotted using Origin as isolines contour maps as a function of temperature and ln strain rate at a constant strain.

3.3.4 Heat treatments

Heat treatments were performed in the Gleeble®3800 at several temperatures with two holding times to obtain the evolution of the microstructure as a function of $\dot{T}$, T and t. The thermal cycle *fast* was carried out without deformation under Ar atmosphere. All specimens were heated up above the solvus temperature of the γ phase and then cooled down to temperatures between 1140°C and 1340°C, held for 10s or 60s, and cooled down with 2.5K/s to room temperature.

3.4 Modelling

3.4.1 Plastic flow modelling

The flow behaviour was modelled with an empirical material model. In this study the TANH (hyperbolic tangent) model based on a modification of the JC model was optimised to describe the flow behaviour of the TNM alloy in the studied range. A genetic algorithm (GA) optimisation method developed by Chen et al. [161] was used to optimise the material constants. The flow model TANH was adapted to the flow curves of the *slow cycle.* The optimised TANH model for the nominal TNM alloy is discussed in Eq. 42 (chapter 4.2.1).

3.5 Finite element method

3.5.1 Numerical modelling and simulation of compression tests

The uniaxial compression tests were numerically modelled using the commercial forming software DEFORM™ 2D version 10.2.1 developed by SFTC. This commercially available software is divided in three subprograms, which can be termed preprocessing, simulation and postprocessing [162]. Figure 21 presents an overview of the three main subprograms of the finite element method DEFORM™.
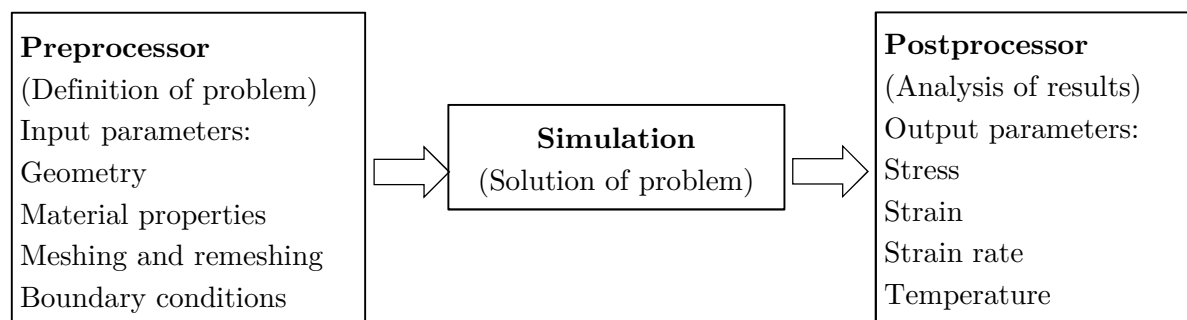
Preprocessor
(Definition of problem)
Input parameters:
Geometry
Material properties
Meshing and remeshing
Boundary conditions

⟹

Simulation
(Solution of problem)

⟹

Postprocessor
(Analysis of results)
Output parameters:
Stress
Strain
Strain rate
Temperature

Figure 21: Schematic diagram of subprograms of the commercial software DEFORM™.

1. *Preprocessing:* In the *pre-processor* the geometry of the workpiece and anvils, the material parameters, the loads and the simulation controls have to be defined. The geometry can be loaded from the extensive tools library or created within the programme or else imported from CAD files by the user. DEFORM™ has a large material database. Additionally, the material database can be created manually by implementing material properties. Many macro- and micromechanical damage criteria such as Cockcroft and Latham, Ayada, McClintock and many others are already implemented in the software. The interaction object conditions must be described also. In this module the friction condition and the heat transfer coefficient between the objects are defined. The database with the defined process conditions and simulation controls is generated [162].

For this study the compression tests with cylindrical specimen of an aspect ratio of 1.5 were set as an axisymmetric non-isothermal model, as shown in Figure 22. The simulations of the compression tests were carried out at the same temperatures and strain rates as the experimental ones. The visco-plastic workpiece was located between two rigid tools. The upper tool was moved at a constant displacement speed as in the real measurements, while the bottom tool was fixed. Before compression the workpiece was heated up by electric resistance heating to the desired deformation temperature. Both tools were subjected to a constant current flux (Amp/mm^2) and were grounded on one side (i.e. zero voltage), as shown in Figure 22. The plastic behaviour of the workpiece was described by the experimental and modelled flow curves. The FEM simulations were performed to simulate the *slow cycle*.
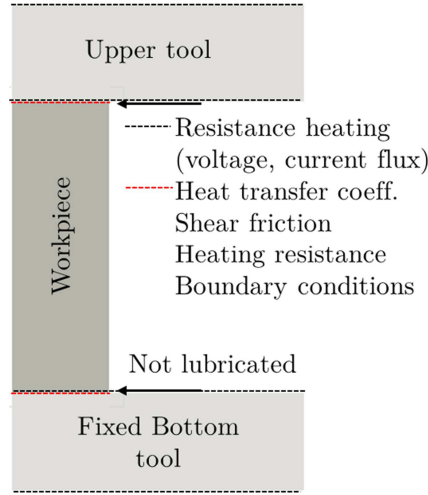
Figure 22: Schematic diagram 2D axisymmetric model of compression test.

Isotropic hardening rule and the von Mises yield's isotropic rule were applied to describe the plastic behaviour. The elastic, thermal, electric and magnetic properties of the nominal TNM alloy were provided by Böhler Schmiedetechnik GmbH & Co KG.

Figure 23 shows the Young's modulus, thermal expansion, thermal conductivity, density heat capacity and electrical resistivity of TiAl as functions of the temperature. The Poisson's ratio and the emissivity value were considered as constant values, as well as the Taylor-Quinney factor was assumed equal to 0.9.

The used amount of elements of the workpiece and the tools together was 3000 elements with a thickness of 4 and a size ratio of 3. Remeshing with a maximum step increment of 5 was applied for the workpiece. The inter-object relation such as friction, heat transfer coefficient and heating resistance were adjusted to obtain the same geometry as in the real measurements. The tool and workpiece interface interaction was assumed to follow a shear friction law usually used for bulk-forming simulations. The value of 0.5 was used for higher strain rates and of 0.4 for lower strain rates to better fit experimental geometry. The frictional force in the constant shear definition is defined by

$$fs = m_s\, k$$

Eq. 41

where fs is the frictional stress, k is the shear yield stress and m_s is the friction factor. The Eq. 41 shows that the friction is a function of the yield stress of the deforming material [162]. The heat transfer coefficient was adjusted to obtain the measured temperature gradient. A heat transfer coefficient of 0.4W/mm²°C was found to describe well the experimental simulation. Other boundary conditions defined are heat exchange with the environment and heating of the material, defined by voltage and current flux. The material data were limited to temperatures lower than 1200°C. For simulations above 1200°C, the data were extrapolated linearly based on the last two data points [162].

2. *Simulation:* The generated database is used as input for the simulation step.

3. *Postprocessing:* In this last step the results of the problem are processed and displayed in graphs, images or videos. Stress, strain, force, strain rate, damage and temperature values for every element can be graphed and analysed.
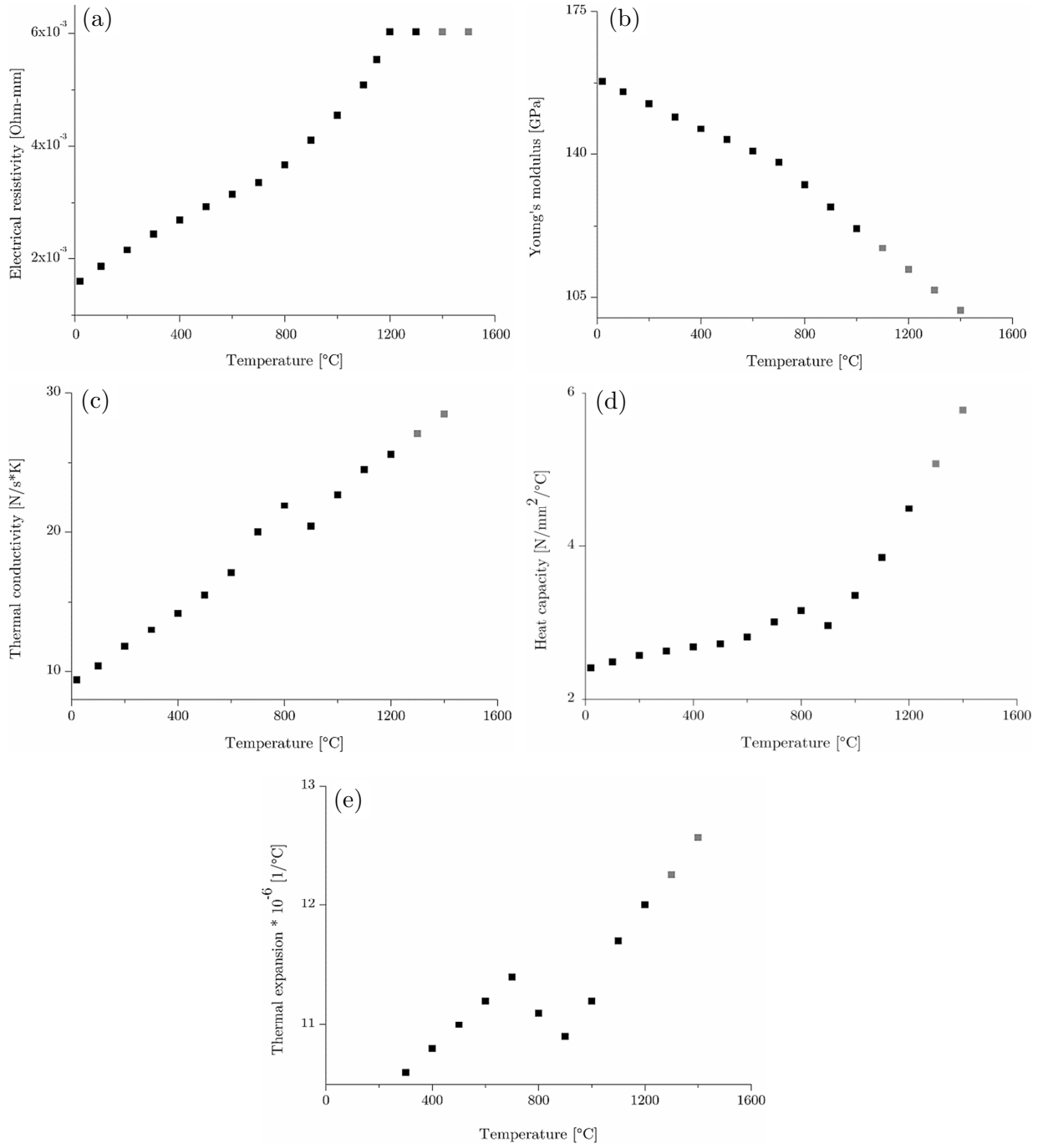
Figure 23: Material input data for FEM simulation: (a) electrical resistivity, (b) Young's modulus, (c) thermal conductivity, (d) heat capacity and (e) thermal expansion [163]. Extrapolated data are shown as grey squares.

3.5.2 User defined FEM subroutines

The flow localisation parameter and the flow stress function were implemented into the FE code DEFORM™ 2D as user subroutines. The programming language FORTRAN was used to write the user subroutines that were subsequently compiled by Absoft. In this work two different user subroutines were used: the USRMTR to calculate the flow stress using the TANH model, and USRUPD to calculate the nodal and the element values of α_{SJ}, γ' and m.

4 Results

4.1 Microstructure

4.1.1 Characterisation of the as-received material

Figures 24 (a) and (b) show SEM micrographs of the as-received condition taken using backscatter diffraction mode. The microstructure is characterised by a duplex structure consisting of globular γ grains, β_o phase and α_2/γ colonies. The colonies consist of alternating α_2 and γ laths surrounded by β_o phase (bright in the SEM micrographs). A very small amount of β_o phase was detected within the lamellae. The γ phase has the darkest colour and the α_2 phase is light grey. The α_2/γ colonies are distributed homogeneously within the specimen without any preferential direction. No microstructural differences between the edge and the centre of the specimens were observed. The phase fraction of the β_o phase was 15vol.-%, of α_2/γ colonies is 27.15vol.-% and of γ_g phase is 57.85vol.-%. The LOM images in Figures 24 (c) and (d) show precipitated TiB in black (marked by rectangles).
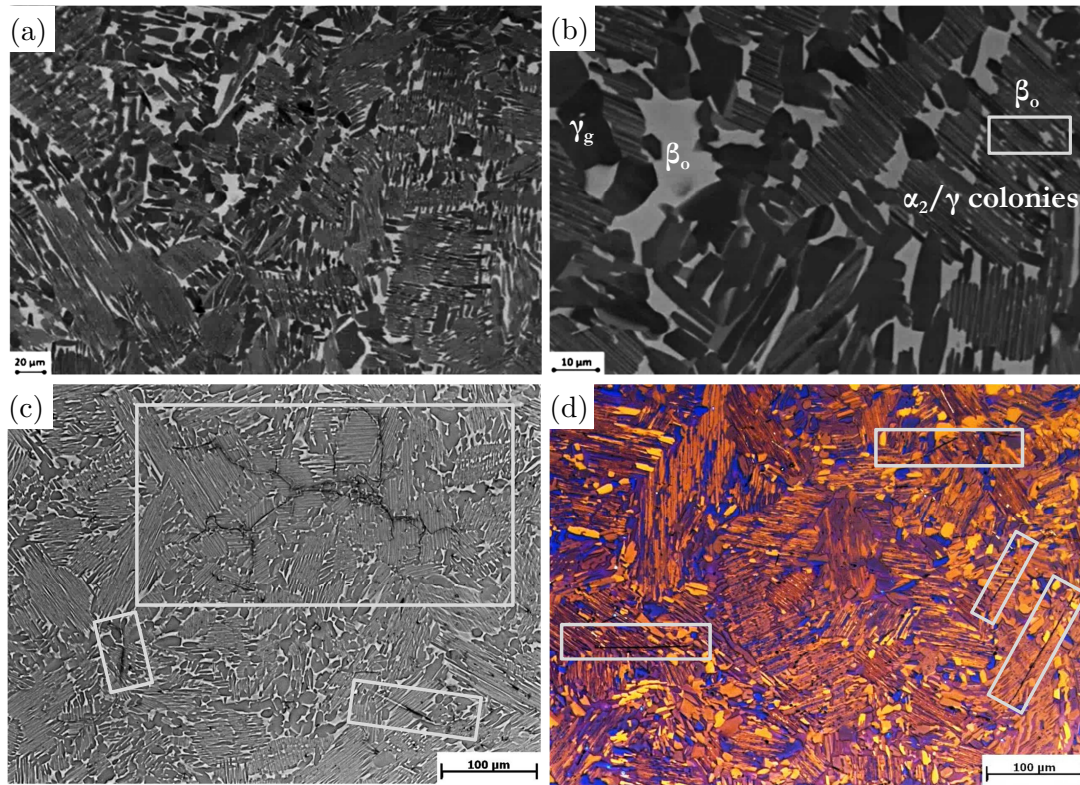

Figure 24: SEM micrographs in BSE mode of the as-received condition, i.e. α_2 light grey, γ dark grey and β_o phase bright (a), (b) LOM micrographs with TiB precipitates (marked with rectangles) etched (c) with OPS+H_2O_2 and (d) after Ence and Margolin colour etchant.

4.1.2 Microstructures after fast cycle treatments

Figure 25 shows LOM micrographs after the *fast cycle* heat treatment. Figures 25 show the microstructure of specimens heat treated at (a) 1220°C and (b) 1300°C for a soaking time of 10s. Both microstructures show TiB precipitates, which appear dark in the micrographs.
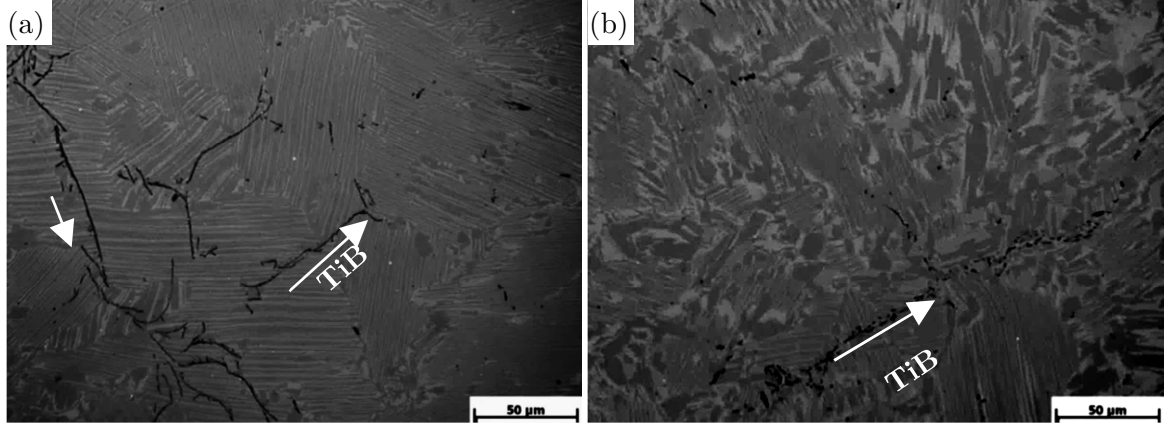

Figure 25: LOM micrographs showing TiB precipitates in the heat treated specimens after (a) 1220°C and (b) 1300°C for a soaking time of 10s.

The longitudinal temperature gradient along the specimen causes a difference in the microstructure. The temperature gradient varies depending on the temperature and the holding time.

Figure 26 shows an example for the specimen heat treated at 1220°C and soaked for 60s. In contrast to the edge Figure 26 (a), the centre (b) exhibits higher colonies content within a high amount of β_o. The α_2/γ colony size in the microstructure at the edge is larger compared to the centre. The measured temperature gradient for this testing condition is 11°C.
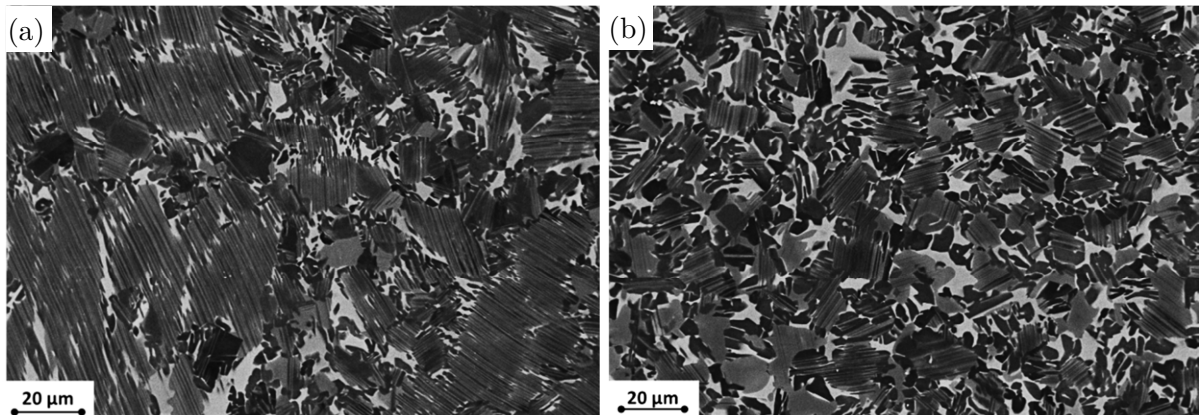

Figure 26: Microstructures of (a) the edge and (b) the centre of the specimen heat treated at 1220°C, soaking time of 60s.

Figures 27 (a)-(d) provide the SEM micrographs of the heat treated specimens at 1140°C. The microstructure consists of α_2/γ colonies with small amounts of β_o and γ_g phases.
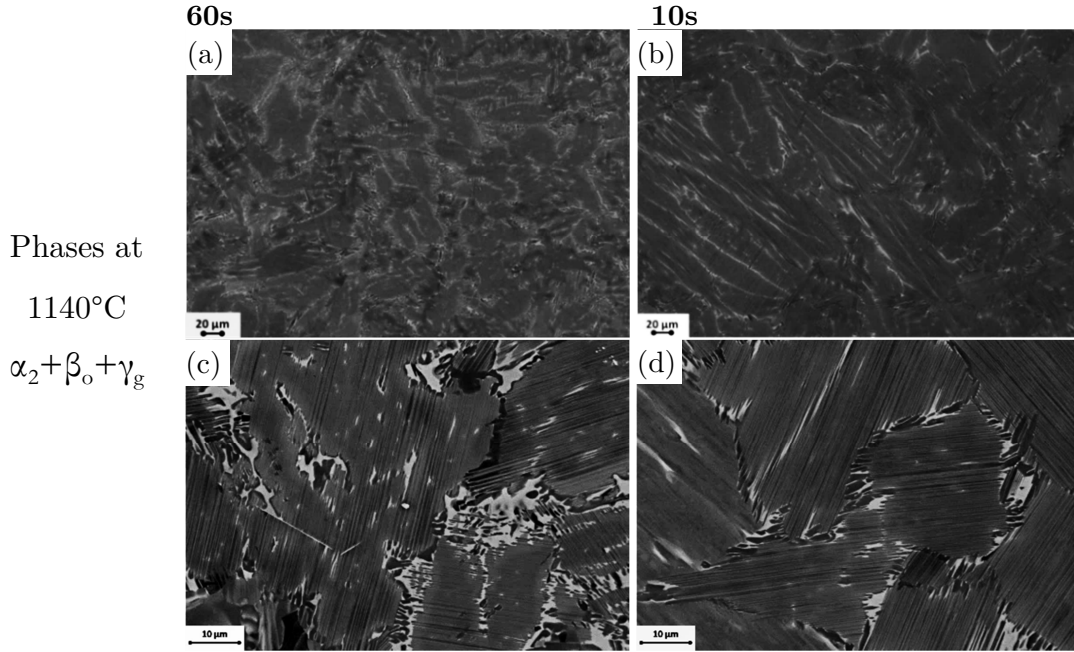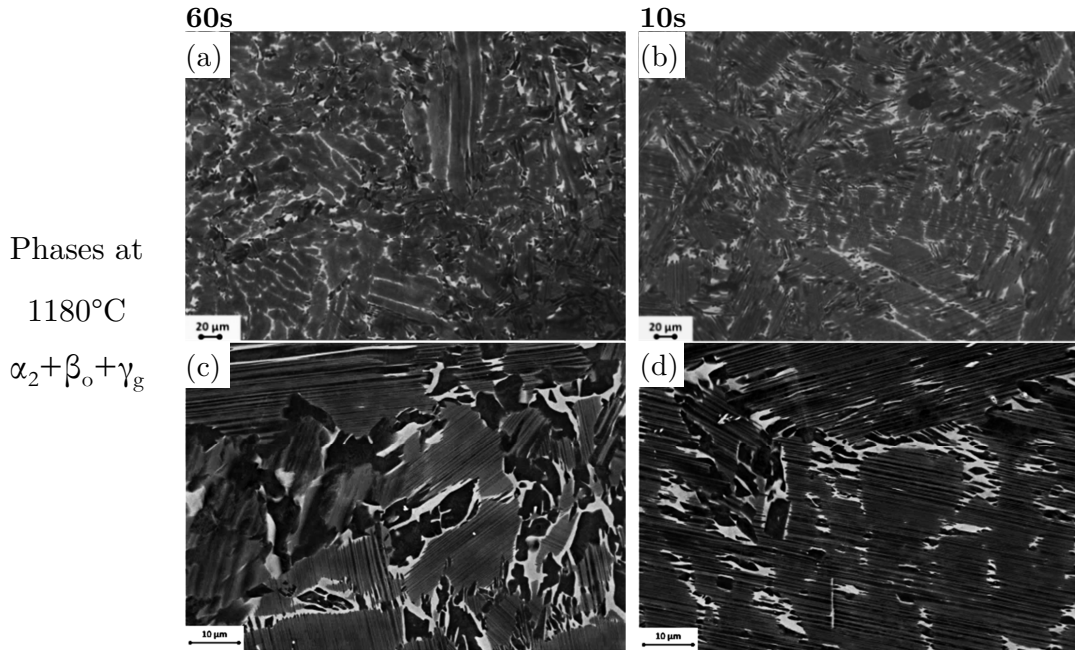
Figure 27: SEM micrographs in BSE mode of the heat treated specimens left column with a holding time of 60s/1140°C (a), (c) and 10s/1140°C (b), (d) [157,162].

The microstructure of the specimens heat treated at 1180°C was coarser than at 1220°C. The micrographs in Figures 28 (a) and (b) depict a higher amount of the γ_g phase and less phase fraction of the β_o phase.

Figure 28: SEM micrographs in BSE mode of the heat treated specimens left column with a holding time of 60s/1180°C (a), (c) and 10s/1180°C (b), (d) [157,162].

After heat treatment at 1220°C the samples showed a finer microstructure compared to those treated at higher temperatures. The images in Figures 29 revealed higher amounts of β_o and γ_g phases. The size of lamellae colonies was smaller compared to that of the samples treated at higher temperatures.
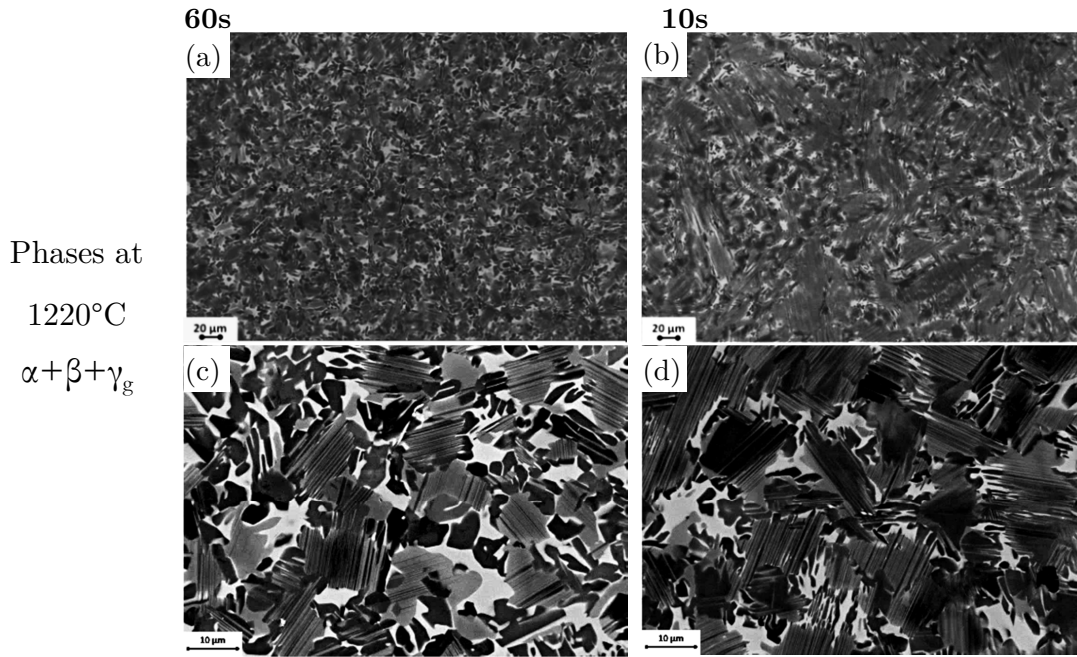
Figure 29: SEM micrographs in BSE mode of the heat treated specimens left column with a holding time of 60s/1220°C (a), (c) and 10s/1220°C (b), (d) [157,162].

The microstructure of specimen heat treated at 1260°C (see Figures 30), reveals a finer structure compared to the higher temperatures, a smaller volume fraction of the β_o phase, and presence of γ_g phase. The temperature of 1260°C corresponds to the temperature, where the γ_g phase dissolves. In comparison to the heat treated specimens at 1220°C size of the lamellae colonies is larger after heat treatments at 1260°C.
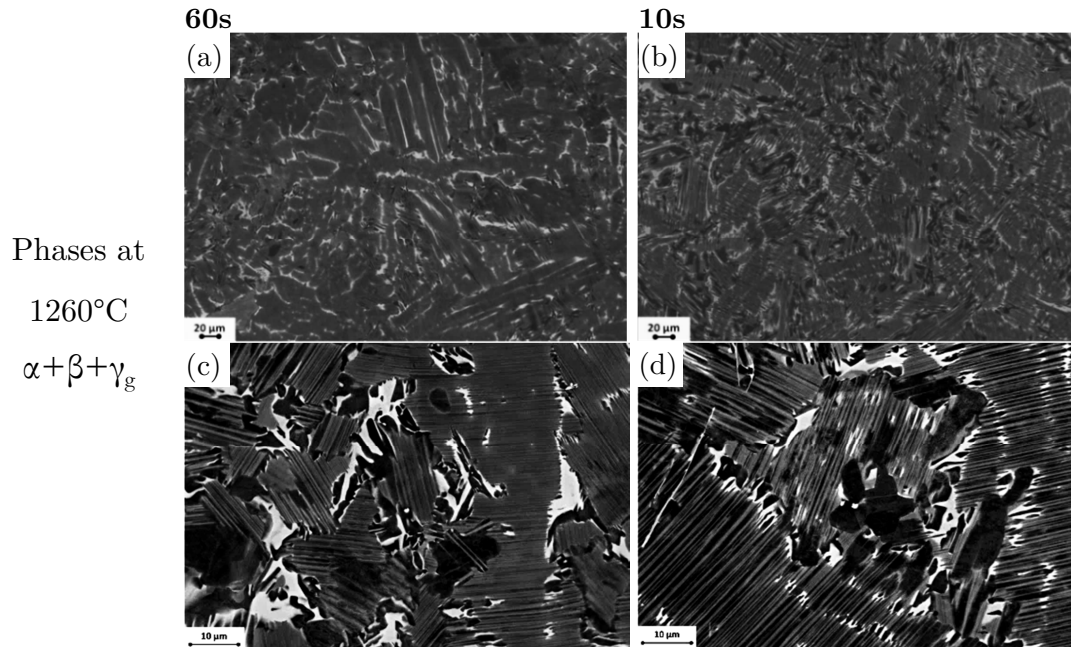

Figure 30: SEM micrographs in BSE mode of the heat treated specimens left column with a holding time of 60s/1260°C (a), (c) and 10s/1260°C (b), (d) [157,162].

Figures 31 (a)-(h) show the micrographs of the specimens heat treated at 1300°C and 1340°C with holding times of 10s and 60s. The microstructures consist of α_2/γ colonies surrounded by β_o phase. No significant differences were observed in the microstructures after the heat treatments in the $\alpha+\beta$ range.
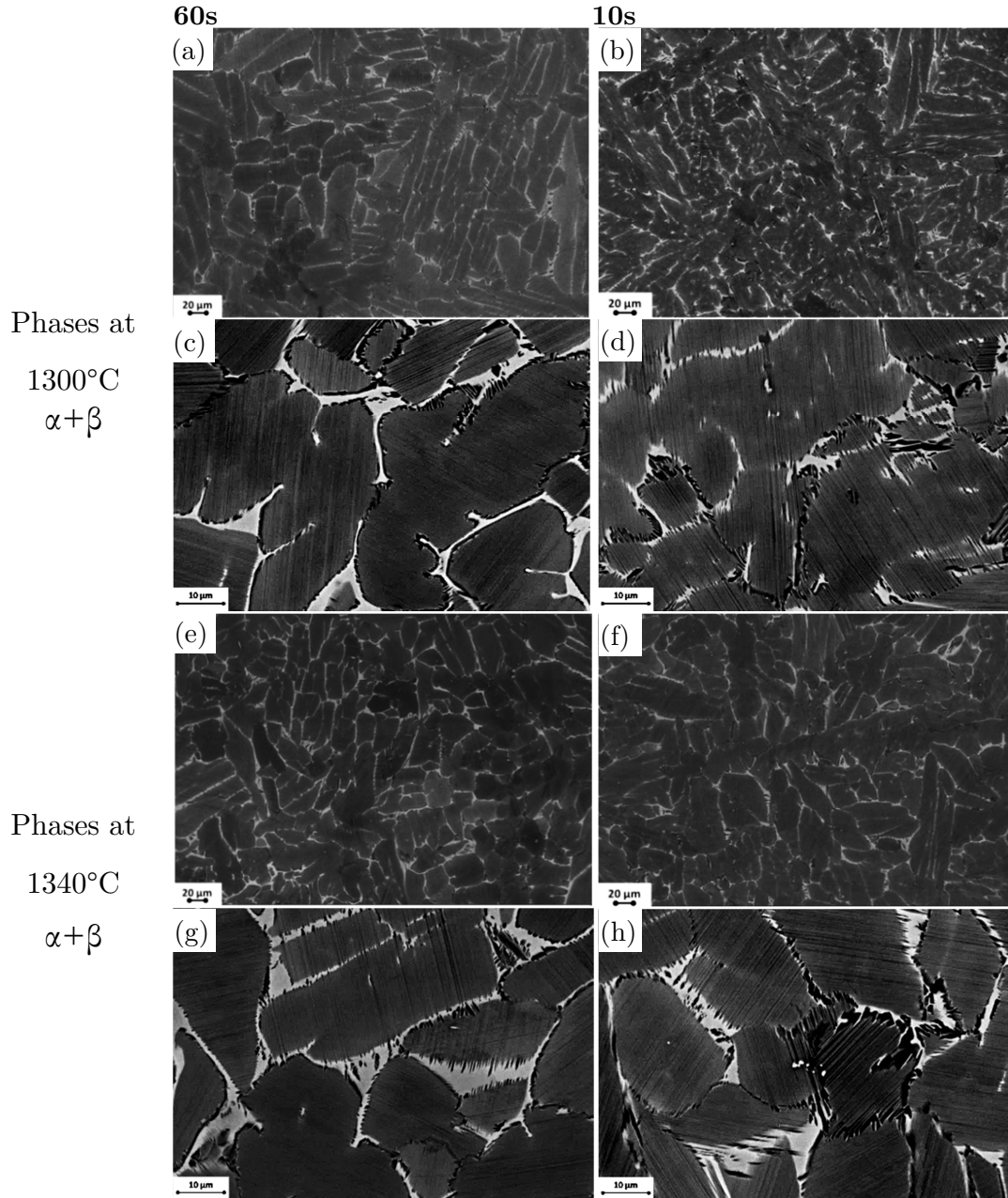

Figure 31: : SEM micrographs in BSE mode of the heat treated specimens left column with a holding time of 60s/1300°C (a), (c), 10s/1300°C (b), (d), 60s/1340°C (e), (g) and 10s/1340°C (f) and (h)[157,162].

4.1.2.1 Phase quantification of heat treated specimens

Figure 32 shows the phase fractions in area % as function of the annealing temperature during 60s, as well as the phase transformation temperatures. Figure 32 (a) shows the phase fractions obtained at the centres and (b) at the edges of the heat treated specimens, with a similar tendency. The lowest amount of β was obtained at the γ solvus temperature (1260°C). At temperatures above and below T_γ at 1220°C an increment in the β amount was observed. Below the T_{eu} (1160°C) the $β/β_o$ phase amount decreased again. The highest amount of the $α_2/γ$ colonies were obtained above the T_γ. The phase fractions differences between edge and centre were due to the temperature gradients along the specimens.
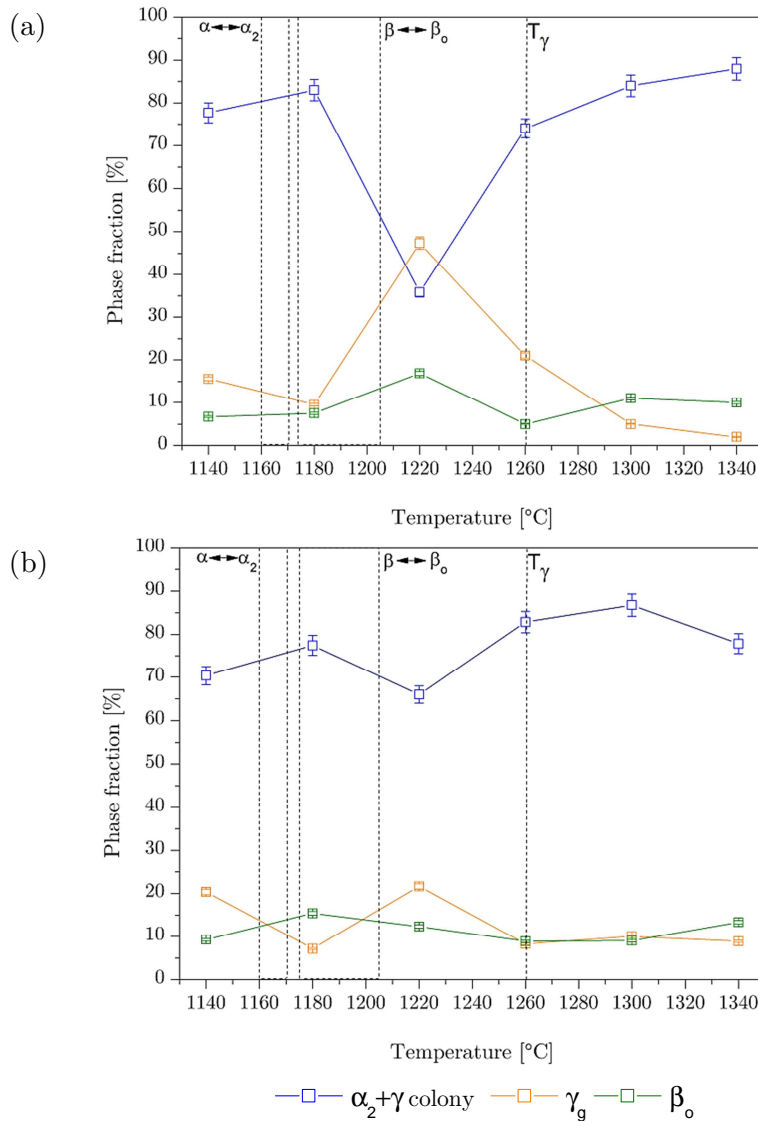

Figure 32: Quantative phase fraction analysis of (a) the centre and (b) the edge of heat treated specimens (*fast cycle*) [157].

4.1.3 Flow curves experimental

4.1.3.1 Fast cycle

Figure 33 depicts the flow curves of the TNM alloy for different temperatures and strain rates up to a strain of 0.6. Only the samples held for 60s at the testing temperature are shown. Large stress values are obtained by increasing the strain rate and decreasing the temperature and a maximal peak stress is followed by softening and then by steady flow stress. There are some exceptions at temperatures of 1220°C and 1260°C and at a strain rate of $1s^{-1}$, which show hardening after some strain.
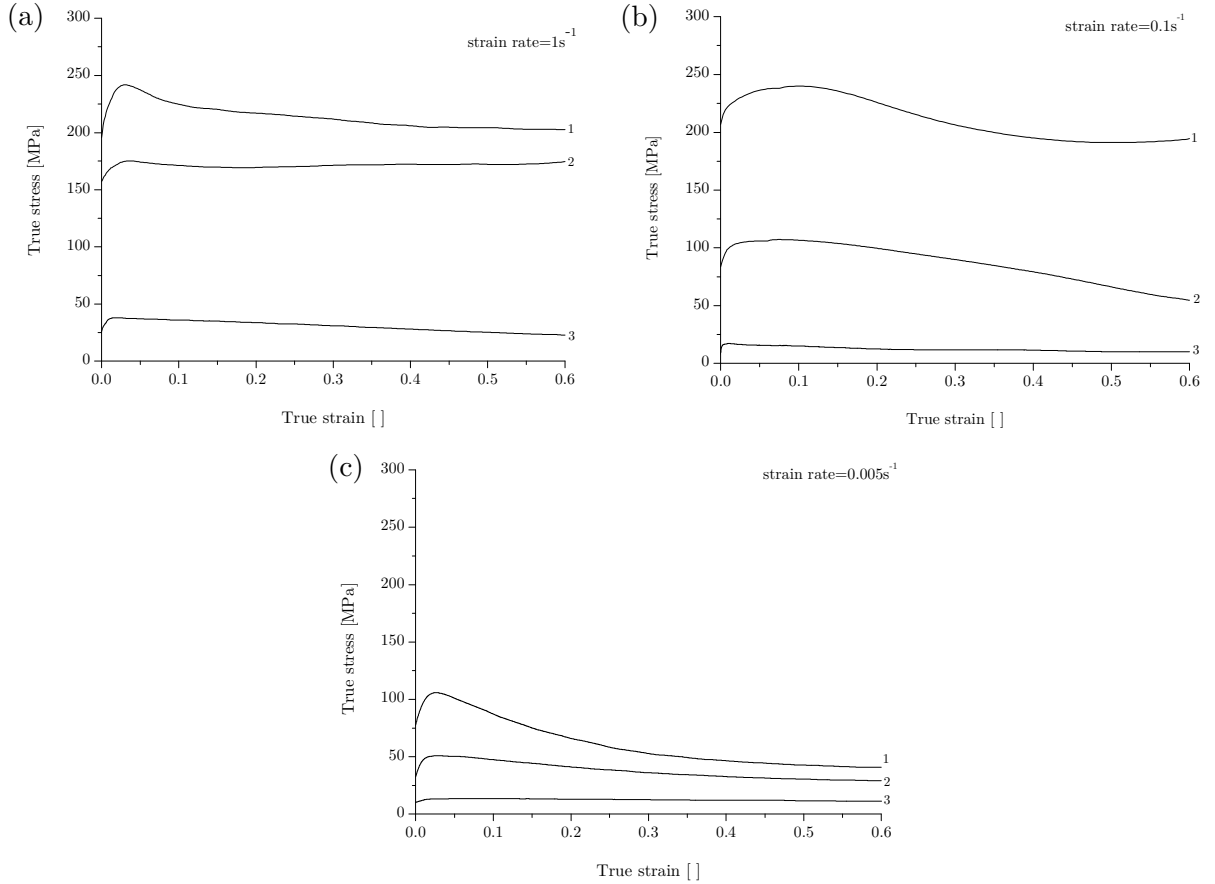

Figure 33: Flow curves of the nominal TNM alloy (*fast cycle*) at several strain rates (a) $1s^{-1}$, (b) $0.1s^{-1}$, (c) $0.005s^{-1}$ and temperatures 1: 1140°C, 2: 1220°C, 3: 1340°C.

Figure 34 (a) shows the peak stress as a function of temperature for different strain rates. A decrease in the strain rate and increase in temperature lead to lower values of the peak tresses. Figure 34 (b) shows the $\sigma_{peak} - \sigma_{0.6}/\sigma_{peak}$ (relative softening) values at a strain of 0.6 as a function of T and $\dot{\epsilon}$. The light green arrows mark the areas of large softening and the dashed areas represent hardening. Low strain rates and low temperatures show the tendency of large softening, also observed at high temperatures and high to moderate strain rates. Hardening was observed at moderate strain rates at a deformation temperature of 1220°C.
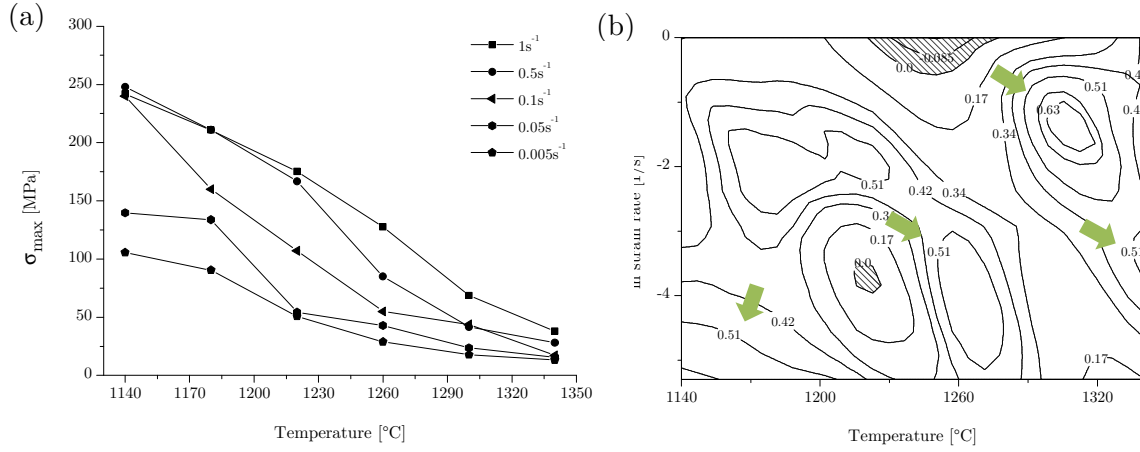
Figure 34: (a) Maximal peak stresses as function of temperature for different strain rates at a strain of 0.6 and (b) relative softening as a function of T and $\dot{\varepsilon}$ of samples deformed under the *fast cycle*.

4.1.3.2 *Slow cycle*

Figure 35 shows the flow curves corresponding to the *slow cycle* corrected by self-heating as mentioned in (3.3.3). The compression flow curves are depicted as a function of T and $\dot{\varepsilon}$. In all obtained flow curves the maximal peak stress at a low true strain (<0.05) is followed by extensive flow softening. All flow curves reach flow steady state after some strain except: 1140°C between 0.05 and 1s^{-1}, and 1220°C at 0.5s^{-1} to 1s^{-1}. The steady state conditions are approached at lower ε when decreasing $\dot{\varepsilon}$ and increasing T.
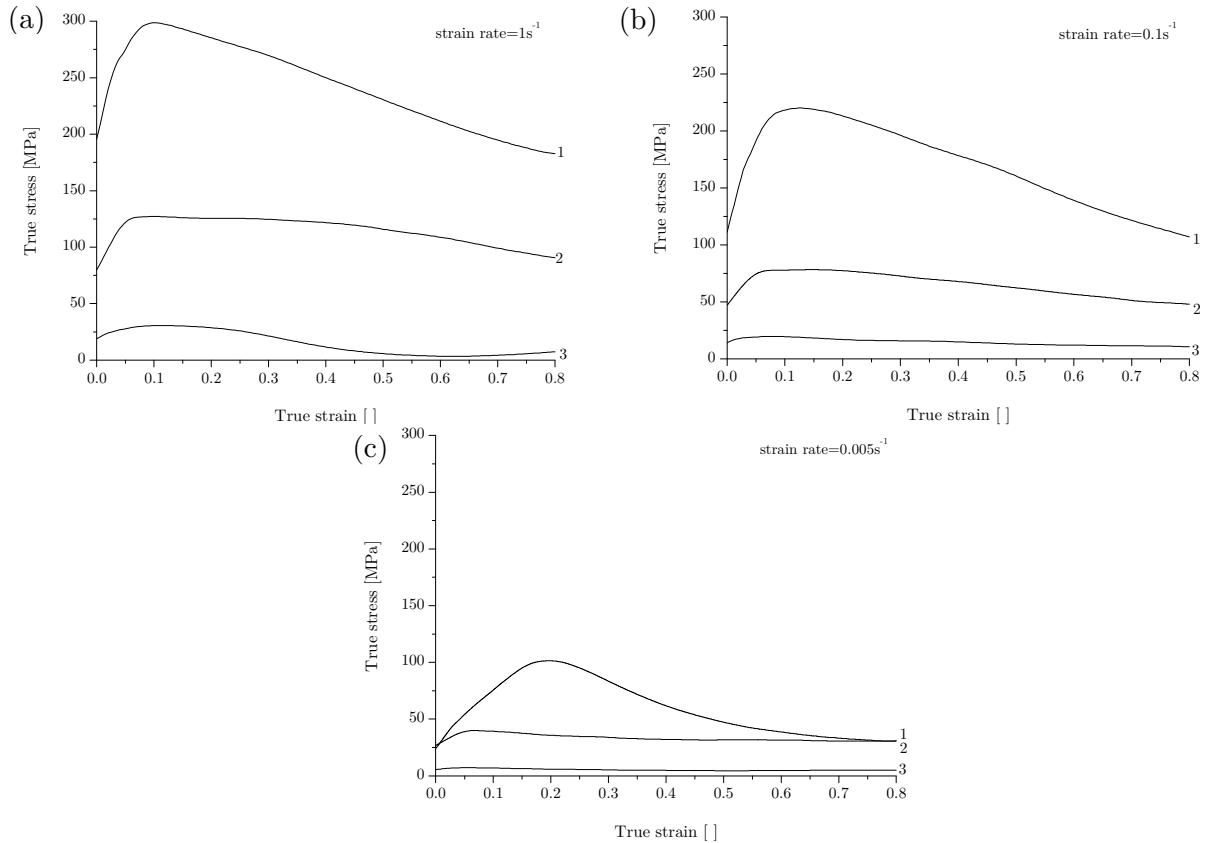

Figure 35: Flow curves of the *slow cycle* at several strain rates (a) 1s^{-1}, (b) 0.1s^{-1}, (c) 0.005s^{-1} and temperatures 1: 1140°C, 2: 1220°C and 3: 1340°C.

Figure 36 (a) depicts the peak stresses as a function of temperature at several strain rates. In general, the peak flow stress decreases with increasing temperature and decreasing strain rate. Out of the tendency the peak stresses at the temperature of 1260°C with strain rates of $1s^{-1}$ and $0.5s^{-1}$ was observed. Figure 36 (b) shows the relative softening map $\sigma_{peak} - \sigma_{0.8}/\sigma_{peak}$ for the samples deformed following the *slow cycle*. The light green arrows indicate the areas of large softening. The lowest softening values are observed for the temperatures between 1200°C and 1260°C. No negative values were calculated, which means no hardening could be observed.
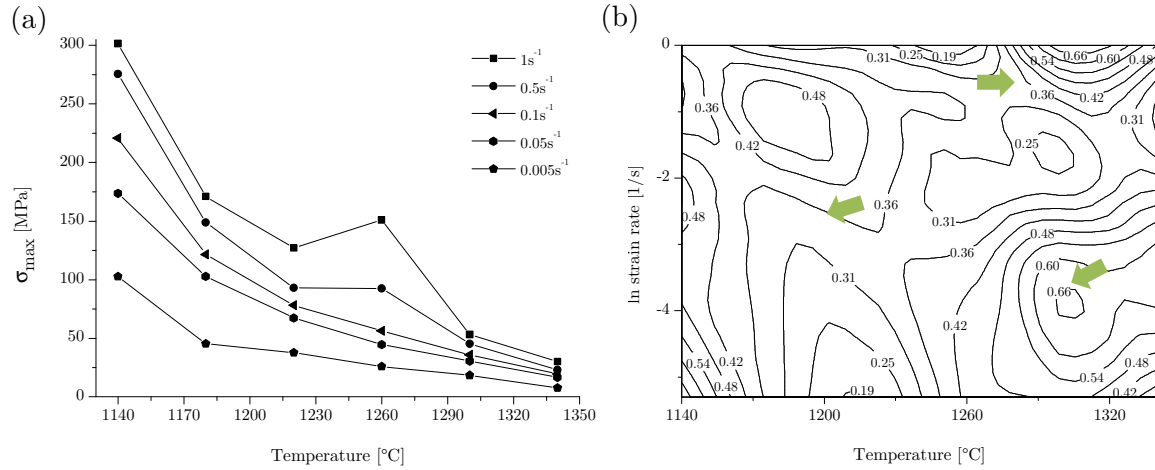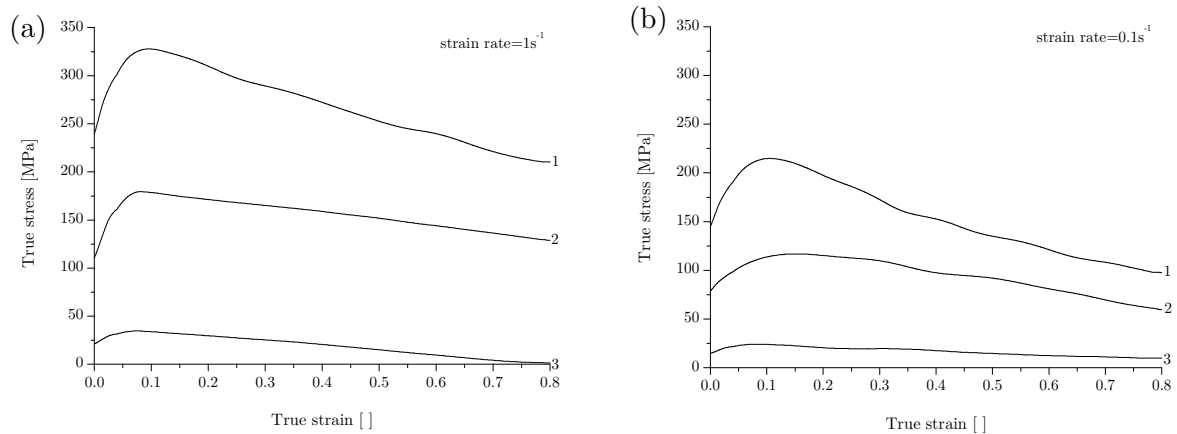

Figure 36: (a) Peak stresses as a function of temperature for several strain rates and 0.8 of strain and (b) relative softening map obtained from flow curves in Figure 35 at a strain of 0.8. Light green arrows show the large softening areas.

4.1.3.3 *Isothermal cycle*

Figures 37 show the flow curves obtained following the cycle *isothermal* at various deformation conditions. All isothermal flow curves were corrected of the self-heating effect and all of them show an increase in the flow stress up to a peak stress, followed by softening. Many flow curves achieve the steady state condition after softening. No hardening after the peak stress could be observed. With increasing temperature and decreasing strain rate it can be observed that the flow stress decreases with the exception of the flow curves at 1220°C and strain rate of $1s^{-1}$ (Figure 37 (a), 3).
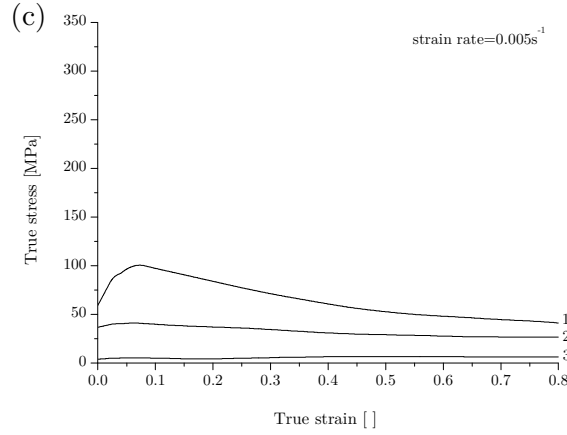
(c)

Figure 37: Flow curves of the isothermal cycle at several strain rates (a) 1s^{-1}, (b) 0.1s^{-1}, (c) 0.005s^{-1} and temperatures 1: 1140°C, 2: 1220°C and 3: 1340°C.

The peak stresses are depicted in Figure 38 (a) as a function of temperature at several strain rates at a strain of 0.8. In general, the peak flow stress is decreasing with increasing temperature and decreasing strain rate. Figure 38 (b) shows the relative softening map $\sigma_{peak} - \sigma_{0.8}/\sigma_{peak}$ for the samples deformed following the *isothermal cycle*. The light green arrows indicate the areas of large softening. The lowest softening values are observed for the temperatures between 1320°C and 1340°C.
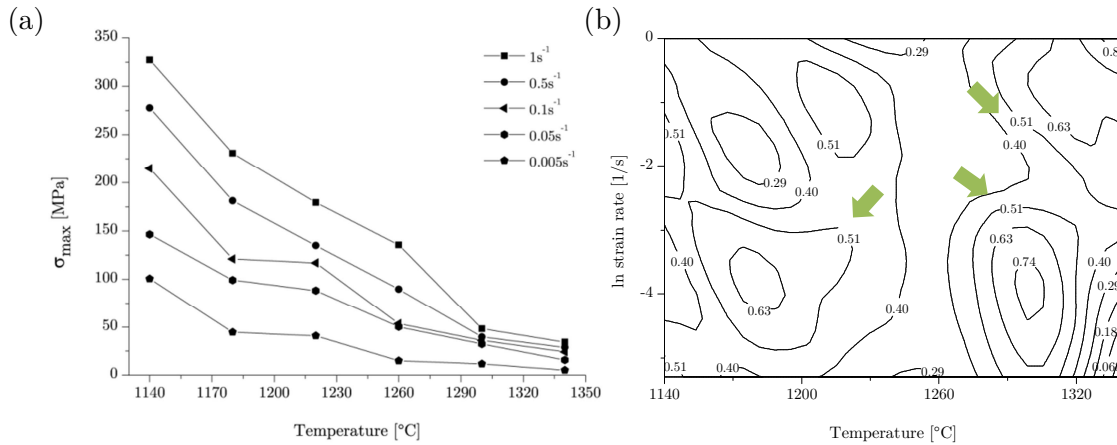
Figure 38: (a) Peak stresses as function of temperature for different strain rates at a strain of 0.8 and (b) relative softening map obtained from flow curves in Figures 37 at a strain of 0.8. Light green arrows show the high softening values.

4.1.4 Microstructures after hot deformation

4.1.4.1 *Fast cycle*

Figures 39-43 show the SEM micrographs of the specimens deformed following the *fast cycle* with a holding time of 60s. The compression direction is illustrated with an arrow with a F in it.

The specimen deformed at 1140°C and 1s^{-1} shows a duplex microstructure, which consists of α_2/γ colonies, γ_g and β_o phase surrounding the α_2/γ colonies (Figure 39 (a) and (b)). The γ_g has a smaller grain size in comparison to the heat treated condition (Figures 27 (a)-(d)).
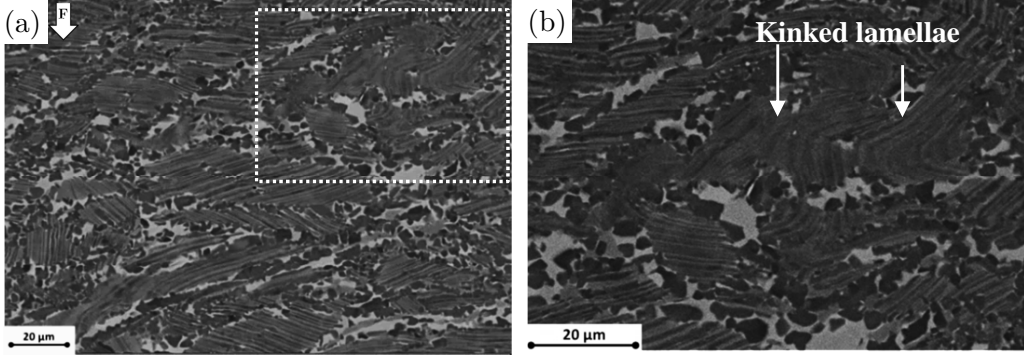
Figure 39: SEM pictures of the *fast cycle* deformation (a) and (b) 1140°C, 1 s^{-1}.

The micrographs of samples after deformation at 1140°C and 0.005s^{-1} show larger γ_g grains compared to the γ_g obtained after deformation at higher strain rates. The microstructure reveals kinking of the α_2/γ lamellae for both strain rates, as indicated by the rectangle in Figure 40 (a). The kinked colonies after deformation at both strain rates are zoomed in Figure 40 (b) and marked by arrows.

Figure 40: SEM pictures of the *fast cycle* deformation (a) and (b) 1140°C, 0.005s^{-1}.

The microstructure obtained after deformation at 1220°C and a strain rate of 1s^{-1} has a duplex microstructure, as shown in Figures 41 (a) and (b). The γ_g grains are smaller in comparison to the samples deformed at lower temperatures.
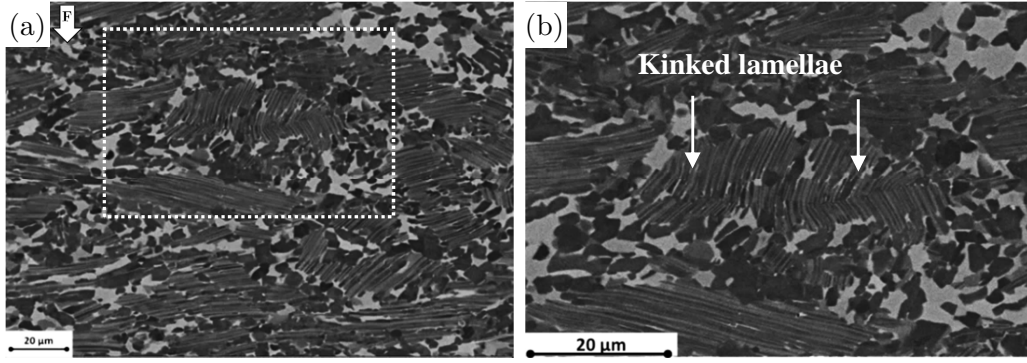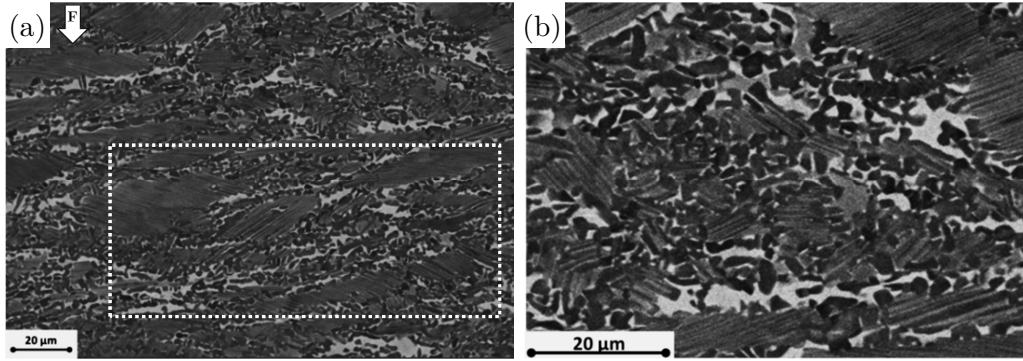

Figure 41: SEM pictures of the *fast cycle* deformation (a) and (b) 1220°C, 1 s^{-1}.

The specimen deformed at 1220°C of 0.005s^{-1} shows a different microstructure compared to the highest tested strain rate. The amount of the γ_g phase is lower than in Figure 41 (a). It can be seen that the microstructure consists mainly of α_2/γ colonies with a low amount of the β_o phase (see Figure 42 (b)).
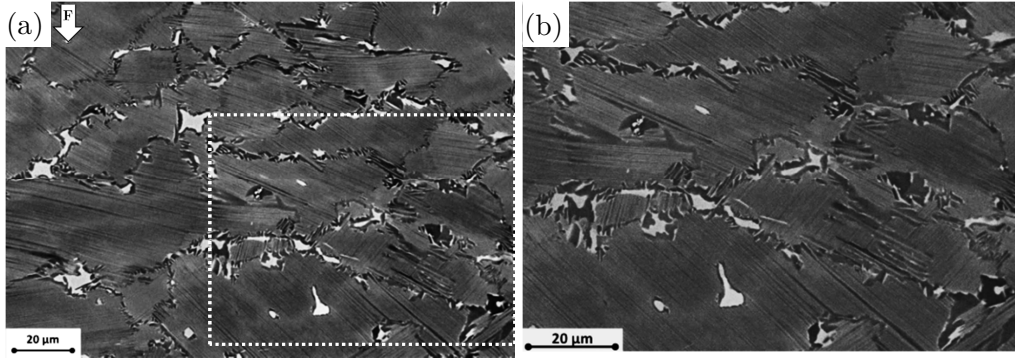
Figure 42: SEM pictures of the *fast cycle* deformation (a) and (b) 1220°C, 0.005s^{-1}.

Figures 43 (a) and (b) represent the microstructure of the specimen deformed at 1300°C with a strain rate of 1s^{-1}. It consists mainly of α_2/γ lamellae with the ordered β_o phase and small amounts of γ_g phase. The images of the specimens deformed at 1300°C and a strain rate of and 0.005s^{-1} show a microstructure with α_2/γ, β_o and small amounts of γ_g phases (Figures 43 (c) and (d)). At high temperatures (1300°C), no kinking of the α_2/γ lamellae was observed.
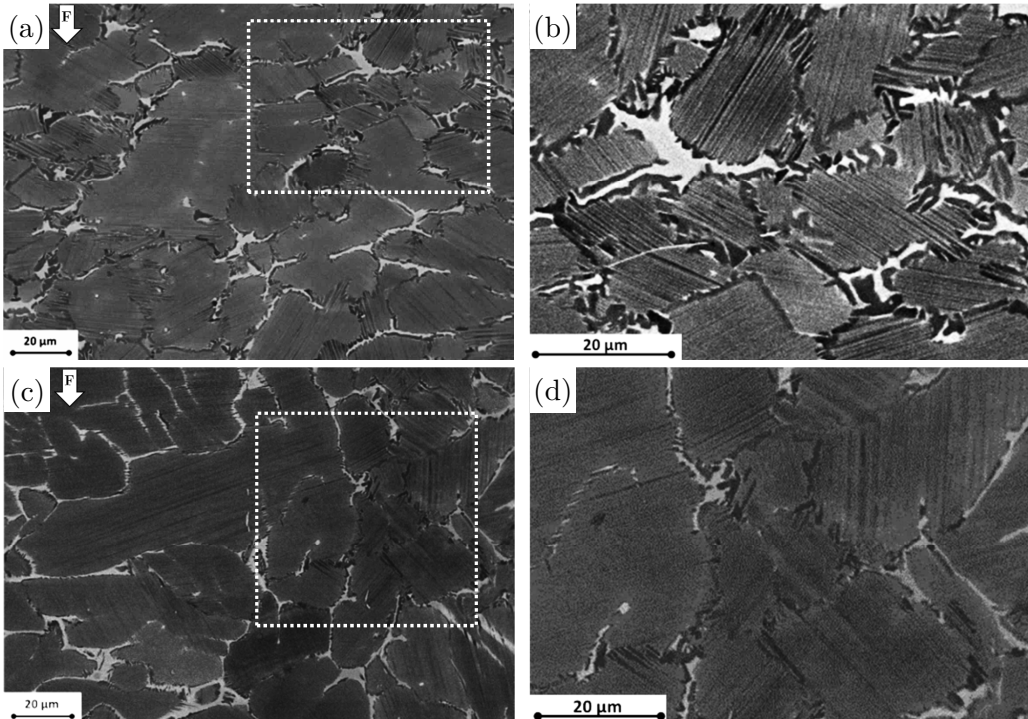
Figure 43: SEM pictures of the *fast cycle* deformation (a), (b) 1300°C, 1s^{-1} and (c), (d) 1300°C, 0.005s^{-1}.

Figure 44 shows the amounts of α_2/γ lamellae, β_o and γ_g microstructures of samples deformed after the *fast cycle* for a soaking time of 60s at the centre and the edges (b). The fractions were determined after deformation at 1140°C, 1220°C and 1300°C, strain rates 1s^{-1}, 0.05s^{-1} and 0.005s^{-1}. Generally, a higher amount of β_o is observed for the lowest temperature of 1140°C. The γ_g phase fractions are observed below 1260°C. As can be seen in both diagrams the highest α_2/γ colonies amount is observed for the temperature of 1300°C. The phase fractions of the specimens' edges slightly differ from the ones at the centre, and this difference is due to the longitudinal temperature gradient along the specimens. The obtained results correlate to the findings in Figure 4 (b) (see chapter 2.1.1).

Figure 44: Quantitative phase fractions (a) of centres and (b) edges of the deformed specimens for several temperatures and strain rates.

4.1.4.2 *Slow cycle*

Figures 45-51 depict the microstructures after hot deformation at different conditions. All micrographs were taken from the centre of the deformed specimens after deformation under the *slow cycle.*
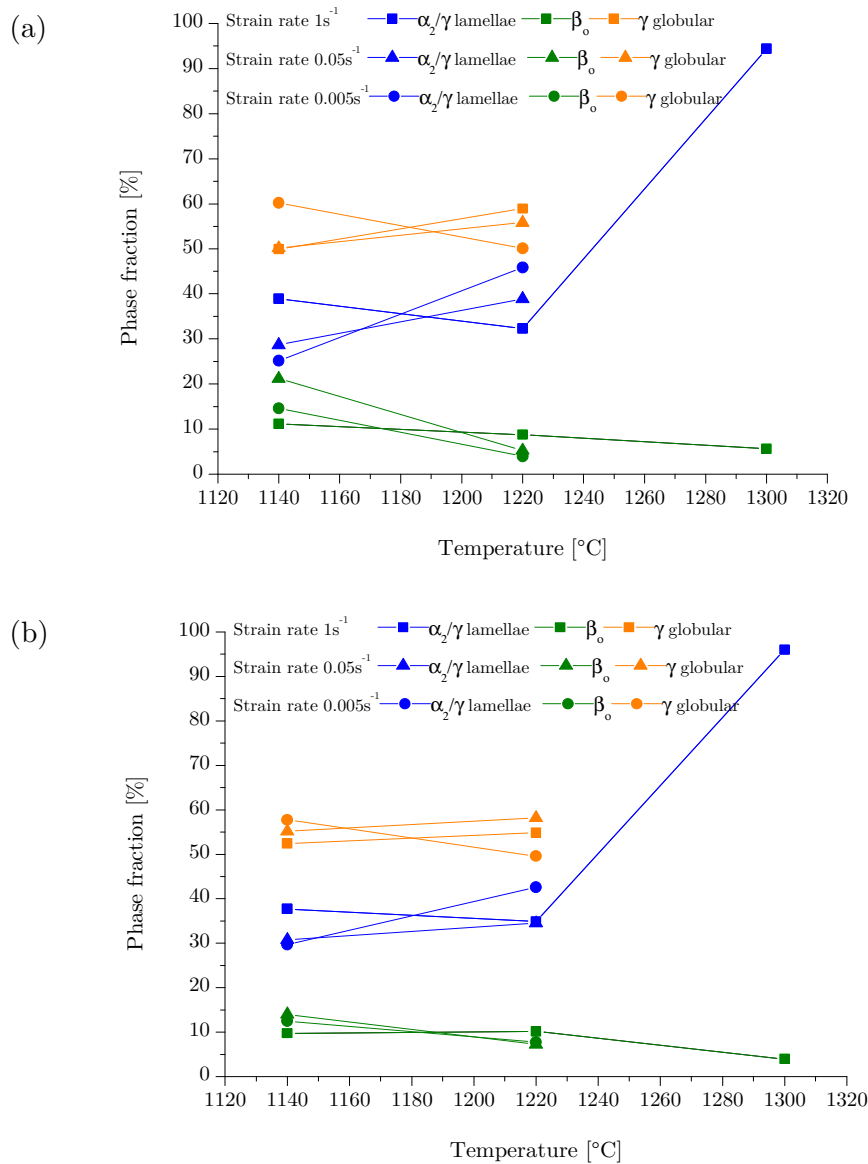
The SEM micrographs of the deformed specimen at 1140°C, $1s^{-1}$ show a microstructure consisting of α_2/γ lamellae with β_o and γ_g phases (Figures 45 (a) and (b)). In many colonies the lamellar structure appears as kinked. Lamellar globularization is observed inside some lamellar colonies. In the α_2/γ colonies in Figures 45 (c) and (d) there are areas within fine γ grains, which are marked by rectangles. Small amounts of the β_o phase appeared within the colonies (Figures 45 (e) and (f)).
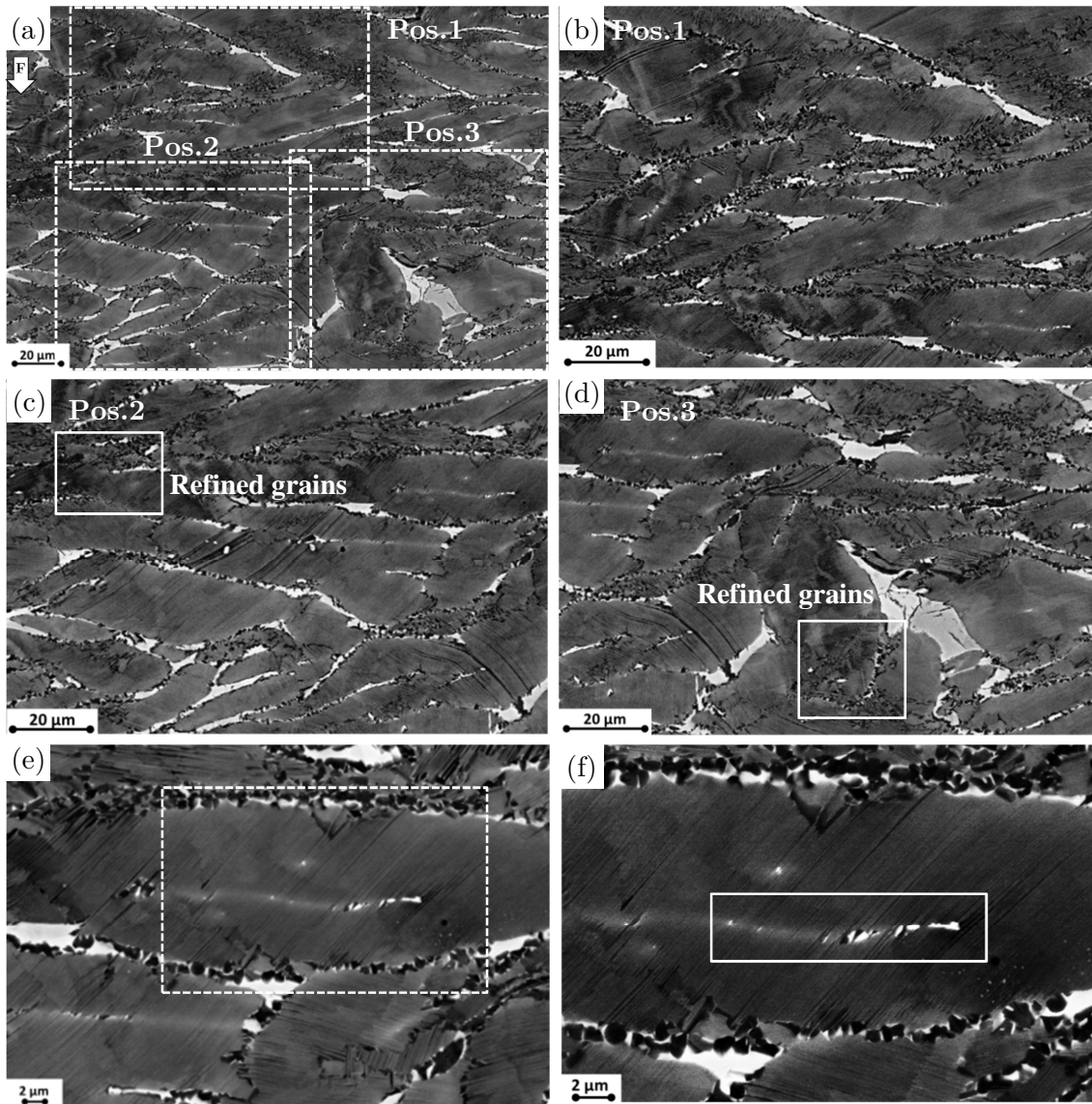
Figure 45: FEG-SEM micrographs of the deformed specimens at 1140°C and $1s^{-1}$.

The micrographs of the deformed specimen at 1140°C and $0.005s^{-1}$ show a microstructure that can be seen in Figures 46 (a)-(d). In comparison to the high strain rate, the micrograph of this specimen shows a higher β_o fraction. In comparison with the as-received state the grain size of the γ_g phase is smaller in the deformed specimens. Annealing twins in the

hexagonal γ_g phase are shown in Figures 46 (a) and (b) (marked by arrows). Many lamellae appear kinked in the colonies (Figures 46 (c) and (d)). TiB are observed along the colonies, as indicated by arrows in Figure 46 (d).
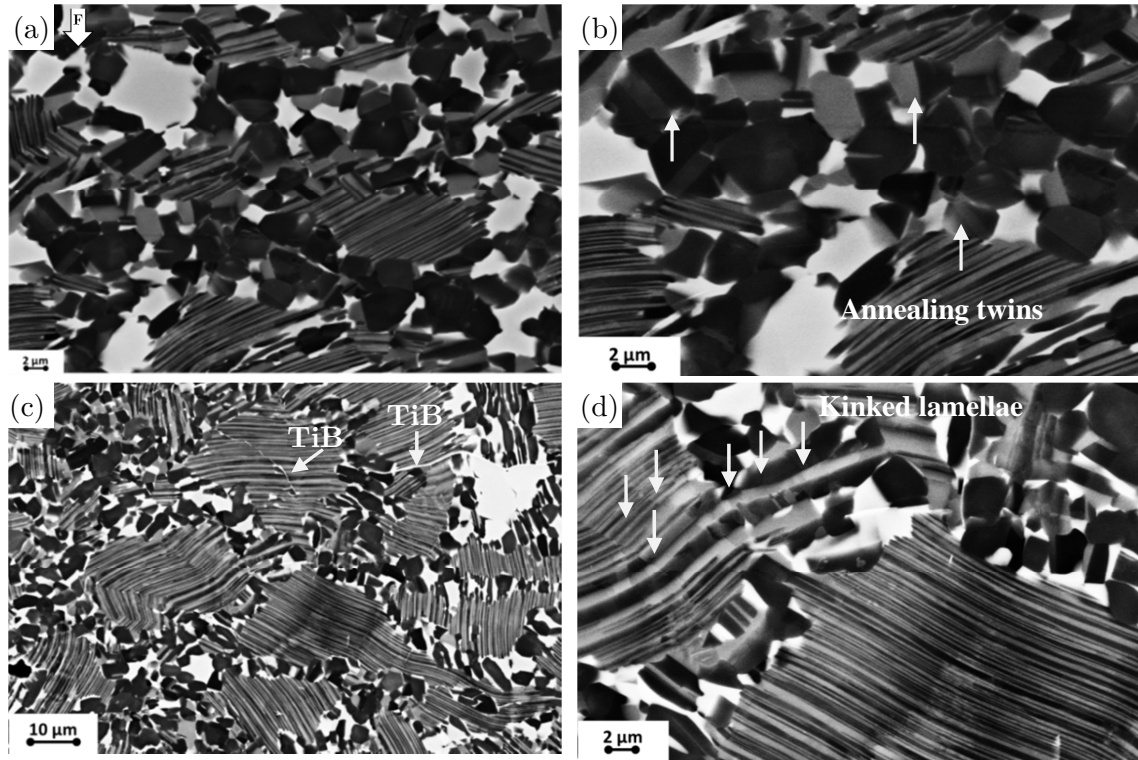
Figure 46: FEG-SEM micrographs of the deformed specimens at 1140°C and 0.005s^{-1}.

Figures 47 show the microstructure of the specimen deformed at 1220°C and 1s^{-1}. At this temperature a α_2/γ colony microstructure with β_o phase and the γ phase is detected. The γ phase that surrounds the α prior grain boundaries, is not globular as in the low temperature range. The β_o phase appears elongated at high strain rates and equiaxed at low strain rates. At a deformation at temperature of 1220°C the prior phase grain boundaries are observed and the α_2/γ colonies are formed inside them. The precipitates TiB appear bright in the micrograph, as marked in Figure 47 (b).
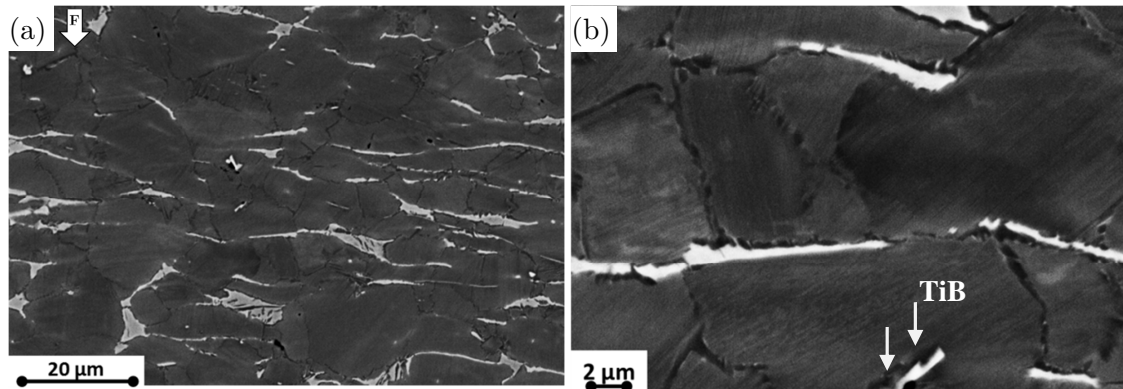
Figure 47: FEG-SEM micrographs of the deformed specimens at 1220°C and 1s^{-1}.

The image of the specimen deformed at 1220°C and a strain rate of $0.1s^{-1}$ shows a complex β_o phase, as shown in Figures 48 (a) and (b). The micro segregation of the β_o phase within the colonies is observed.
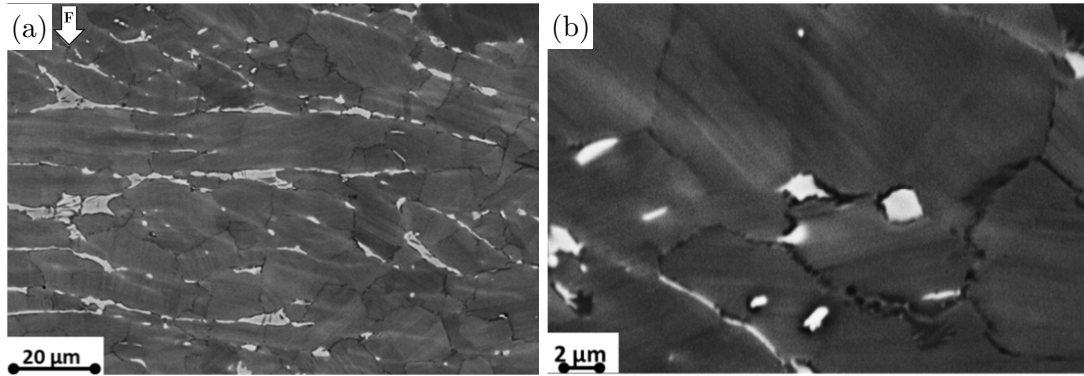
Figure 48: FEG-SEM micrographs of the deformed specimens at 1220°C and $0.1s^{-1}$.

The image in Figure 49 (a) of the specimen deformed at 1260°C and $1s^{-1}$ reveals only α_2/γ colonies surrounded with β_o phase. Some low fraction γ phase is primarily located within the β_o phase. Many segregation areas of the β_o phase within the colonies are observed (Figures 49 (b) and (c)).

Figure 49: FEG-SEM micrographs of the specimens deformed at 1260°C and $1s^{-1}$.

The prior α grains can be distinguished for the low and high strain rates (see Figure 50 (a)).
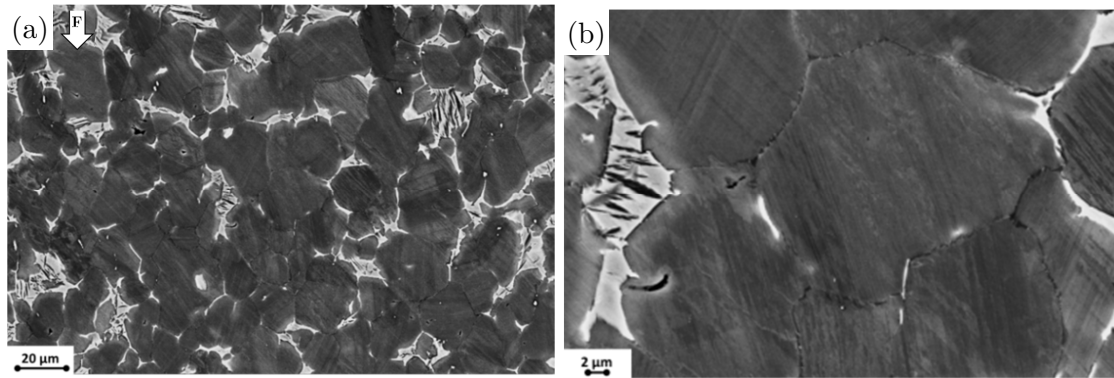
Figure 50: FEG-SEM micrographs of the specimens deformed at 1260°C and 0.005s^{-1}.

The sample deformed at 1300°C and 0.1s^{-1} shows microstructure features similar to the sample deformed at 1260°C and 0.005s^{-1}, as shown in Figures 51.
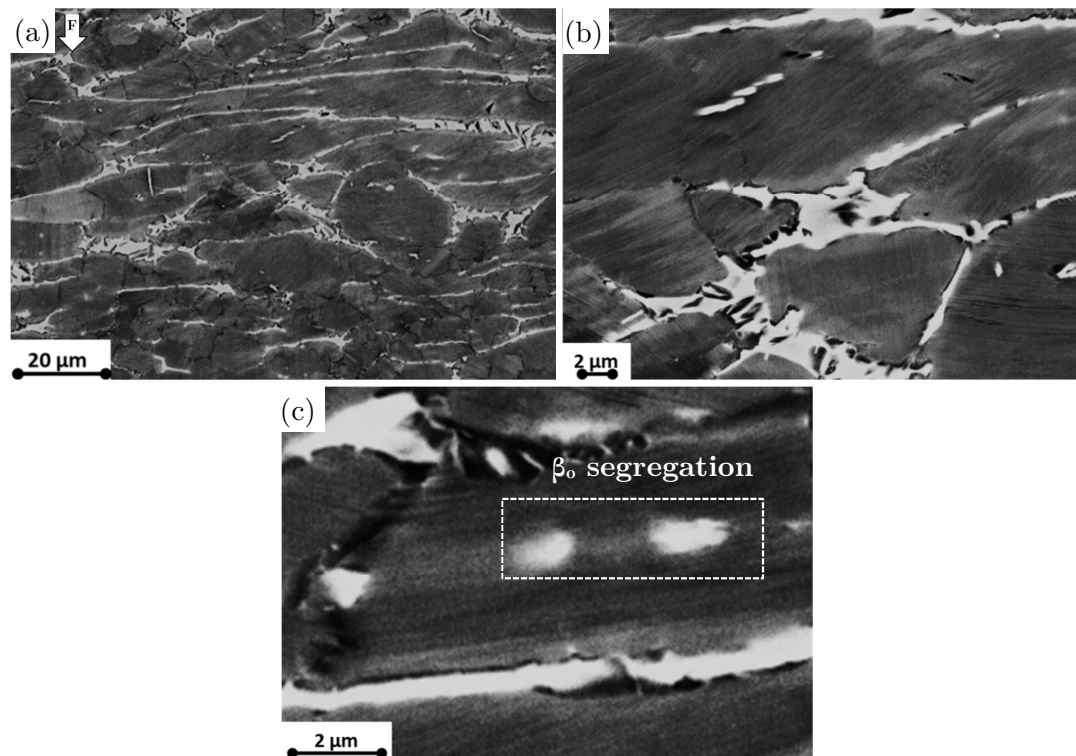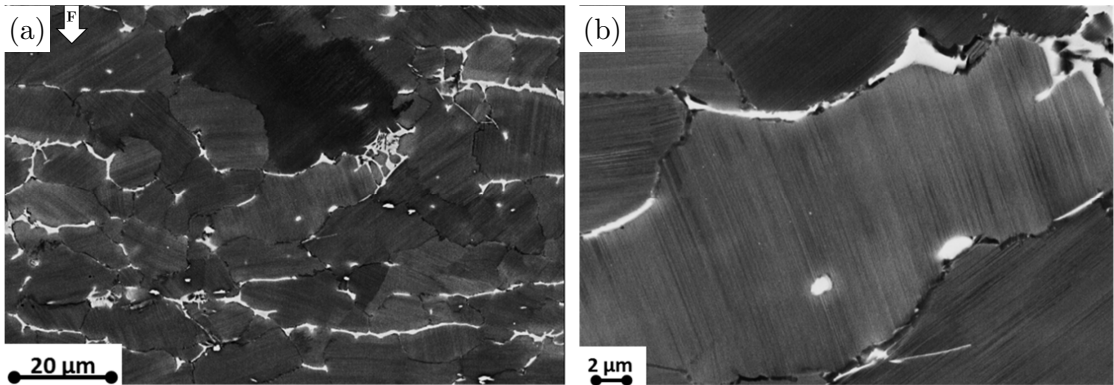

Figure 51: FEG-SEM micrographs of the specimens deformed at 1300°C and 0.1s^{-1}.

The images of the specimens deformed at 1140°C and a strain rate of 1s^{-1} are shown in Figures 52 as a function of the global strains (a)-(d) ε=0.2, (e), (f) ε=0.4, (g), (h) ε=0.6 and (i), (j) ε=0.9.

At the lowest strain of 0.2, the microstructure consists of α_2/γ colonies surrounded by the β_o phase. The α_2/γ colonies have more a rather randomly orientation with respect to the direction of compression axis. Additionally, small amounts of γ_g grains can be observed, which are primarily located at the interface between colonies and β_o grain boundaries. The beginning of α_2/γ lamellae kinking and β_o segregation is observed at the strain of 0.2 (see Figures 52 (a)-(d)). An increment in the strain to 0.4 shows a higher amount of the β_o phase within the α_2/γ colonies, as depicted in Figure 52 (e). It is visible that the γ_g phase fraction increases with increasing strain. TiB precipitates are formed within the α_2/γ colonies, as marked in Figure 52 (f). By increasing the strain the γ_g phase fraction further increases and the α_2/γ lamellae become bent (Figures 52 (g) and (h)). After deformation up to a strain of 0.9 α_2/γ lamellae appeared kinked (Figures 52 (i) and (j)).
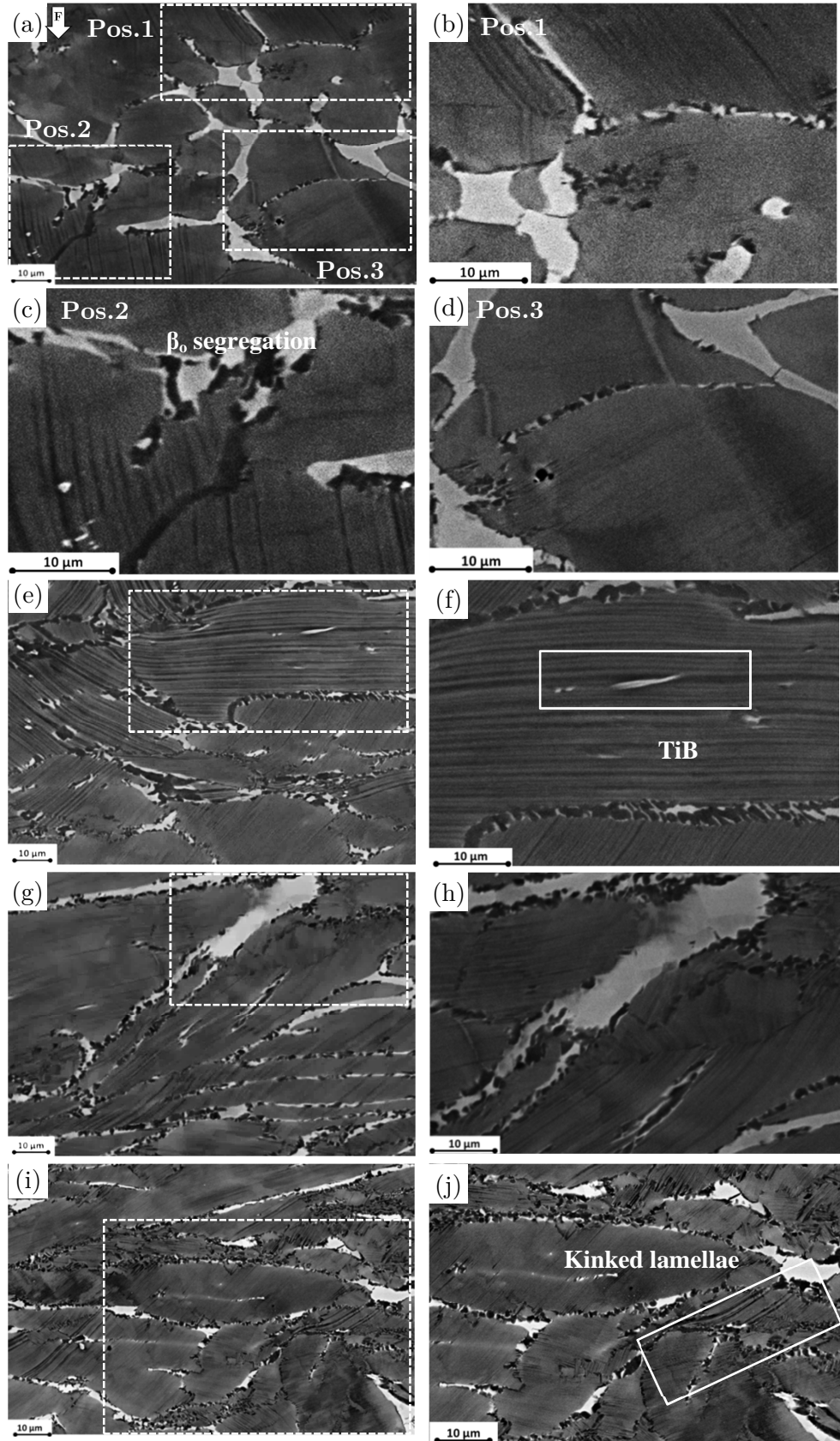
Figure 52: SEM micrographs of the deformed specimen at 1140°C with a strain rate of 1s⁻¹ up to true strains of (a)-(d) ε=0.2, (e), (f) ε=0.4, (g), (h) ε=0.6 and (i), (j) ε=0.9.

Figures 53 show the images of the specimens deformed at 1220°C and at 1s⁻¹ and 0.005s⁻¹. The micrographs were taken using backscatter and inlens detectors, revealing that fine B rich precipitates have been formed during the deformation of the *slow cycle*. The precipitates appear bright in the SEM-BSE images, as shown in Figures 53 (a) and (c). Their chemical composition was determined by EDX (Figure 53 (e)), and it consists of a high content of the elements Mo, Nb and B. Those precipitates correspond to the titanium niobium borides.
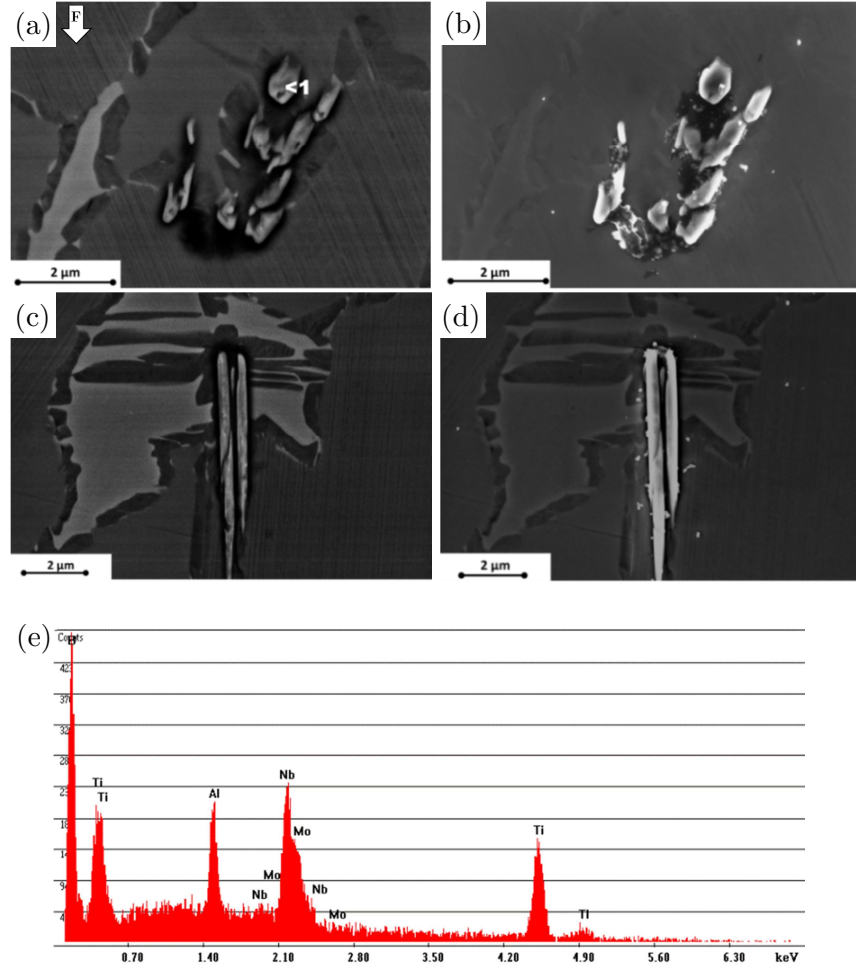
Figure 53: Micrographs of deformed specimens (a) and (b) 1220°C, 1s⁻¹, (c) and (d) 1220°C, 0.005s⁻¹ (BSE (a), (c) vs SE (b), (d) and (e) EDX analysis point in Figure 53 (a)).

4.1.4.3 X-Ray diffraction

Figure 54 shows the X-Ray diffraction analysis results of the as-received condition and two specimens deformed at 1140°C, 1s^{-1} and 1260°C, 0.005s^{-1}. In as-received condition large reflex intensities of the β_o and γ phases are observed. The specimen deformed at 1140°C reveals a significant increment of the α_2 intensity at expense of the β_o phase compared to the as-received condition. The XRD pattern of the sample deformed at 1260°C shows a large decrease in the γ phase intensities and large increase in the α_2 phase reflex intensities (see Figure 54 (d)). A broadening of the α peaks in the different conditions is observed.
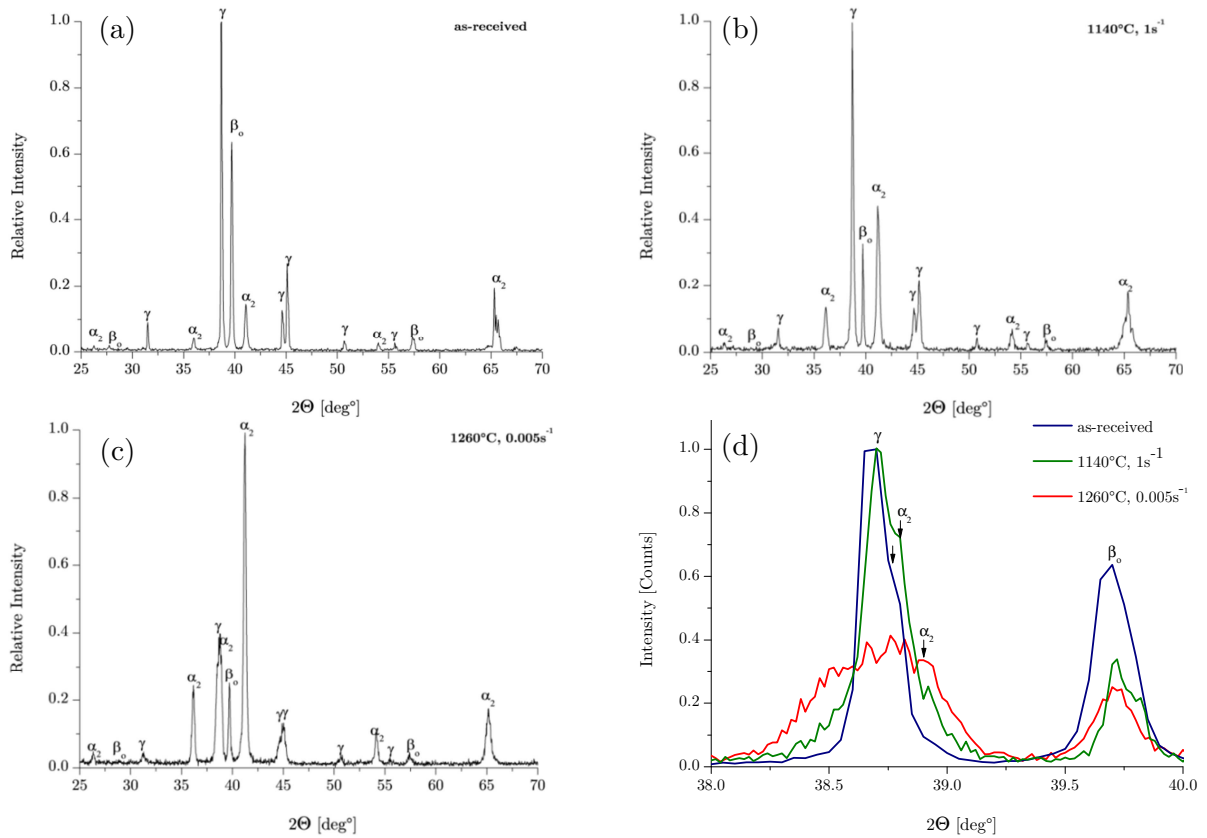
Figure 54: X-Ray diffraction patterns (Cu Kα) of the TNM alloy of the deformed specimens (a) as-received condition, (b) 1140°C, 1s^{-1}, (c) 1260°C, 0.005s^{-1} and (d) comparison.

4.1.5 Elements mapping

The elements mapping was carried out by means of EDX to reveal the correlation between phases and damage. Figure 55 shows the EDX maps for specimens deformed at a strain rate of 1s^{-1} and temperatures of (a) 1140°C and (b) 1260°C. The distributions of the elements Al, Nb and Mo are shown. The SEM micrograph in Figure 55 (a) shows α_2/γ lamellae with β_o phase and γ_g phases. A wedge crack is observed in black. Figure 55 (b) shows wedge cracks in the specimen deformed at 1260°C. The wedge crack is visible in the Nb and Mo elements indicating damage in the β_o phase, rich in Nb and Mo.
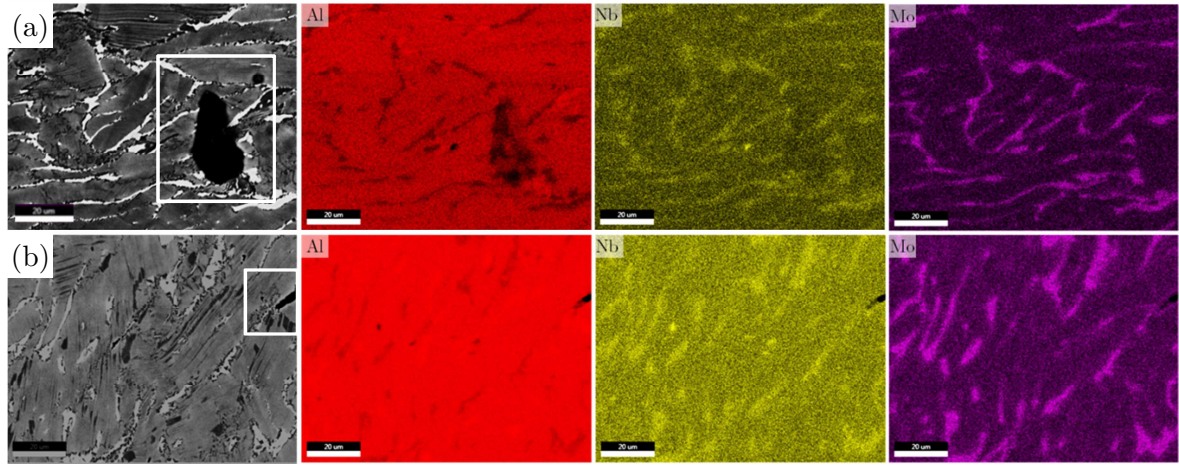
Figure 55: EDX analysis of specimens deformed at 1s^{-1} and at several temperatures. Mapping of elements Al, Nb and Mo. Deformation at temperatures of (a) 1140°C and (b) 1260°C.

4.1.6 Macrostructure after hot deformation under slow cycle schedule

The macroscopic damage evaluation was carried out via stereomicroscope analysis, and images are shown in Figure 56.

All deformed samples were barrelled because of the friction between anvils and samples. At low temperatures several macroscopic cracks were formed at the surface, as shown in Figure 56 (a)-(c). The cracks were oriented parallel to the compression axis and appeared mainly in the bulged area. Furthermore, the specimen deformed at 1140°C and a strain rate of 1s^{-1} shows a macro shear band as marked in Figure 56 (a).

Decreasing the strain rate at a given temperature as well as increasing the temperature at a given strain rate lead to less cracks at the surface (marked by rectangles).
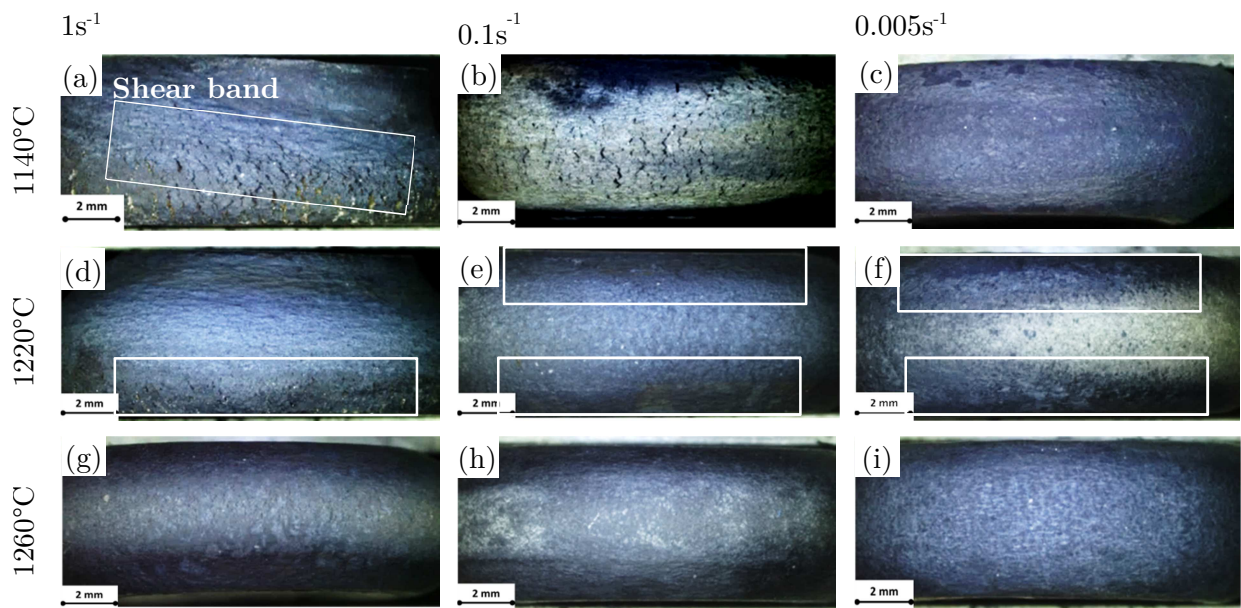
Figure 56: Macroscopic images of deformed specimens at several temperatures of 1140°C (a) 1s^{-1}, (b) 0.1s^{-1}, (c) 0.005s^{-1}, 1220°C (d) 1s^{-1}, (e) 0.1s^{-1}, (f) 0.005s^{-1} and 1260°C (g) 1s^{-1}, (h) 0.1s^{-1}, (i) 0.005s^{-1}. Compression axis is vertical.

4.1.7 Microdamage after deformation

4.1.7.1 *Fast cycle*

The microstructural damage characterised using LOM and SEM are shown in Figures 57, 58 and 59. In all images the loading direction is depicted.

Figure 57 shows the characteristics of a shear band after deformation at 1140°C, 1s^{-1} and a strain of 0.9. The direction of the formed macro shear band is indicated by the rectangle in Figure 57 (a). Figure 57 (b) depicts the microstructure inside and Figure 57 (c) outside the shear band. The microstructure in the shear band is much finer than outside. Close to the shear band the microstructure is highly deformed.
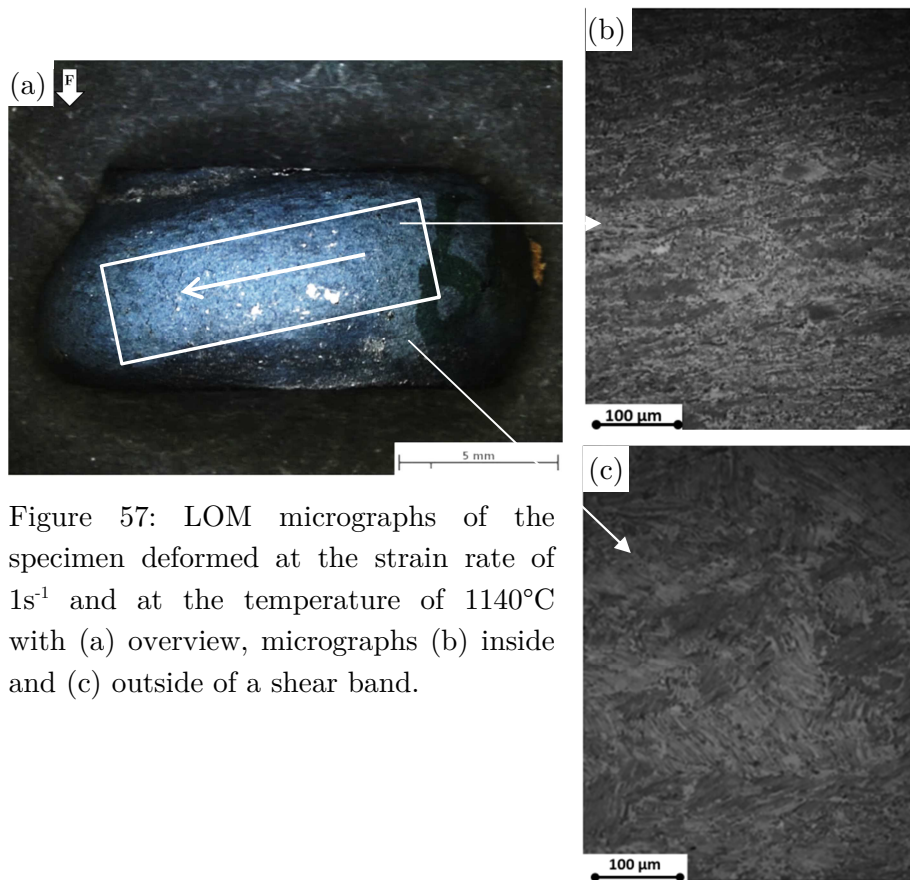
Figure 57: LOM micrographs of the specimen deformed at the strain rate of 1s^{-1} and at the temperature of 1140°C with (a) overview, micrographs (b) inside and (c) outside of a shear band.

The specimen deformed at 1140°C and a strain rate of 0.1s^{-1} shows micro cracks initiated at the bulge Figure 58 (a). The micro crack propagates parallel to the lamellae orientation (Figure 58 (b)). Some cracks appear across the lamellae and on the whole translamellar crack propagation dominates. Many small cracks (smaller than 40µm) are arrested in the lamellae colony and some propagate in the neighbouring lamellae colonies. Some small cracks form parallel to the main crack located near the tip of the latter. The bulged area shows micro crack formation due to tensile stresses state during deformation. The initial crack formation is not being analysed in this work.
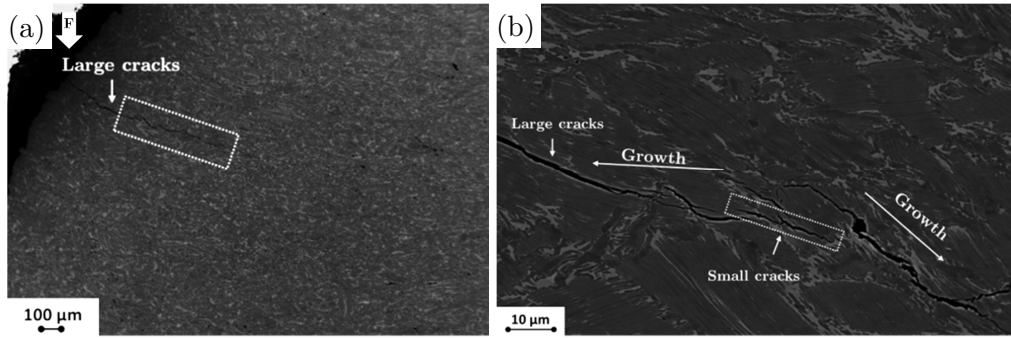
Figure 58: Micro damage analysis of the deformed specimens at 1140°C, 0.1s⁻¹ of the *fast cycle* (a) initiated micro crack at the bulge and (b) higher magnification image with a detailed view of the micro cracks.

Figures 59 show the micrographs of the specimens deformed at 1140°C for 0.1s⁻¹ and 0.005s⁻¹. The specimens deformed at 1140°C for 0.1s⁻¹ shows wedge cracks at the edge of the specimen (Figure 59 (a)). Kinking of the α_2/γ colonies is marked by rectangle in Figure 59 (b). No other damage kinds could be found in the specimens deformed at 1140°C. The specimen deformed at 1220°C and 0.005s⁻¹ reveals a pore close to the TiB precipitate, as shown in Figure 59 (c). No damage could be observed at higher temperatures shown as example in Figure 59 (d) for the specimen deformed at 1300°C and 0.005s⁻¹.
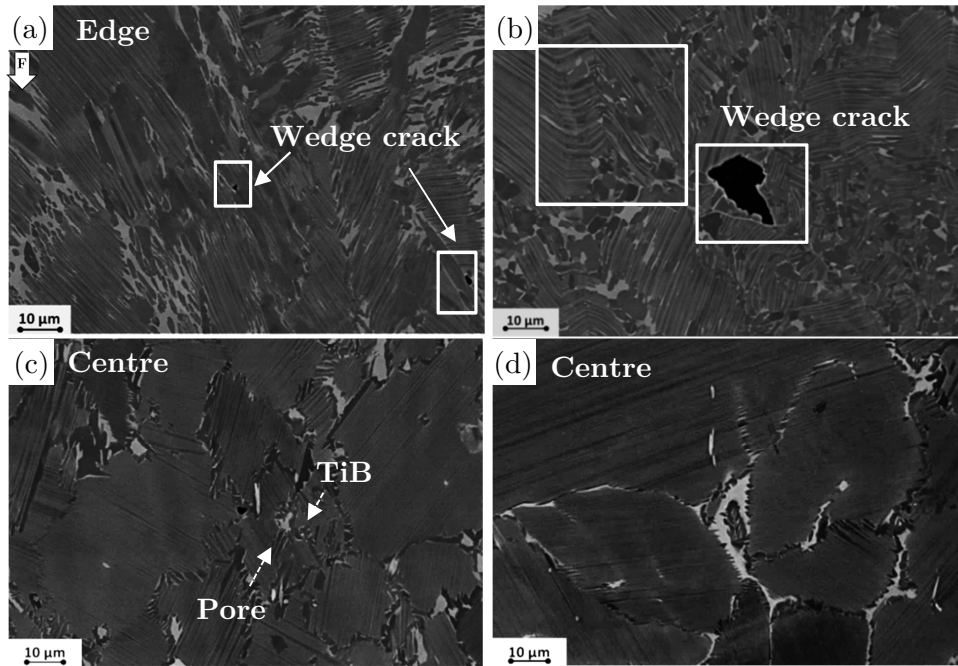
Figure 59: Micrograph of the specimen deformed at 1140°C (a) 0.1s⁻¹, (b) 0.005s⁻¹, (c) 1220°C, 0.005s⁻¹ and (d) 1300°C, 0.005s⁻¹.

Wedge cracks are mostly seen for low temperature range 1140-1220°C and strain rates 0.05-0.005s⁻¹. The bulged areas of the deformed specimens show more damage compared to the areas of the centre. Deformation at low temperatures and high strain rates provoked most damage in the form of wedge cracks and cracks. Wedge cracks are formed at 1140°C and low strain rates, pores at 1220°C and no damage was observed when deformation takes place at temperatures higher than 1220°C.

4.1.7.2 *Slow cycle*

Wedge cracks appear both at the centre as well as at the bulged areas of the specimen deformed at 1140°C and 1s^{-1}. The wedge cracks are oriented along the prior α grain boundary. Refined grains are observed throughout the specimens (Figures 60 (c) and (d)). Specimens deformed at 1140°C and 1s^{-1} present mainly γ$_g$ in the β$_o$ phase (Figures 60 (e) and (f)). The specimen deformed at 1260°C and 0.1s^{-1} shows many wedge cracks located inside the α$_2$/γ colonies at the edge of the sample (see Figure 60 (g) and (h)).
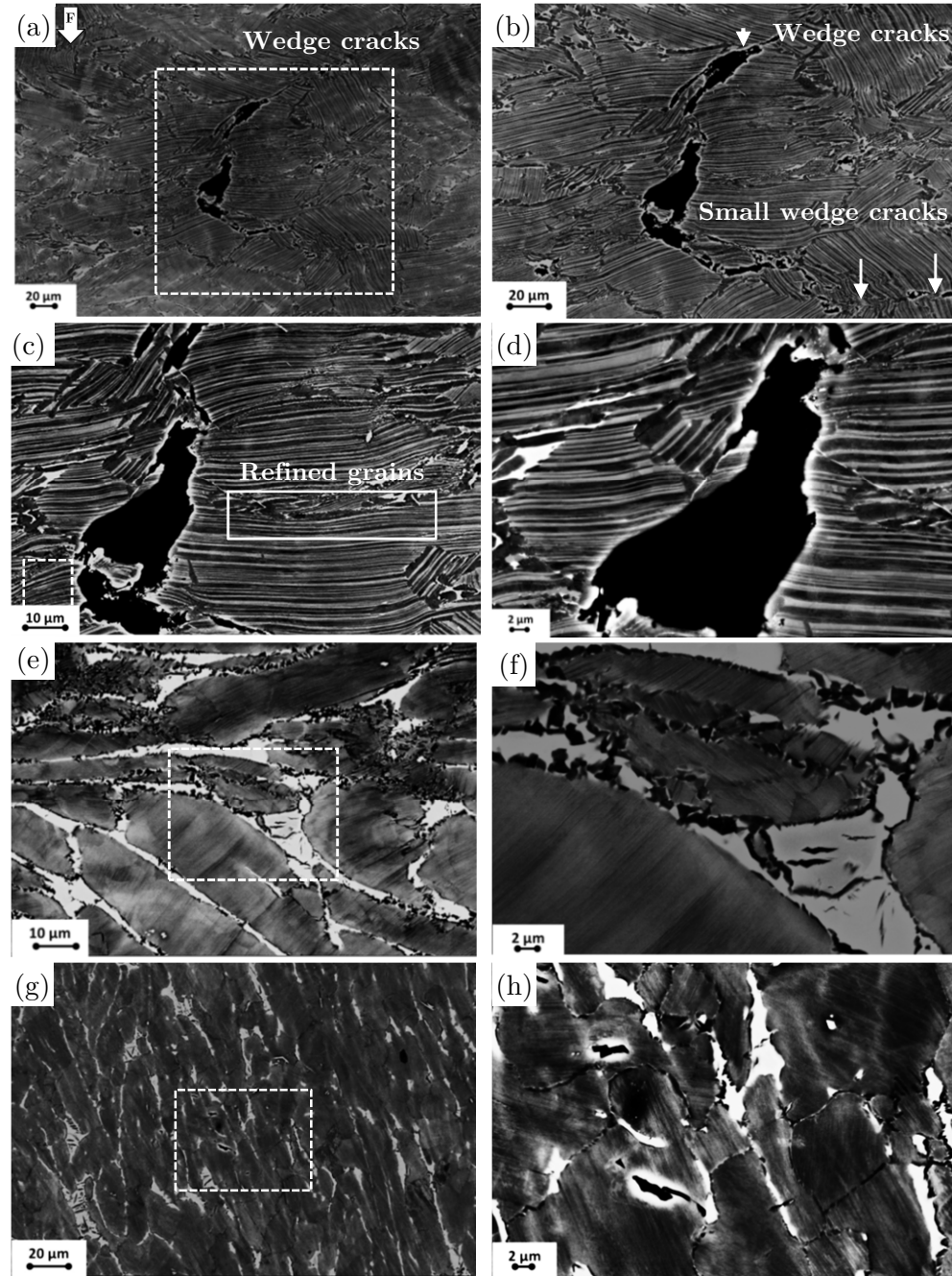
Figure 60: Microdamage investigations of specimens deformed at (a)-(d) 1140°C, 1s^{-1}, edge with wedge cracks, (e), (f) 1140°C, 1s^{-1} centre with γ$_g$ in the β$_o$ phase and (g), (h) edge of the specimen deformed at 1260°C, 0.1s^{-1} showing cracks within the α$_2$/γ colonies.

The micrograph in Figure 61 (a) shows the damage in a specimen deformed at 1140°C and a strain rate of 0.005s^{-1}. Many microcracks induced during deformation are primarily oriented parallel to the compression axis. Locally, however, the crack pathway is influenced by the orientation of the colonies. A detailed overview with a higher magnification of the specimen deformed at 1140°C, 0.005s^{-1} is shown in Figure 61 (b). Some small cracks act as bridges to larger ones (see Figure 61 (b)). The new cracks were formed close to the main micro crack. The arrows mark the point where one crack is located, which is located at the interface of γ globular and γ lamellae. No new cracks appear in the γ_g phase. The cracks spread mainly in translamellar direction over the microstructure. The detailed crack path observed in Figure 61 (b) is a combination of intralamellar, interlamellar and translamellar.
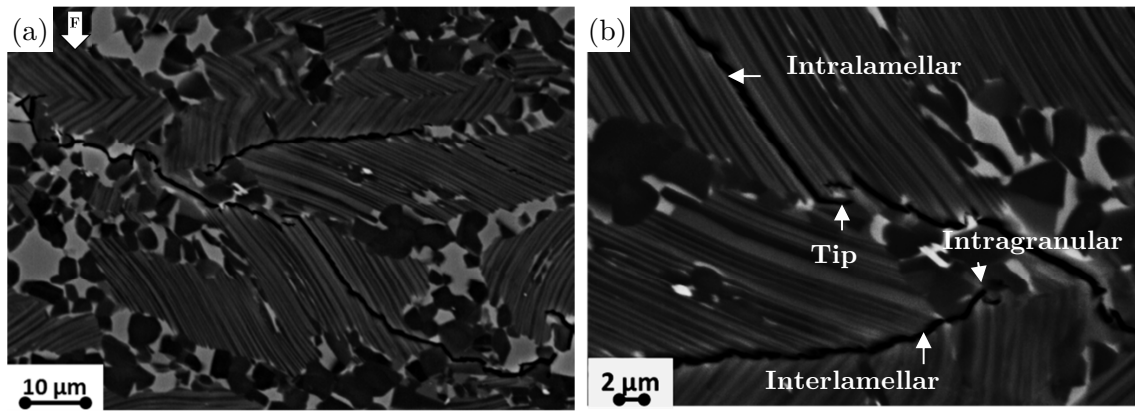
Figure 61: Micrographs of the damage investigations of the specimen deformed at 1140°C and 0.005s^{-1}.

Figures 62 show images with different magnifications of the longitudinal section of the specimen deformed at 1260°C, 0.1s^{-1}. The microstructure consists primarily of very fine α_2/γ colonies with small amounts of β_o phase. In the longitudinal section the surface presents many cracks parallel to the compression axis (see Figure 62 (a)). However, cracks also appear at the outer edge. In this case their orientation is different from the compression axis. The cracks from the outer edge penetrate deeply into the sample. The lengths and the widths of the cracks cover a wide range. As shown in (b), the crack propagation, as mentioned above, is mainly parallel to the compression axis, but also directed towards the lamellar orientations in the colonies. Some cracks propagate intergranular for a short range but the translamellar propagation becomes more determining. Crack bridging is observed, as shown in the magnified view in Figure 62 (c). The micro crack tips are mainly located either inside the β_o phase or at the interface between β_o and α_2/γ colony boundaries.
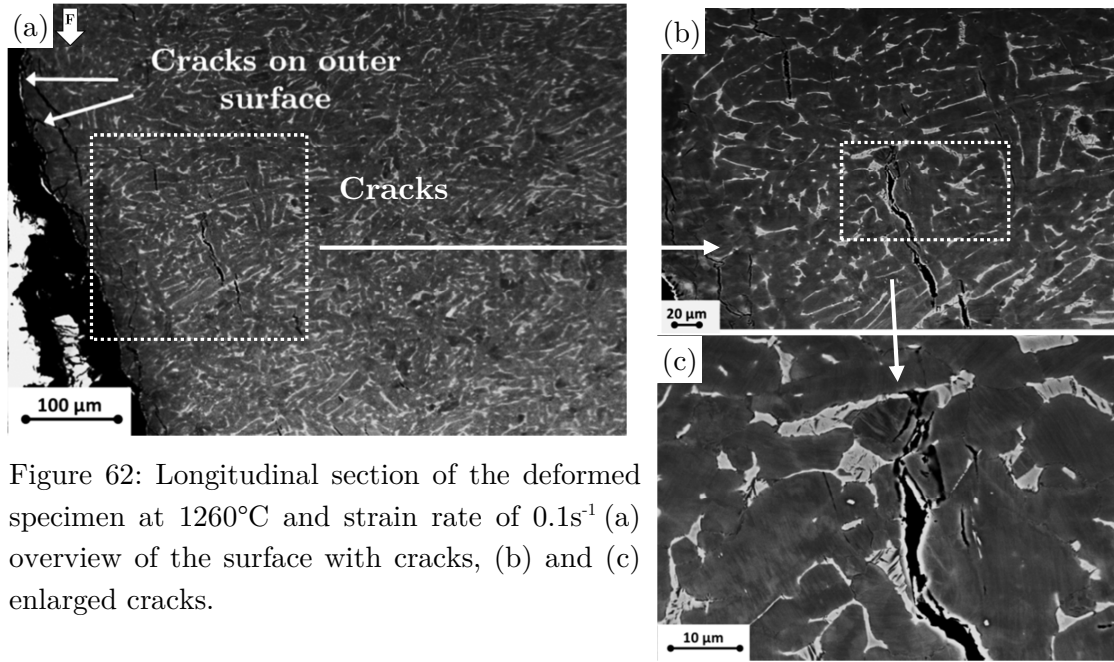
Figure 62: Longitudinal section of the deformed specimen at 1260°C and strain rate of 0.1s^{-1} (a) overview of the surface with cracks, (b) and (c) enlarged cracks.

In order to describe the micro damage as a function of temperature and strain rate, the damage characteristics have been summed up in "damage maps". Damage was analysed at the edge and at the centre of the deformed specimens. The maps are shown in Figures 63 for (a) the edge and (b) the centre of the deformed specimens. From Figure 63 (a) it is visible that wedge cracks are observed at temperatures between 1140-1220°C from high to moderate strain rates. The temperatures 1220-1260°C reveal wedge cracks at the edges for all strain rates. Micro cracks are visible for the temperatures 1140-1180°C and for the strain rates of 0.05-0.005s^{-1}. A shear band is observed for the specimen deformed at 1140°C and a strain rate of 1s^{-1}. Furthermore, Figure 63 (a) shows that the high temperatures between 1300-1340°C and that moderate to slow strain rates produce micro pores in the microstructures. The centres of the deformed specimens show wedge cracks as far as 1200°C for all strain rates and in the temperature range from 1200-1260°C for the high strain rates (Figure 63 (b)). The specimen deformed at 1260°C reveals wedge cracks for all analysed strain rates. Shear band occurs for the lowest temperature and the highest strain rate. Pores are observed for the specimen deformed at 1220°C and the strain rate 0.005s^{-1}. The centres of the specimens deformed at temperatures above 1260°C show no damage at all.
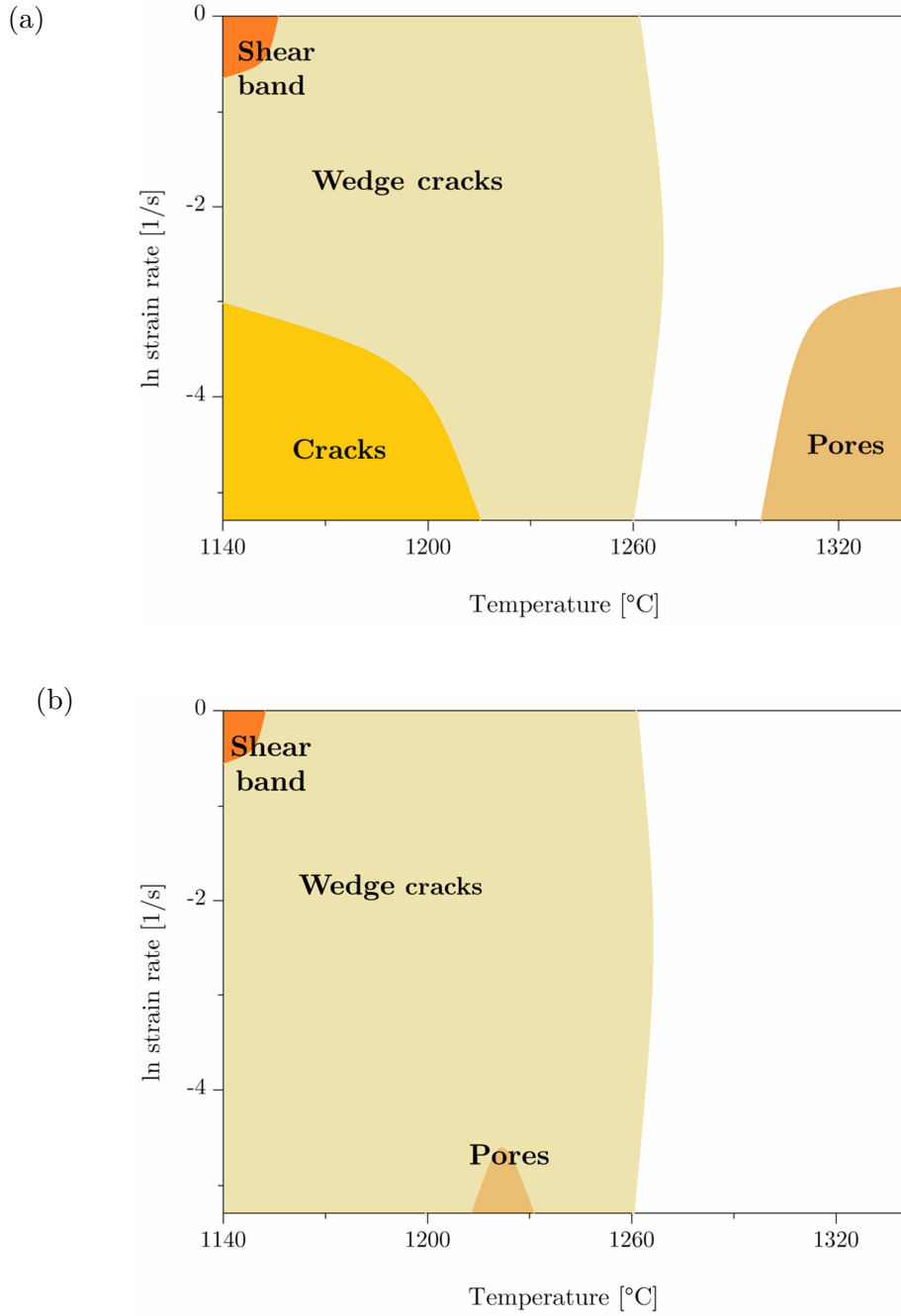
Figure 63: Experimental damage maps of deformed specimens showing damage found at different temperatures and strain rates at the (a) edges and (b) centres of the specimens. The areas of damage are marked by lined rectangles.

Furthermore the influence of B-rich precipitates on micro damage has been analysed. The SEM (BSE) pictures of the deformed specimens with precipitates enriched in Nb, B and Mo are illustrated in Figures 64, where the precipitates appear bright and every kind of damage is dark. The precipitates are marked with rectangles and the pores are identified by arrows. The pores are located very close to these brittle precipitates, as shown in Figure 64 (a). One large precipitate with a size of approximately 40µm is marked in the specimen deformed at 1260°C and 0.005s^{-1} (see Figure 64 (b)).
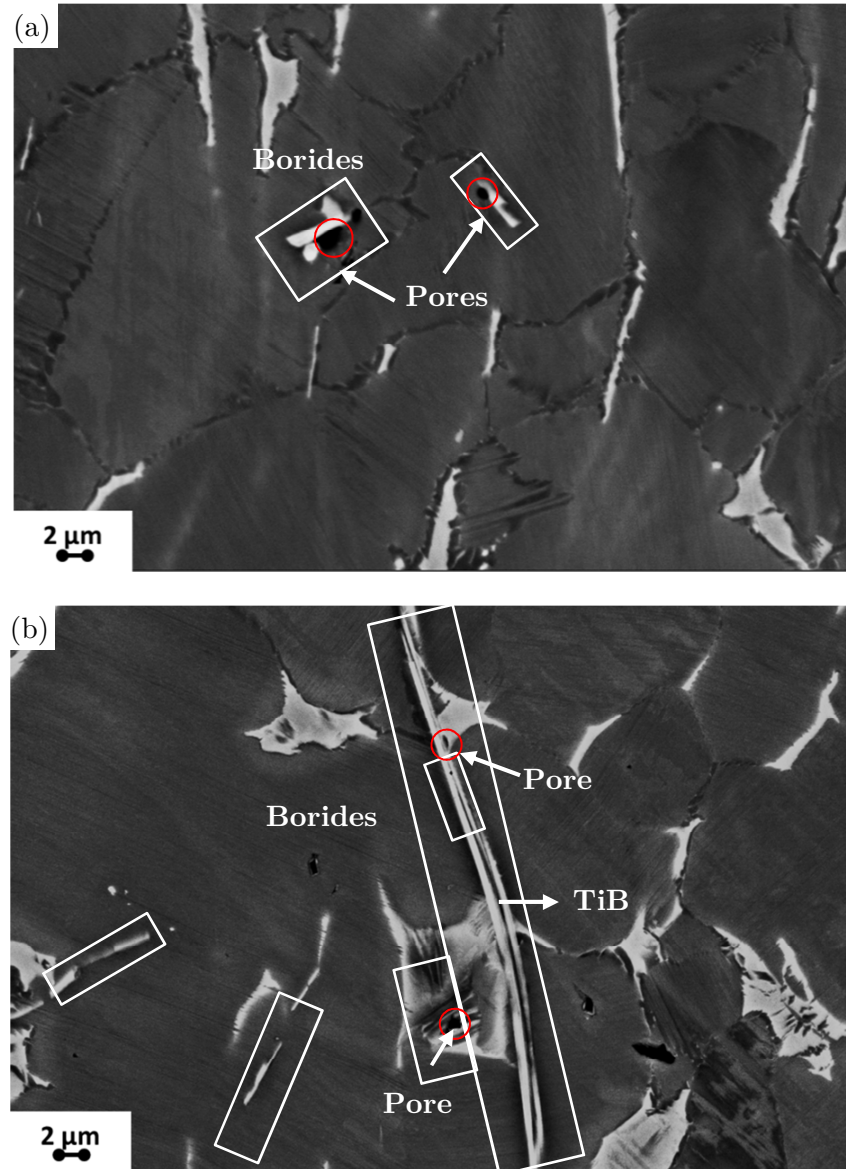
Figure 64: SEM micrograph of the deformed specimen (a) 1220°C, 1s^{-1} and (b) 1260°C, 0.005 s^{-1} showing precipitates enriched with B, Nb and Mo with damage close to them.

The microstructures of selected hot deformed specimens were further analysed by EBSD measurements. The investigated areas were all taken from the edge of the deformed specimens subjected to intensive damage. Figures 65 show the image quality maps overlapped with the phase maps. The yellow colour represents the γ phase, red the α_2 phase and the green the β_o phase.
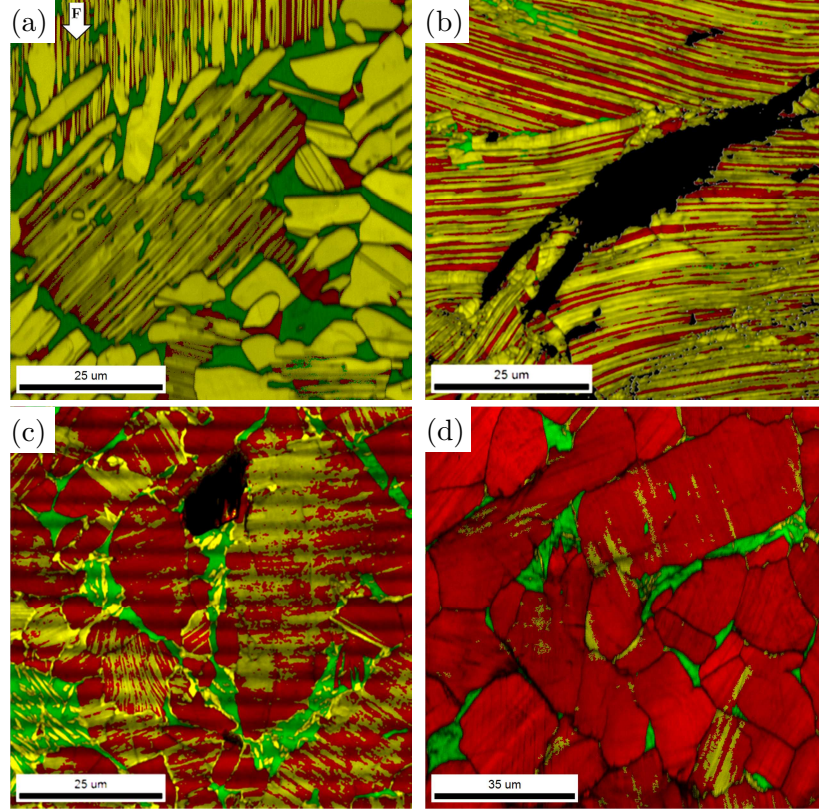
Figure 65: Image quality maps with overlapped phase maps of (a) as-received condition and after deformation at (b) 1140°C and 1s^{-1}, (c) 1260°C and 1s^{-1} and (d) 1260°C and 0.005s^{-1}, yellow=γ, red=α$_2$, green=β$_o$ and black shows damage.

The specimen deformed at 1140°C at a strain rate of 1s^{-1} reveals a higher α$_2$ phase content compared to the as-received condition. The specimen deformed at 1260°C shows the largest amount of α$_2$ phase. The lowest fraction of γ phase is observed after deformation at 1260°C, which corresponds to the γ solvus temperature. A proper distinction between the α$_2$ and γ lamellae in the specimen at 1260°C is not possible due to the limited resolution of SEM. The phase quantifications are summarised in Table 6.

Table 6: Quantifications of the phase fractions in the as-received and deformed specimens.

	α$_2$ phase vol.-%	β$_o$ phase vol.-%	γ phase vol.-%
As-received	9.7	15	74.9
1140°C, 1s^{-1}	31.7	2.9	65.3
1260°C, 1s^{-1}	54.8	10	34.4
1260°C, 0.005s^{-1}	89.8	5.3	4.9

Figure 66 shows the standard colour triangles correlated to the crystallographic orientation maps showed in Figure 67.

γ phase   β₀ phase   α₂ phase
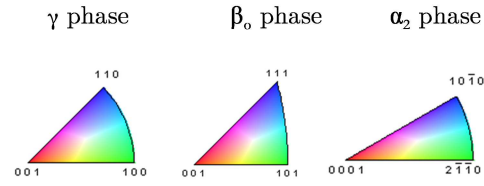
Figure 66: Standard colour coded triangles used for the phases measured in the titanium aluminide.

In the grain orientation maps of the HAGBs and LAGBs are depicted in Figures 67. HAGB are marked with black lines and LAGB are white. Subgrains are mostly located in the β_o and α_2 phases.
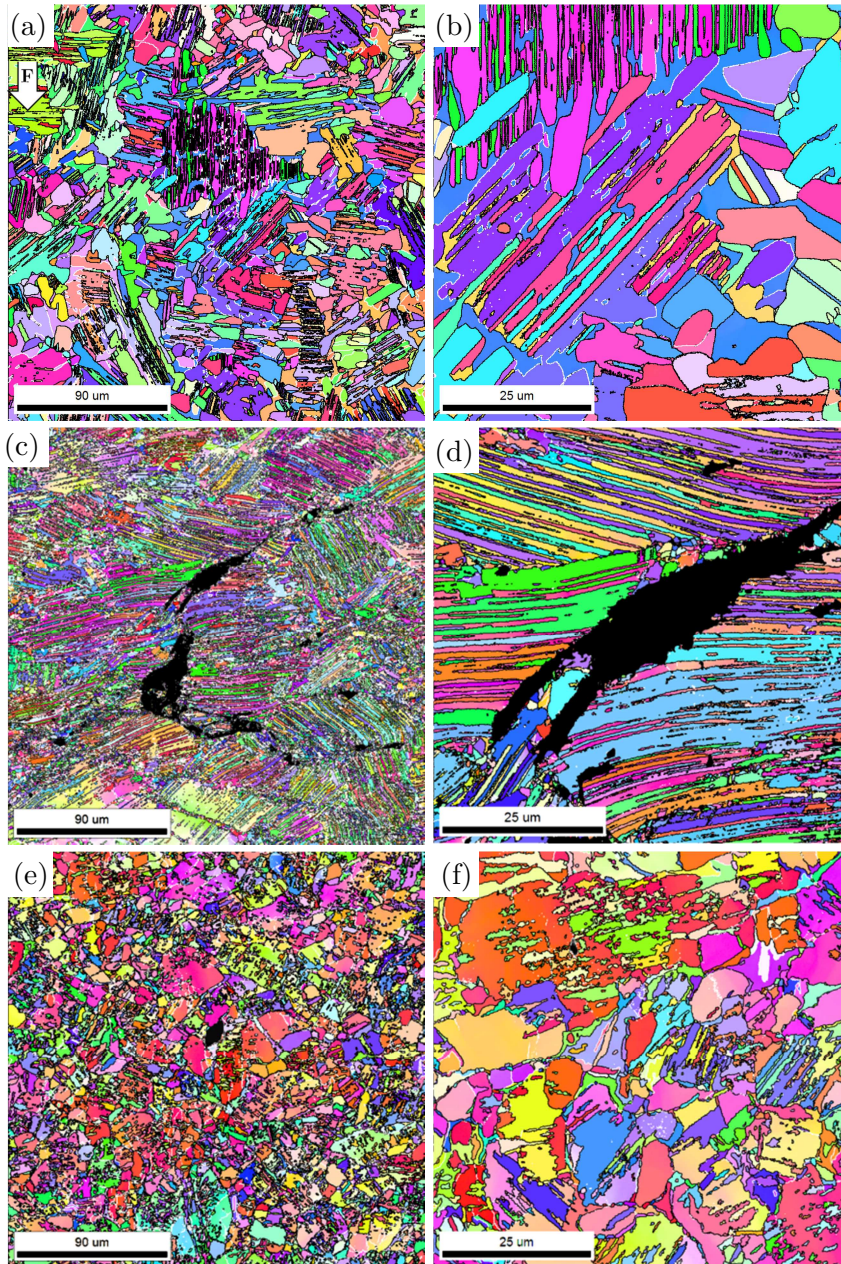
Figure 67: IPF maps with HAGB (black) and LAGB (white) and of (a), (b) as-received condition, (c), (d) 1140°C, 1s⁻¹ and (e), (f) 1260°C, 1s⁻¹.

The image quality maps of the specimen deformed at 1140°C and 1s⁻¹ are shown in Figures 68 (a)-(d). There are many slip bands in the γ phase, as shown in Figures 68 (a) and (d). The slip band are oriented parallel to the compression direction.
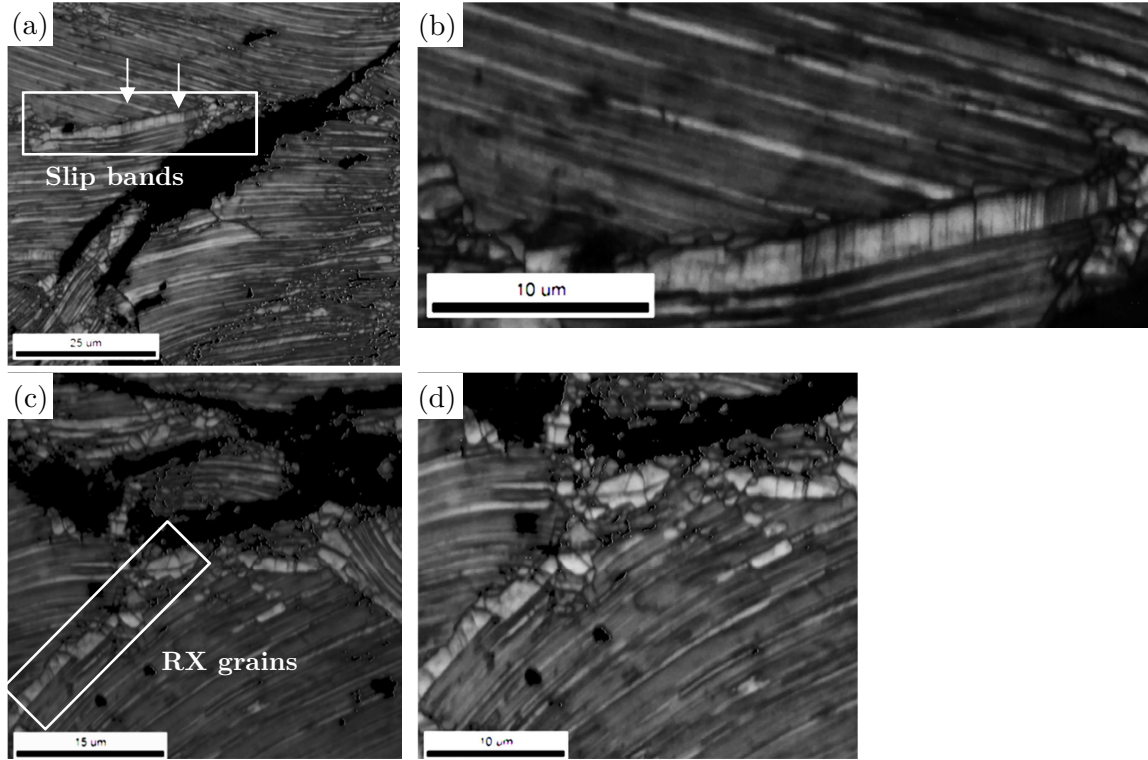
Figure 68: Image quality maps of the deformed specimen at 1140°C, 1s⁻¹ within slip bands.

Figure 69 shows the kernel average misorientation (KAM) map of each phase for specimens in (a) as-received condition and deformed at (b) 1140°C, 1s⁻¹, (c) 1260°C, 1s⁻¹ and (d) 1260°C, 0.005s⁻¹. Kernel average misorientation between 0-5° was set for the calculation and was generated with the first neighbour. The blue colour in the kernel misorientation maps represents a lower local misorientation, while red shows a high degree of local misorientation. High misorientation is observed around the crack tips as the crack itself. HAGBs (black) are mainly located in the γ phase and LAGBs (red) in the other two phases for all four conditions. The γ phase shows almost no local misorientation, while the α₂ phase has a higher degree of misorientation.
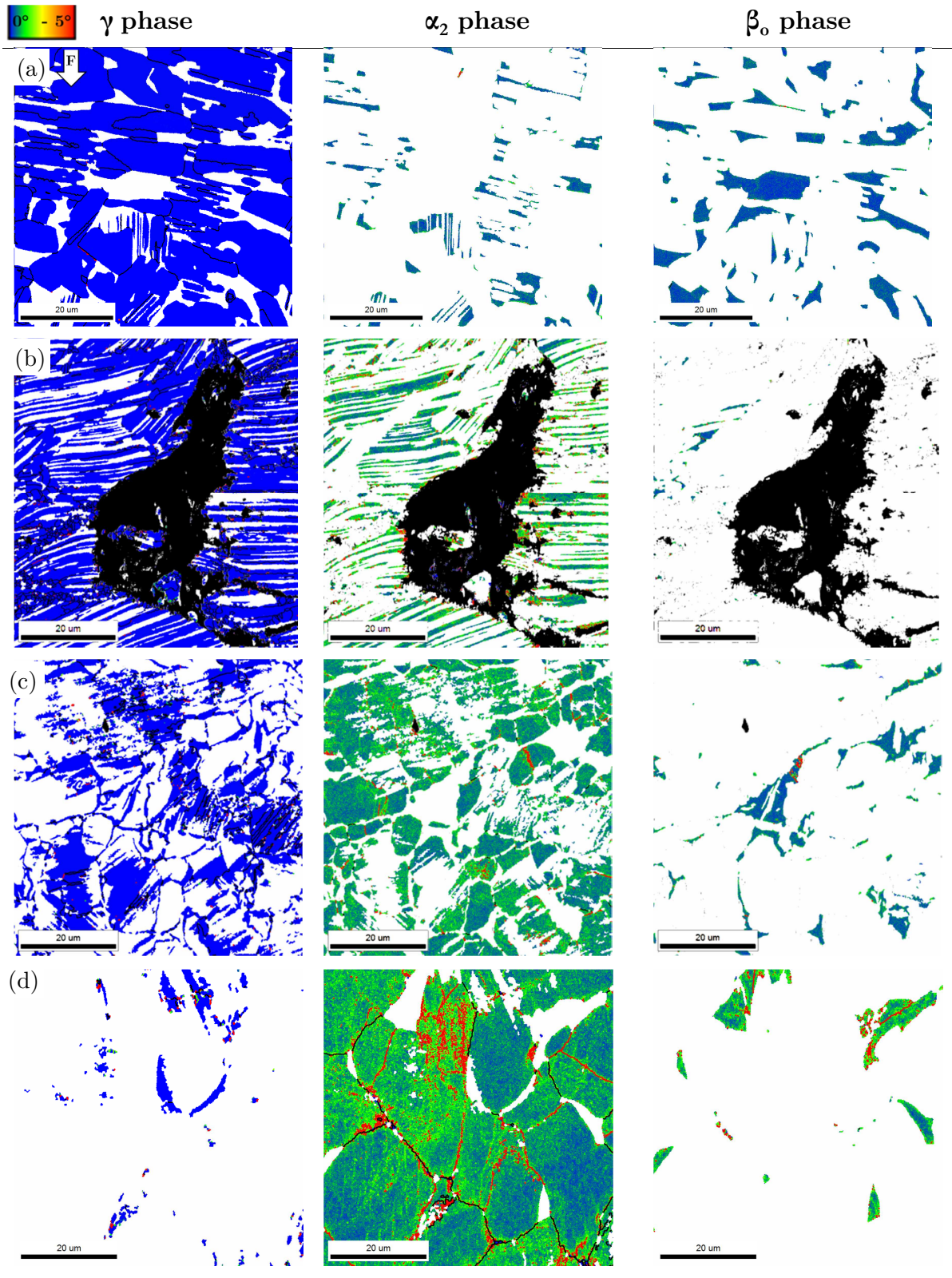
Figure 69: Kernel average misorientation profiles of the γ, α₂ and β₀ phases (a) in the as-received condition, (b) deformed at 1140°C, 1s⁻¹ with a wedge crack, (c) deformed at 1260°C, 1s⁻¹ with a pore within the microstructure and (d) the microstructure deformed at 260°C, 0.005s⁻¹.

4.2 Modelling

4.2.1 Flow curves

The flow behaviour of the nominal TNM alloy under hot deformation conditions was modelled using the modified TANH model based on Eq. 2 (2.3.1).

$$\sigma = \left[A + B\varepsilon^n \left(\frac{1}{exp(\varepsilon^a)} \right) \right] \left[exp(q + Cln\dot{\varepsilon}) \right] \left[1 - \left(\frac{T}{T_d} \right) \left(\frac{T - T_r}{T_m - T_r} \right)^p \right] \left[D + (1 - D)tanh \left(\frac{1}{(\varepsilon + S)^c} \right) \right] \qquad \text{Eq. 42}$$

$$\underbrace{\qquad\qquad}_{\text{hard.+ soft.}} \quad \underbrace{\qquad}_{\dot{\varepsilon}\ \text{sensitivity}} \quad \underbrace{\qquad\qquad}_{\text{temp. term}} \quad \underbrace{\qquad\qquad\qquad}_{\text{soft.}}$$

$$\text{With } D = 1 - \left(\frac{T}{T_m} \right)^d \text{ and } S = \left(\frac{T}{T_m} \right)^b$$

The material parameters and constants of the TANH model for the *slow cycle* are given in Table 7.

Table 7: Adjusted constants for the modified TANH model.

A (MPa)	a	B (MPa)	b	C	c	d	n	p	q
827.6	0.650	1200	0.5	0.281	2.0	1.00	0.394	0.488	0.31

Figures 70 show a detailed comparison between the experimental and modelled flow stress curves under different strain rates (a) 1s^{-1} and (b) 0.1s^{-1}. The modelled flow curves are plotted using dashed lines and the measured ones by full lines. Many modelled flow curves differ from the experimentally determined ones.
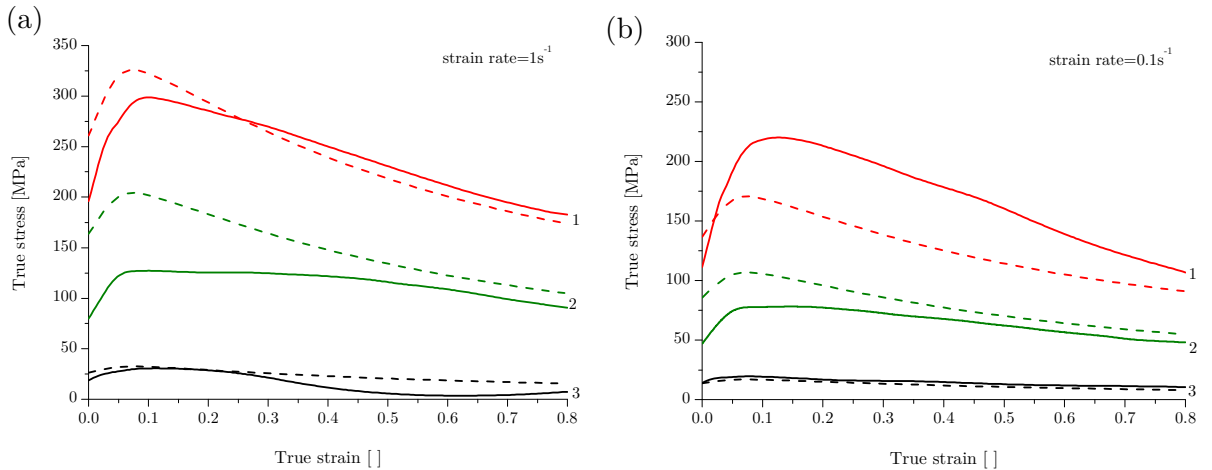
Figure 70: Comparison modelled and experimental flow curves of the *slow cycle* for several strain rates (a) 1s^{-1}, (b) 0.1s^{-1} and temperatures 1: 1140°C, 2: 1220°C, and 3: 1340°C.

4.2.2 Strain rate sensitivity maps

4.2.2.1 *Fast cycle*

The strain rate sensitivity values calculated for the *fast cycle* at strains of 0.2, 0.4 and 0.6 are shown in Figures 71 as a function of temperature and strain rate. The dashed zones represent the negative m values. Negative m values appear at temperatures below 1180°C and high strain rates. Further, negative m values occur at temperatures above 1200°C and low strain rates. High m values occur at high strain rates. An increase in the strain causes the negative m area to increase at high temperatures.

(a) ε=0.2

(b) ε= 0.4

(c) ε=0.6
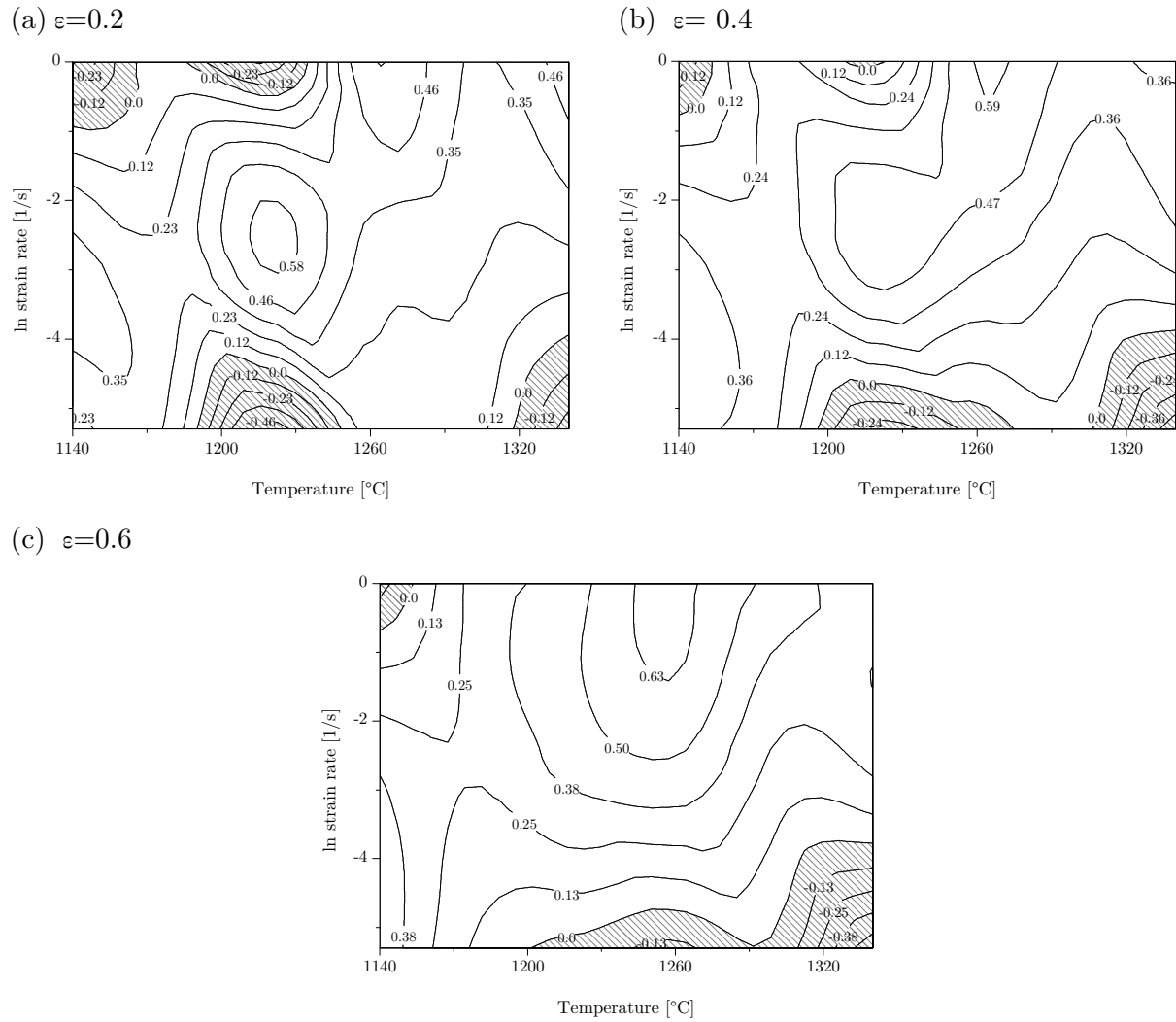
Figure 71: Strain rate sensitivity maps of the *fast cycle* calculated at strains of (a) 0.2, (b) 0.4 and (c) 0.6.

4.2.2.2 *Slow cycle*

The calculated strain rate sensitivity maps of the *slow cycle* for different strains are depicted in Figure 72. The m maps at strains of 0.2, 0.4, 0.6 and 0.8 show negative m values for the lowest temperature and the highest strain rate. Negative m values occur at high strain rates, as can be seen in Figure 72 (b), (c) and (d). High m values appear at low strain rates at temperatures between 1200°C and 1300°C.
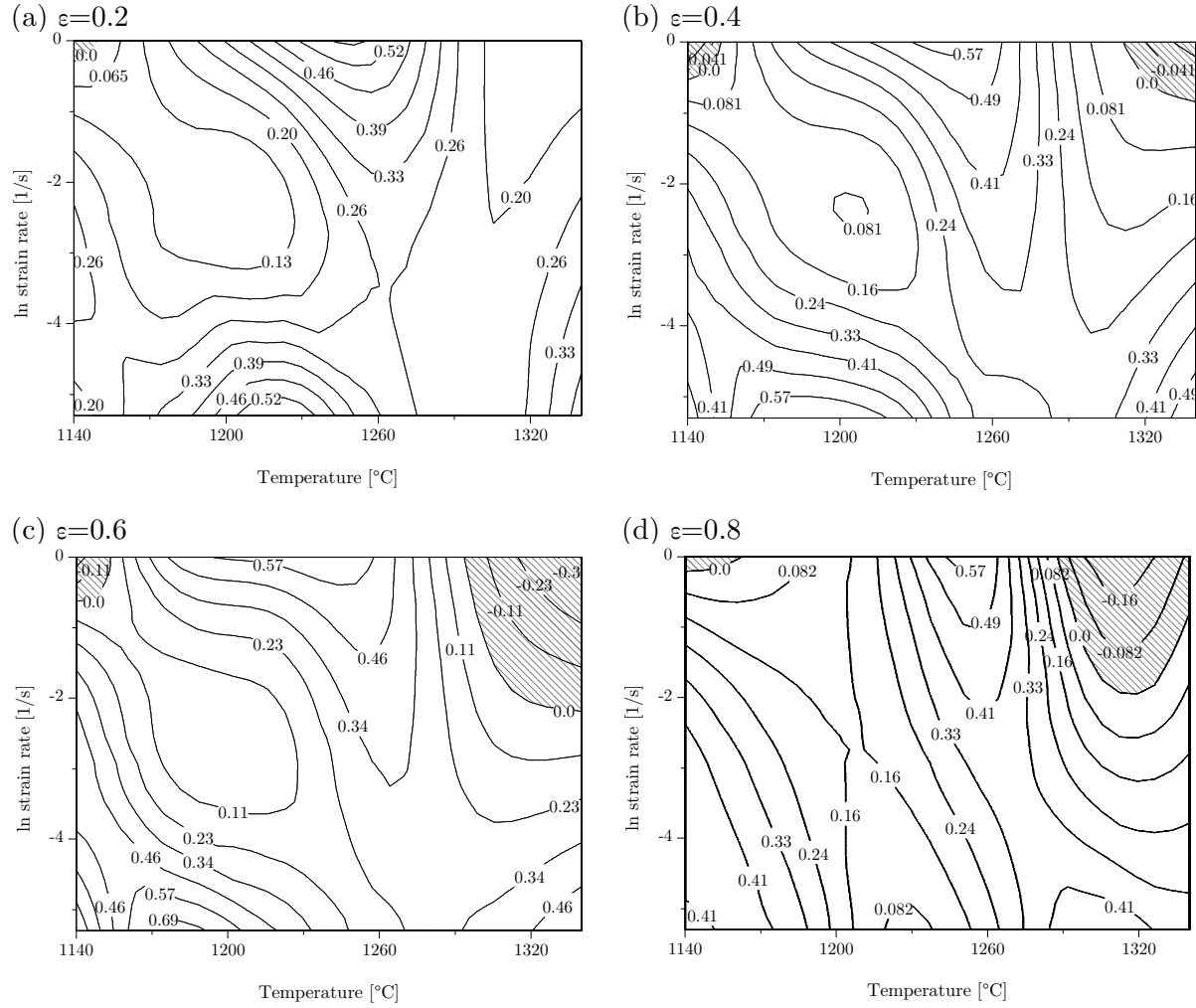
Figure 72: Strain rate sensitivity maps of the *slow cycle* calculated at strains of (a) 0.2, (b), 0.4, (c) 0.6 and (d) 0.8.

4.2.3 Processing maps after DMM

4.2.3.1 *Slow cycle*

The processing maps obtained after DMM are shown from Figure 73 to 75. The numbers at each contour in the maps represent the efficiency of power dissipation after Prasad η_P and Murty and Rao η_{MR}. The shaded areas correspond to ξ, κ or $\kappa_j < 0$. The strain rate sensitivity map at a strain of 0.2 in

Figure 73 shows negative η_P values at the highest strain rate and lowest temperature. The efficiency of power dissipation after Prasad's model shows exactly the same tendency as the strain rate sensitivity map after Eq. 5.
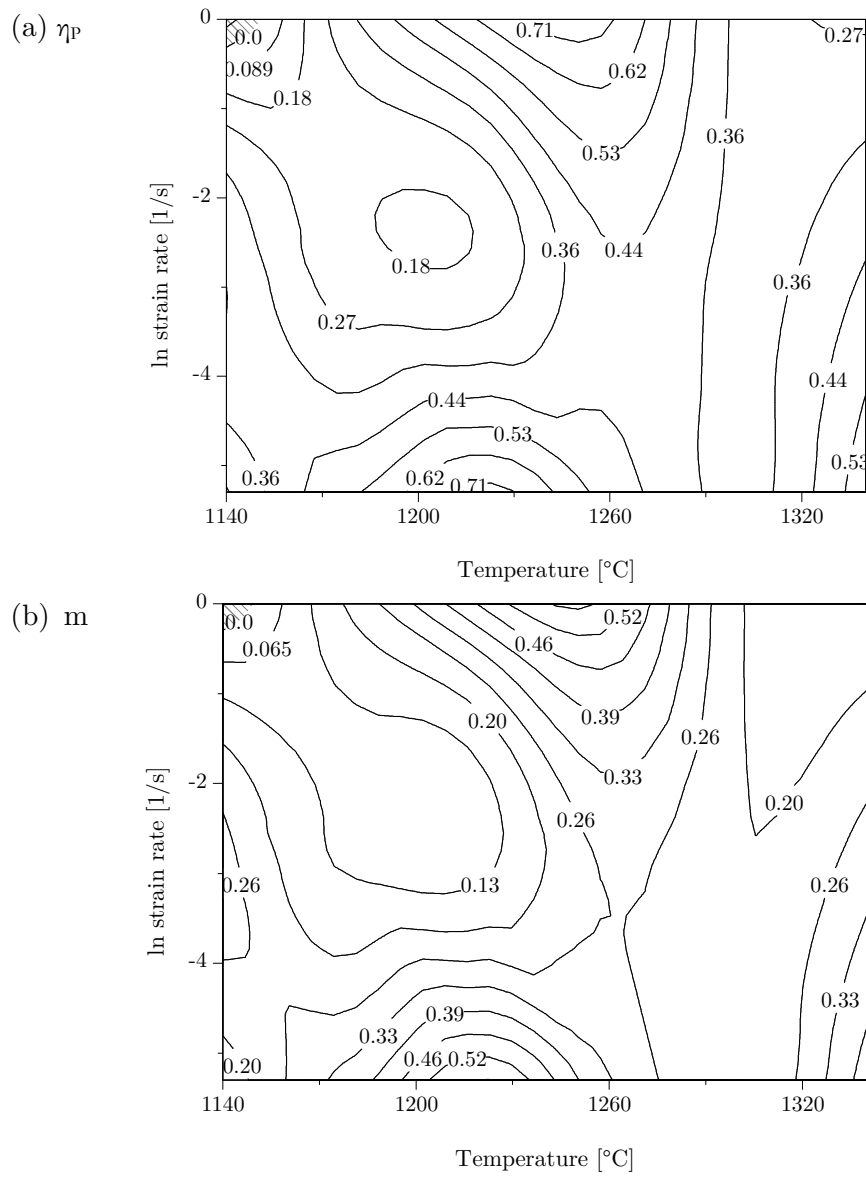
Figure 73: Maps calculated at a strain of 0.2: (a) efficiency of power dissipation η_P and (b) strain rate sensitivity m with dashed areas for negative values.

The instability criterion ξ shows negative values at low temperatures: 1140 -1240°C for low strain rates. At low strain rates the η_P reveal high values. The temperatures from 1300°C to 1340°C combined with high strain rates also show negative ξ values, as shown in Figure 74 (a). The predictions by the instability criterion K show the same tendency like ξ. The processing map based on η_{MR} with the instability criterion K_J is shown in Figure 74 (c). K_J is negative at low temperatures 1140-1200°C and strain rates of 1-0.1s⁻¹. Furthermore, negative K_J are obtained for the strain rate 0.005s⁻¹ at 1220-1240°C and the temperatures at 1300-1340°C and the high strain rates.

(a) $\eta_P + \xi$

(b) $\eta_{MR} + K$

(c) $\eta_{MR} + K_j$
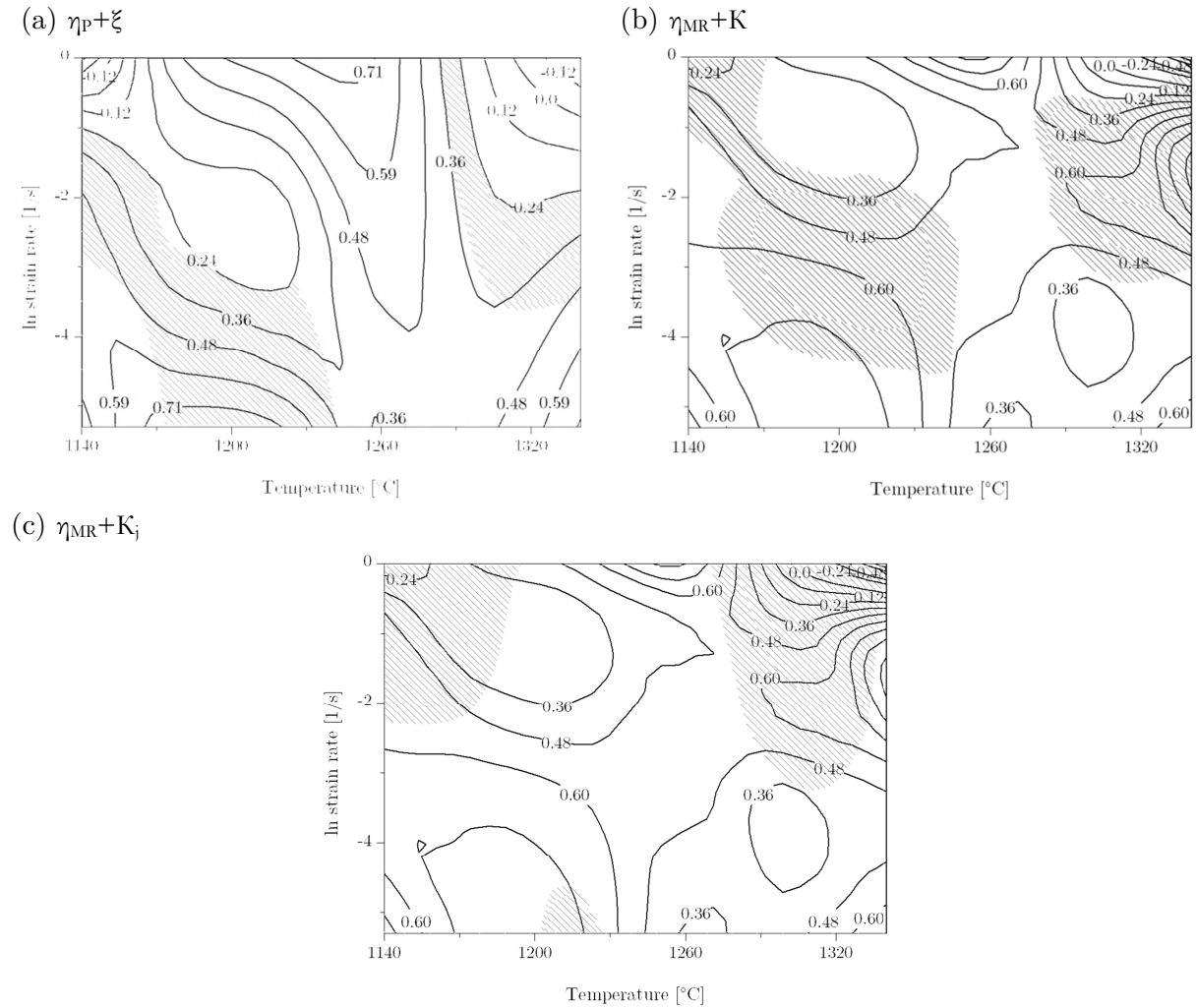
Figure 74: Processing maps calculated at a strain of 0.4 with different efficiency parameters and instability parameters (dashed zones).

Figure 75 depicts the calculated processing maps at a strain of 0.8 after different models. At temperatures between 1140-1200°C and at strain rates between 1-0.005s^{-1} low η_P, ξ, K and K_j occur. At temperatures above 1300°C appear even negative ξ, K and K_j values.

(a) $\eta_P+\xi$

(b) $\eta_{MR}+K$

(c) $\eta_{MR}+K_j$
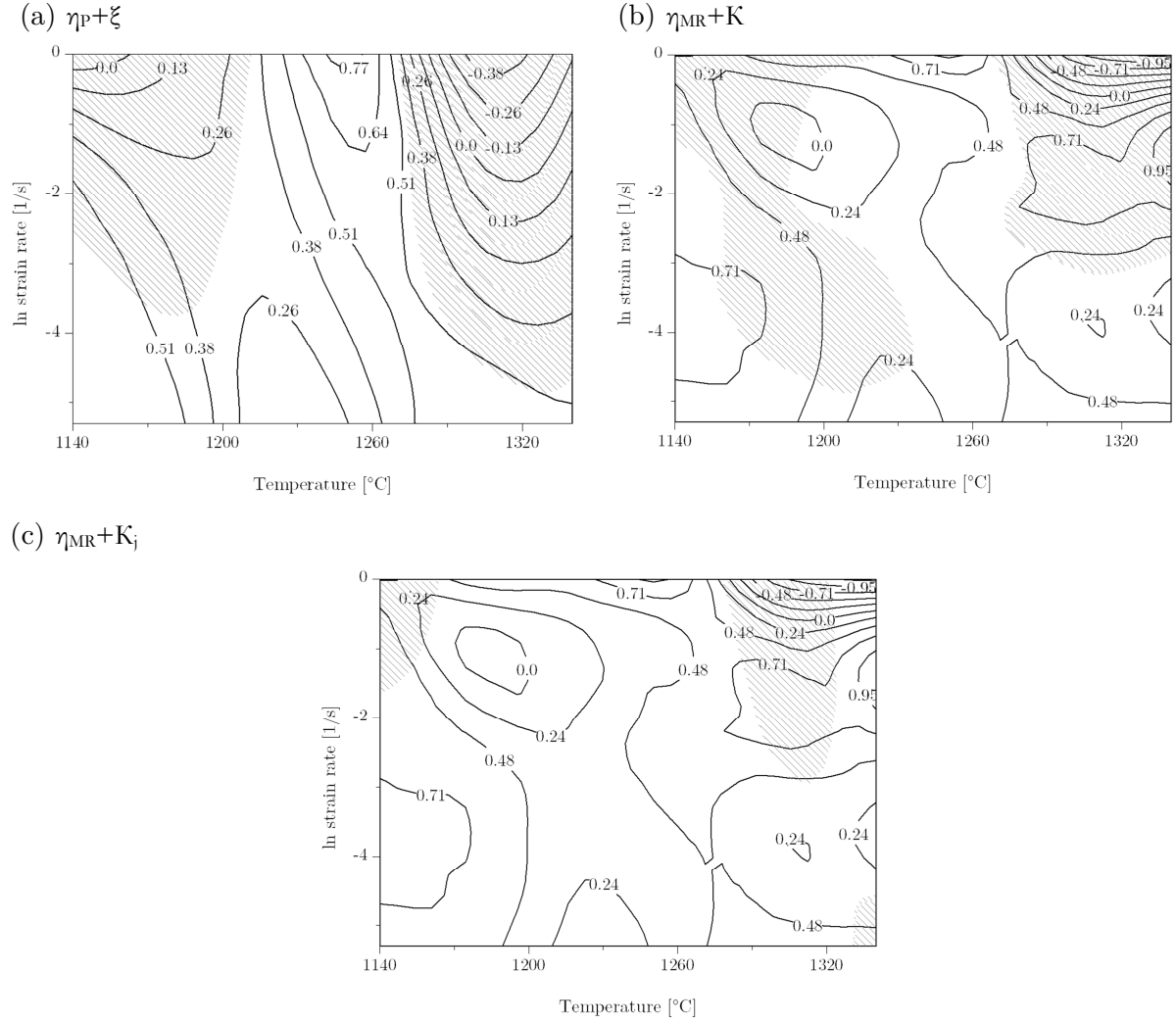
Figure 75: Processing maps calculated at a strain of 0.8 with different efficiency parameters and instability parameters (dashed zones).

4.2.4   Flow localisation and flow softening maps

The flow localisation is described using α_{SJ} parameter after Semiatin and Jonas in Eq. 29. The domains with $\alpha_{SJ}>0$ are dashed in the map in Figure 76 (a). The flow localisation is predicted for $\alpha_{SJ}>3$ in I, II, III and IV, which is shaded grey as shown in Figure 76 (a). The map of the normalised flow softening rate according to Eq. 25 is generated for a total strain of 0.8 and shown in Figure 76 (b). The contour number represents the normalised softening values and the dashed zones correspond to negative values $\gamma'<0$. Domain I shows $\gamma'<-1$, which corresponds to flow localisation. The normalised flow softening is predicted for $\gamma'<0$, as marked by II and III in Figure 76 (b). Positive values correspond to hardening.
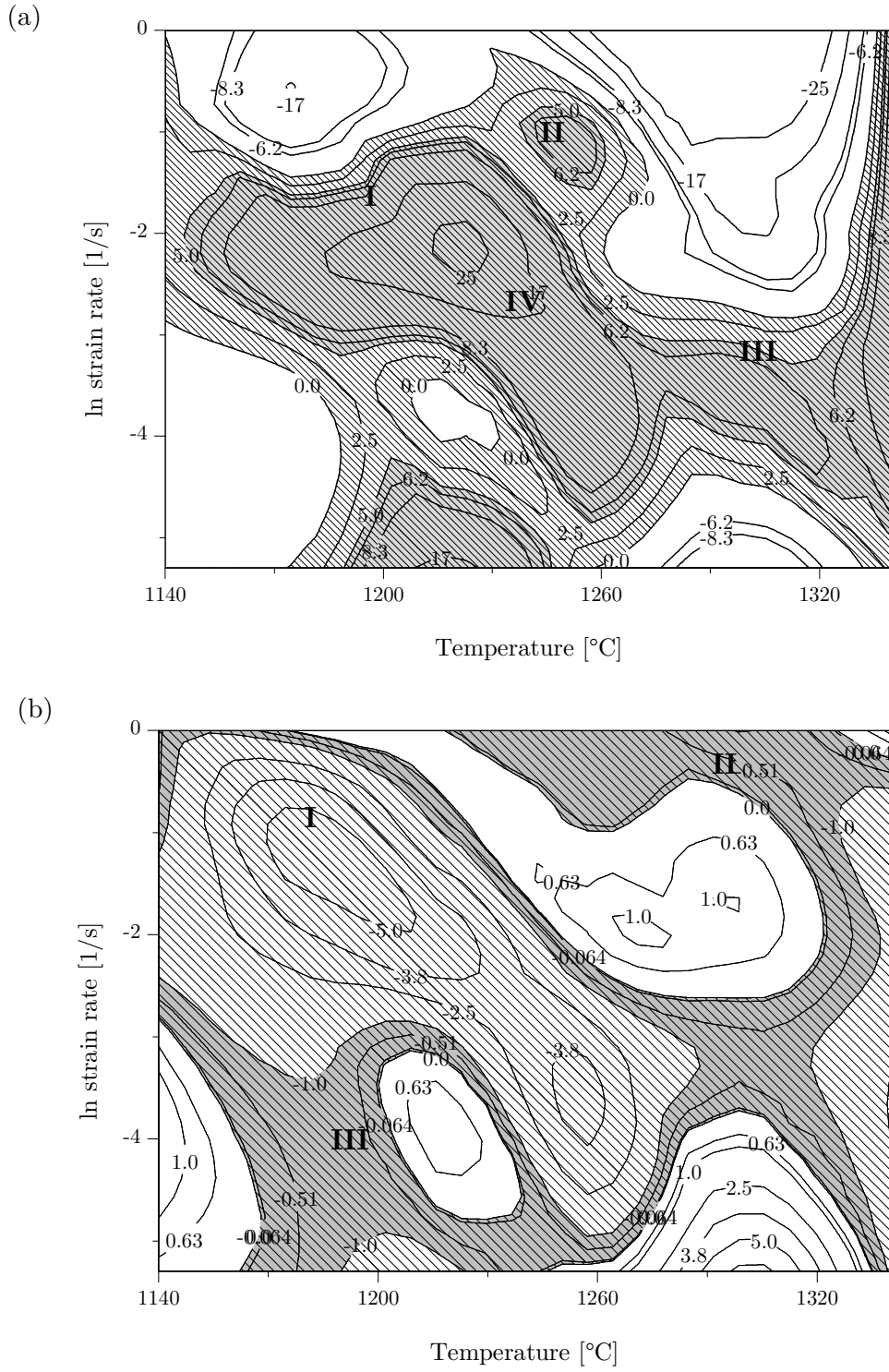
Figure 76: (a) Instability map α_{SJ} at a strain of 0.8, (b) calculated flow softening map at a strain of 0.8 for the slow thermal cycle.

4.3 FEM simulations

4.3.1 Temperature, strain and strain rate distributions

Figure 77 show temperature, effective strain and effective stress distributions developed in the hot compressed samples at temperatures from 1140 to 1300°C and at strain rates of 0.1-1s^{-1} up to a total strain of 0.9. The adiabatic corrected flow stress data of the *slow cycle* were used. The distributions are not homogeneous due to the barrelling and heating methods. Maximum temperatures are localised in the centre of the specimens. The largest values of strain are achieved at the centre of deformed samples, where values of 1.5 local strains are reached. High strains are furthermore localised at the bulge between specimen and loading tools. The stress distributions show high values at the contact area between specimen and loading tool and at the edges of the deformed specimens.
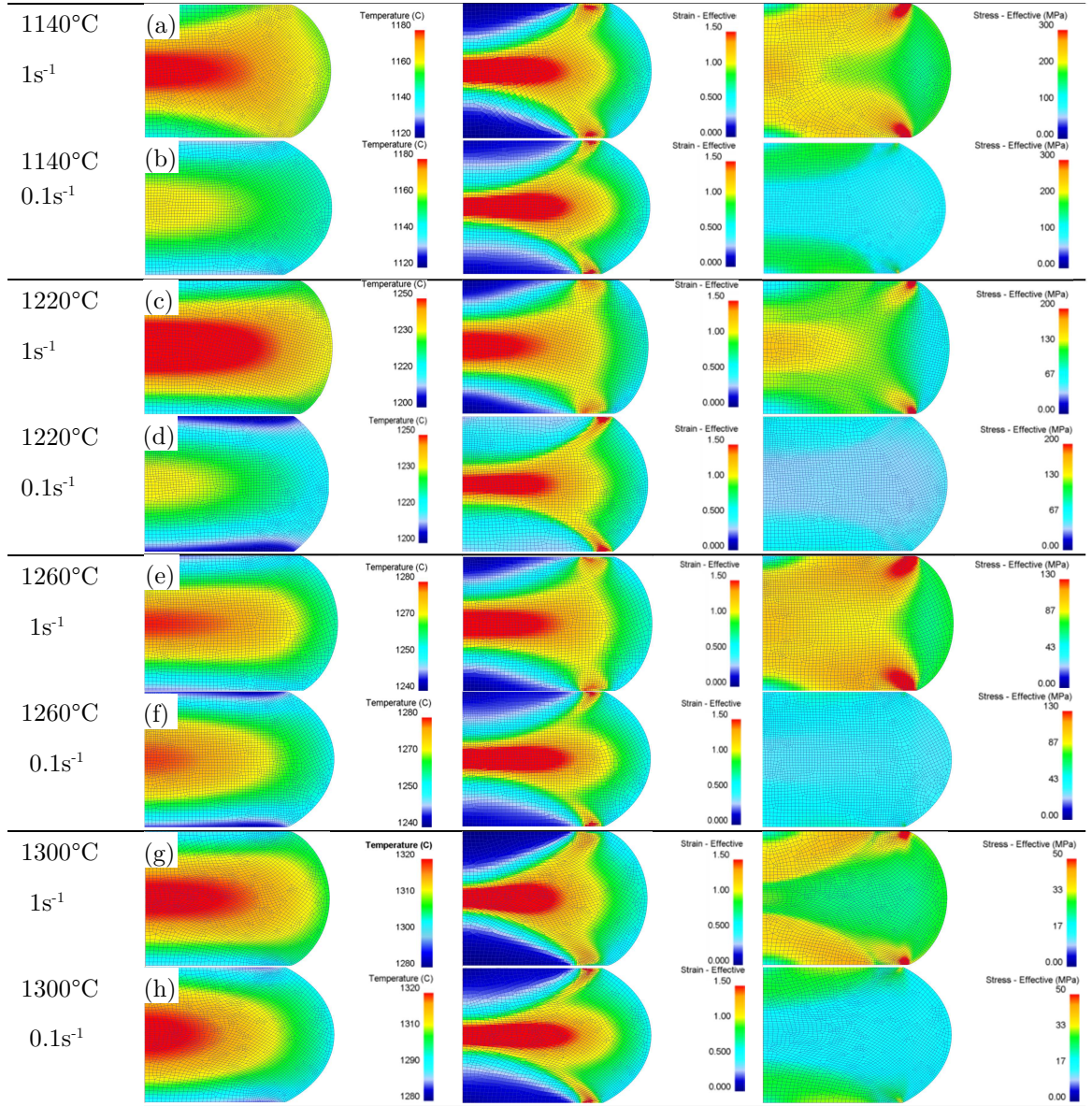
Figure 77: FEM simulation results of deformed samples showing temperature, effective strain- and stress distributions for (a) 1140°C and 1s^{-1}, (b) 1140°C and 0.1s^{-1}, (c) 1220°C and 1s^{-1}, (d) 1220°C and 0.1s^{-1}, (e) 1260°C and 1s^{-1}, (f) 1260°C and 0.1s^{-1}, (g) 1300°C and 1s^{-1} and (h) 1300°C and 0.1s^{-1}.

4.3.2 FE simulations using experimental and modelled flow stresses

Figures 78 show the numerical simulation results using the software DEFORM™. Results of experimental vs modelled flow stress are shown. The resulting effective stress distributions are shown for the specimens deformed at 1140-1300°C for strain rates of 1s^{-1} and 0.1s^{-1}. As can be seen below, different stress values are obtained for the deformed specimens with modelled vs experimental flow curves. However, the specimens simulated with modelled flow curves show in general higher stresses. The qualitative localisation of temperature, strain and stress distributions in the deformed specimens are comparable with experimental and modelled flow stresses.

Nominal	Experimental flow stress	Modelled flow stress
1140°C,1s^{-1}	(a)	
1140°C, 0.1s^{-1}	(b)	
1220°C, 1s^{-1}	(c)	
1220°C, 0.1s^{-1}	(d)	
1260°C, 1s^{-1}	(e)	
1260°C, 0.1s^{-1}	(f)	
1300°C, 1s^{-1}	(g)	
1300°C, 0.1s^{-1}	(h)	
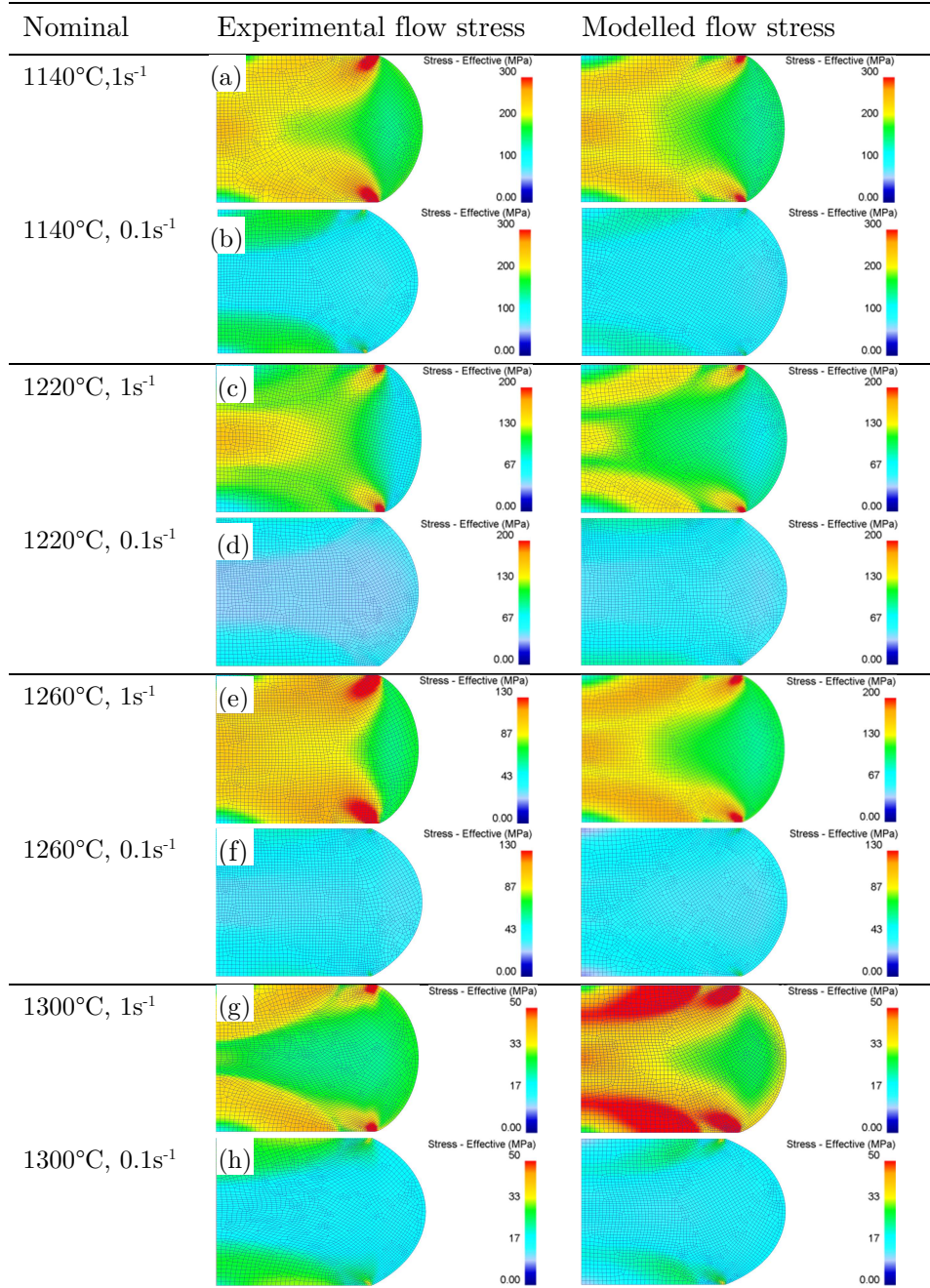
Figure 78: FEM simulation results of deformed samples showing effective stress distributions for experimental vs modelled (a) 1140°C and 1s^{-1}, (b) 1140°C and 0.1s^{-1}, (c) 1220°C and 1s^{-1}, (d) 1220°C and 0.1s^{-1}, (e) 1260°C and 1s^{-1}, (f) 1260°C and 0.1s^{-1}, (g) 1300°C and 1s^{-1} and (h) 1300°C and 0.1s^{-1}.

4.3.3 Macromechanical damage models

Figure 79 depicts FE simulations with selected macromechanical damage models. The highest damage values are coded in warm colours (red). High damage values appear in the bulge region of the sample, while low values are located in the centre. All used ductile damage models showed the same tendency for the applied temperatures and strain rates. The lowest deformation temperature of 1140 °C showed the highest damage values.
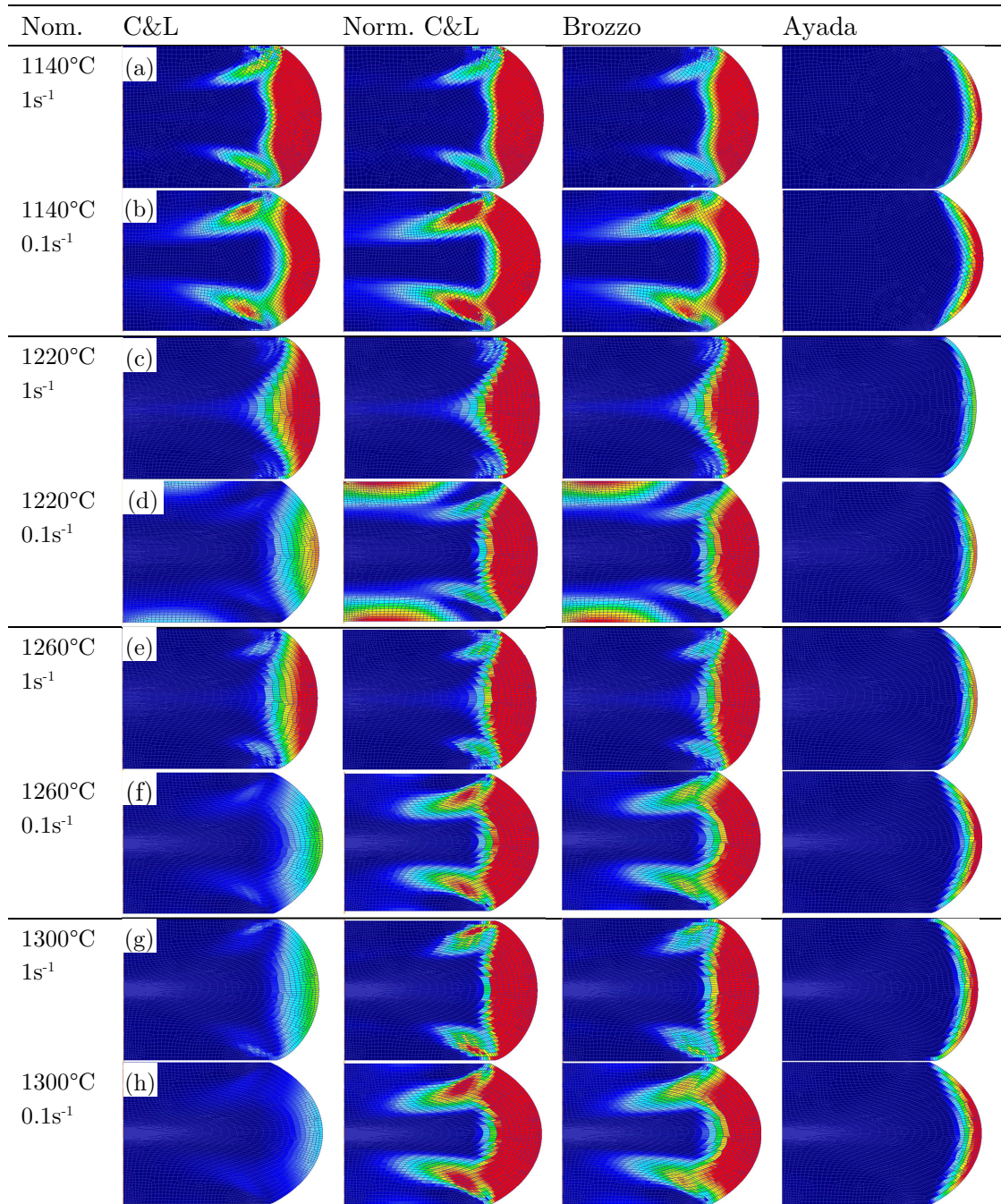
Figure 79: Damage parameter D during hot deformation with selected damage models (a) 1140°C, 1s⁻¹, (b) 1140°C, 0.1s⁻¹, (c) 1220°C, 1s⁻¹, (d) 1220°C, 0.1s⁻¹, (e) 1260°C, 1s⁻¹, (f) 1260°C, 0.1s⁻¹, (g) 1300°C, 1s⁻¹ and (h) 1300°C, 0.1s⁻¹.

4.3.4 Flow localisation model

Figures 80 show the distributions of m, γ' and α_{SJ} as calculated numerically from Eqs. 9, 25 and 29 in the deformed specimens. These results correspond to global deformation temperatures of 1140-1300°C, global strain rates of 0.1 and $1s^{-1}$ and a total strain of 0.9.

The m distribution shows highly positive values, which are localised in a transition zone and at the bulged area. Low m values are observed in the centres of the observed specimens. The m values increase with increasing temperature and decreasing strain rate.

The γ' is low in general close to the dead zone. The highest softening is obtained in the forging cross. By increasing the strain rate and decreasing temperature the deformed specimens show the tendency of high flow softening.

The positive α_{SJ} values are highly localised at the centres and at the edges. The lowest α_{SJ} values are located at the dead zones of the specimens and this tendency is present for all conditions. Generally, the high strain rates and low temperatures reveal higher strain rate sensitivity, flow softening and flow localisation values.

Figure 80: FE simulation results of m, γ and α parameter for the specimens deformed at (a) 1140°C, 1s^{-1}, (b) 1140°C, 0.1s^{-1}, (c) 1220°C, 1s^{-1}, (d) 1220°C, 0.1s^{-1}, (e) 1260°C, 1s^{-1}, (f) 1260°C, 0.1s^{-1}, (g) 1300°C, 1s^{-1} and (h) 1300°C, 0.1s^{-1}.

4.4 Summary of the results

The results of the thesis can be summed up as follows:

The **as-received** condition has shown a duplex structure consisting of γ_g grains, β_o phase, α_2/γ colonies and TiB precipitates.

Different heat treatments were applied: The phase distributions after *fast cycle* heat treatments were analysed. The phase quantification reveal that the lowest amount of β was obtained at the γ solvus temperature (1260°C) and at temperatures above and below $T\gamma$ at 1220°C an increment in the β amount was observed. Below the T_{eu} (1160°C) the β/β_o phase amount decreased again. The highest amount of the α_2/γ colonies were obtained above the T_γ. Phase fractions differences between edge and centre were observed due to the longitudinal temperature gradient along the specimens tested in the Gleeble® machine.

The **flow curves** of the three thermomechanical processes (slow cycle, fast cycle and isothermal) show similar tendencies. In general, large stress values are obtained by increasing the strain rate and decreasing the temperature and a maximal peak stress occurs at strains below 0.1. Softening at lower temperatures and steady flow stress at higher temperatures are characteristic of the flow curves.

For all three thermomechanical processes **peak stresses** were plotted as a function of temperature for different strain rates. A decrease in the strain rate and increase in temperature lead to lower values of peak stresses.

The **relative softening** values were also calculated. The *fast cycle* shows large softening at low strain rates and low temperatures and also at high temperatures and high to moderate strain rates. The *slow cycle* shows large softening values at low temperatures moderate to slow st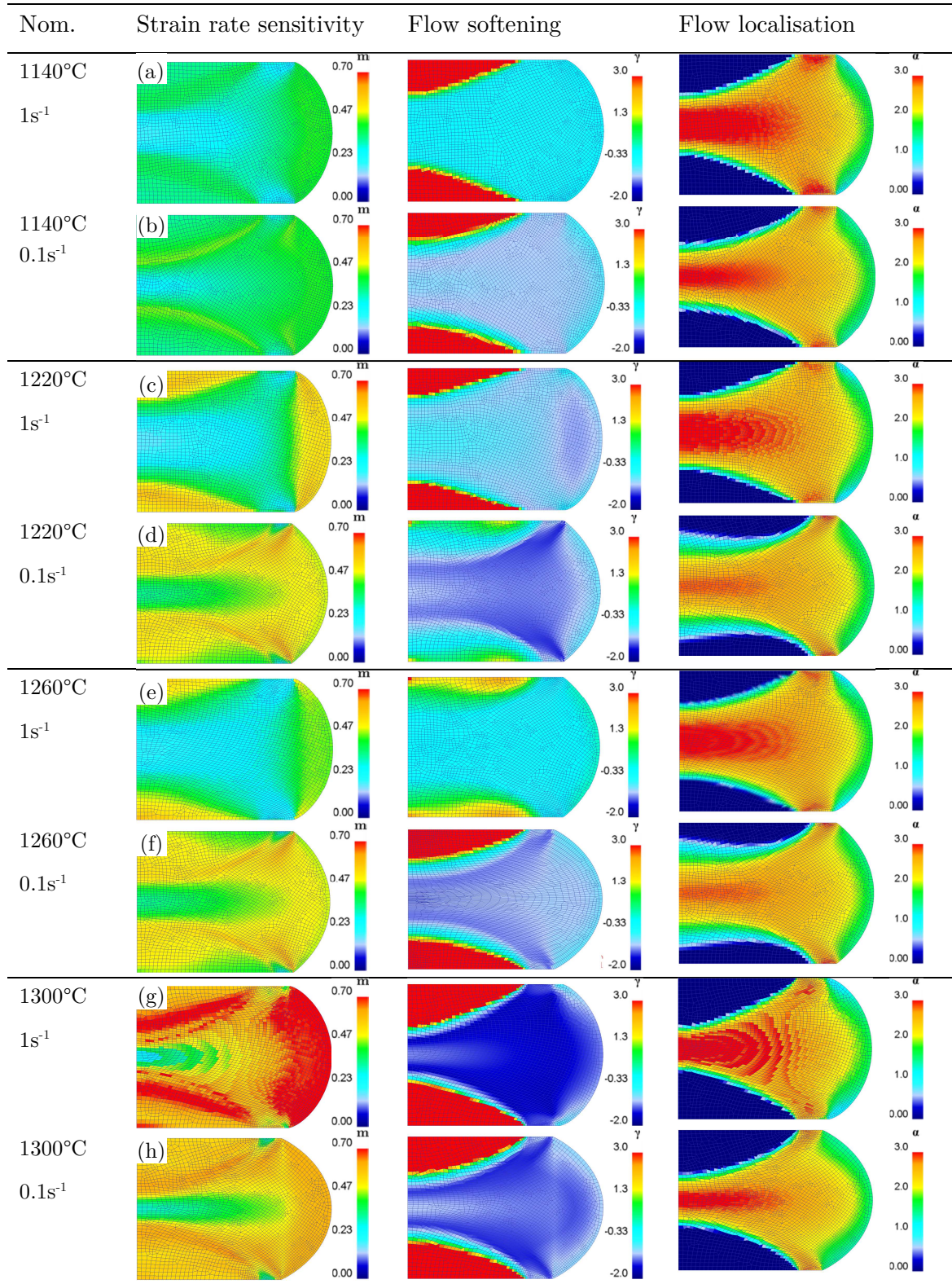rain rates. The high temperature range reveals also large softening values. The *isothermal cycle* shows large softening values at low temperatures moderate to slow strain rates and high temperature range at high strain rates.

The **microstructure after fast cycle deformation** shows a duplex microstructure for the specimen deformed at 1140°C and 1s⁻¹, which consists of α_2/γ colonies, γ_g and β_o phase surrounding the α_2/γ colonies. The γ_g has a smaller grain size in comparison to the heat treated condition. The microstructures at low temperatures (1140°C) reveal kinking of the α_2/γ lamellae. The specimen deformed at 1220°C and a strain rate of 1s⁻¹ shows a duplex microstructure and the γ_g grains are smaller compared to the samples deformed at 1140°C. By decreasing the strain rate to 0.005s⁻¹, the microstructure consists mainly of α_2/γ colonies with a low amount of the β_o phase. The specimens deformed at temperatures higher than 1220°C present a microstructure consisting on α_2/γ lamellae, β_o phase and small amounts of γ_g phase. At high temperatures (1300°C), no kinking of the lamellae was observed.

The **microstructure after slow cycle** for the specimen deformed at 1140°C, 1s⁻¹ reveals a microstructure consisting of α_2/γ lamellae with β_o and γ_g phases. By decreasing the strain rate to 0.005s⁻¹, a higher β_o fraction is observed. The specimen deformed at 1220°C and 1s⁻¹ shows a microstructure with α_2/γ colony with β_o phase and the γ phase. The γ phase that surrounds the α prior grain boundaries is not globular as at 1140°C. The specimen deformed at 1260°C

and $1s^{-1}$ reveals only α_2/γ colonies surrounded with β_o phase. Some low fraction of γ phase is primarily located within the β_o phase. The samples deformed at 1260°C and $0.005s^{-1}$ and 1300°C and $0.1s^{-1}$ show similar microstructural features. Precipitates rich in Mo, Nb and B, titanium niobium borides, were found nearly for all testing conditions.

Microdamage after deformation at 1140°C, $1s^{-1}$ for both, *fast and slow cycles*, is characterised by shear bands. Microcracks were observed for both thermal cycles, which spread mainly in translamellar direction over the microstructure. Locally, however, the crack pathway is influenced by the orientation of the colonies. The bulged areas show micro crack formation due to tensile stresses state during deformation. For both cycles pores were observed close to the Ti(Nb)B precipitates. For both cycles no damage could be observed at high temperatures above 1260°C. The EBSD investigations have shown that subgrains are formed mostly in the β_o and α_2 phases and HAGB's in the γ phase.

The **flow curves** of the material were **modelled** for the slow cycle condition using a TANH type model. It is observed that many modelled flow curves differ from the experimentally determined ones. The TANH model allows a good softening reproduction, but the hardening reproduction is not sufficient.

The **strain rate sensitivity** values were calculated for both thermal cycles and plot in the form of isoline maps as a function of the strain rat and the temperature. The *fast cycle* reveals that negative m values appear at temperatures below 1180°C and high strain rates, and at temperatures above 1200°C and low strain rates. On the other hand high m values occur at high strain rates. An increase in the strain causes the negative m area above 1200°C to increase. The *slow cycle* shows that negative m values occur at high strain rates and high m values appear at low strain rates at temperatures between 1200°C and 1300°C.

The **processing maps** based on efficiency of power dissipation after Prasad η_P and Murty and Rao η_{MR} and the instability models ξ, K or K_j were only calculated for the *slow cycle*. The processing maps calculated at a strain of 0.4 shows that the instability criterion ξ shows negative values at low temperatures: 1140-1240°C for low strain rates. At low strain rates the η_P reveal high values. The temperatures from 1300°C to 1340°C combined with high strain rates also show negative ξ values. The predictions by K show the same tendency as ξ. K_J is negative at low temperatures 1140-1200°C and strain rates of 1-$0.1s^{-1}$. Furthermore, negative K_J are obtained for the strain rate $0.005s^{-1}$ at 1220-1240°C and the temperatures at 1300-1340°C and high strain rates. The processing maps calculated at a strain of 0.8 for the slow cycle reveal that at temperatures between 1140-1200°C and at strain rates between 1-$0.005s^{-1}$ low η_P, ξ, K and K_j occur. At temperatures above 1300°C even negative ξ, K and K_j values appear. Furthermore flow localisation and flow softening maps have been calculated for the slow cycle. The flow localisation is predicted for $\alpha_{SJ}>3$ and $\gamma'<0$.

FEM simulations were used to calculate the temperature, effective strain and effective stress distributions developed within the hot deformed specimens at different testing conditions. It could be observed for all specimens that the distributions are not homogeneous due to the barrelling and heating methods. Maximum temperatures are localised in the centre of the specimens. The largest values of strain are achieved at the centre of deformed samples. High strains are furthermore localised at the bulge between specimen and loading tools. The stress

distributions show high values at the contact area between specimen and loading tool and at the edges of the deformed specimens.

The **FE simulations** were carried out using **experimental and modelled flow stresses** and the specimens simulated with modelled flow curves show in general higher stresses. However, the qualitative localisation of temperature, strain and stress distributions in the deformed specimens are comparable with experimental and modelled flow stresses.

The **continuum mechanic macromechanical damage models** show large damage values at the bulge region and low values at the centres. All used models show the same tendency.

The **m, γ' and α_{SJ} models** implemented into FEM were calculated for different processing conditions. The m distribution shows highly positive values, which are localised in a transition zone and at the bulged area. In general low m values were observed in the centres of the observed specimens. The m values increase with increasing temperature and decreasing strain rate. The γ' is low in general close to the dead zone. The highest softening is obtained in the forging cross. By increasing the strain rate and decreasing temperature the deformed specimens show the tendency of high flow softening. The positive α_{SJ} values are highly localised at the centres and at the edges. The lowest α_{SJ} values are located at the dead zones of the specimens and this tendency is present for all conditions. Generally, the high strain rates and low temperatures reveal higher strain rate sensitivity, flow softening and flow localisation values.

5 Discussion

The objective of the present study is to describe the deformation and damage mechanisms that occur in the TiAl alloys as a function of deformation parameters, as well as to determine flow localisation occurrence.

5.1 Material behaviour under thermomechanical processing

5.1.1 Flow behaviour

The flow behaviour of the analysed alloy for both thermal cycles is strongly influenced by the process parameters (strain, strain rate and temperature) as well as by the history of the material.

Based on the curve shape it can be seen that strain hardening and thermally activated softening processes take place. At small strains the material is hardened due to dislocation formation. However, as soon as a sufficient percentage of dislocations is reached and the temperature is high enough, softening mechanisms are activated. In general dynamic softening of the material is correlated to dynamic restoration processes, phase transformations, damage or a combination of both. The last regime of the flow curves is the steady state condition, which is the equilibrium between work hardening and softening. All obtained flow curves show a single peak for both cycles. The presence of the bcc β phase has a strong influence on the flow stresses. At 1260°C large peak stresses are observed due to the minimum β phase fraction at this temperature (5vol.-% from heat treatment data). The softening map shows relatively low values for these two flow curves in contrast to the other curves. It is known from literature [165] that the bcc β phase is easily deformable at elevated temperatures due to sufficient independent slip systems.

Besides the deformation temperature and strain rate other process parameters such as heating rate, prior temperature and holding time have an influence on the initial microstructure, which in turn influences the flow behaviour of the material. In general the flow stresses of the material submitted to the *fast cycle* are higher in comparison to the ones of the *slow cycle* (see Figure 81). This can be attributed to the non-equilibrium phase condition due to the higher heating rate and short holding time at the peak temperature. The expected initial microstructure before deformation is different between *fast cycle* and *slow cycle* and therefore the starting flow stresses are higher in the *fast cycle*. Furthermore, the softening of the flow curves of the material submitted to the *fast cycle* is in general higher than in the *slow cycle*. At large strains, flow stresses reach similar values.
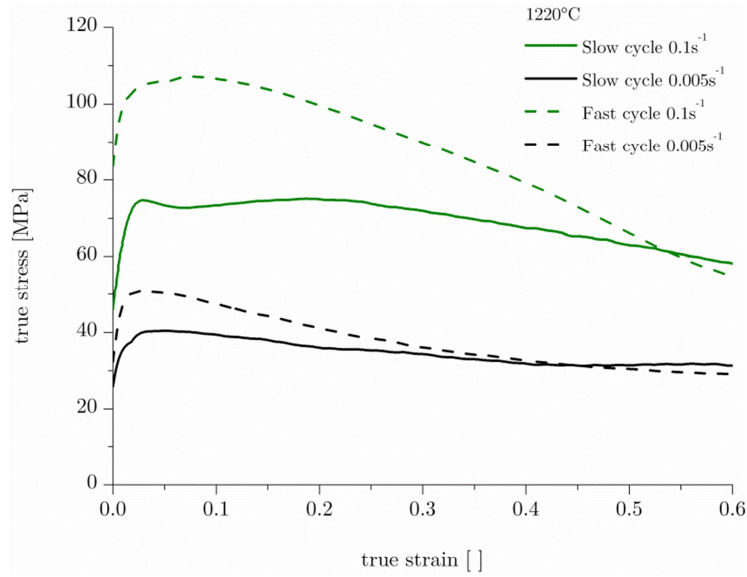
Figure 81: Comparison of flow curves of the *fast-* and *slow cycle.*

Figure 82 (a) shows that the microstructure of the specimen heat treated at 1140°C is characterised by a high amount of α_2/γ colonies and γ_g phase. α as well as γ phases have less independent slip systems, which make them difficult to deform. On the other hand the microstructure of the deformed specimen reveals a different microstructure with higher β_o and γ_g amounts (see Figure 82 (b)).

Figure 82 (c) shows the microstructure of the specimen deformed at 1140°C and 1s^{-1} in the *slow cycle*, which reveals more β_o than Figures 82 (a) and (b). The microstructure of the specimen heat treated reveals no γ with globular shape in contrast to the deformed specimens. As can be seen in the micrographs of the deformed specimens, the DRX grade is higher in the specimen deformed submitted to the *fast cycle,* and this may be attributed to two reasons. Firstly, the long holding time at peak temperature under the *slow cycle* may cause a coarsening of the phases and therefore there are less nucleation sites for DRX in the material. Secondly, during deformation a certain amount of energy is stored, which can cause static recrystallisation during the cooling procedure, significantly slower in the *fast cycle.* In the *slow cycle* the cooling rate is higher, which leads to a smaller RX grade.
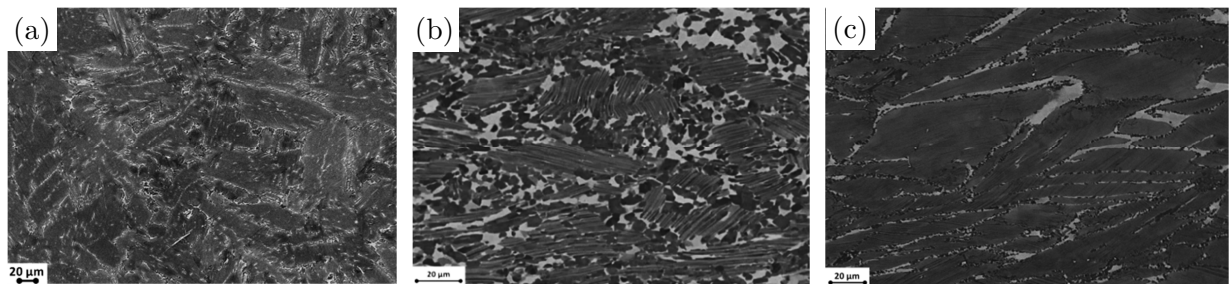
Figure 82: Comparison of microstructures of specimens (a) heat treated by means of the *fast cycle*, (b) deformed at 1140°C, 1s^{-1}, *fast cycle* (c) deformed at 1140°C, 1s^{-1}, *slow cycle*, with (b) and (c) up to a true strain of 0.6.

Phase transformation temperatures are shifted to higher temperatures due to the higher heating rates, also affecting the deformation behaviour. Furthermore, a longer holding time and slower heating rate favour grain growth. The grain coarsening has a strong influence on the DRX, SRX and dynamic phase transformation behaviour of the material.

After deformation specimens were cooled down. Both cycles were carried out with different cooling rates. The *fast cycle* is characterised by a slower cooling rate (2.5°C/s) than the *slow* (10°C/s) ones. As can be seen in Figure 83, the slower cooling rate for the same deformation parameters causes thicker α_2/γ colonies and may be is the reason for SRX of γ.

The flow curves measured by means of the *slow cycle* reveal relatively low softening values compared to the *fast cycle*. Both cycles reveal large m values at low temperatures and low strain rates due to the observed dDRX of the γ phase. In contrast to the *fast cycle* the *slow cycle* reveals less damage at higher temperatures, due to the sufficient restoration processes in the β and α phases. The strain rate sensitivity maps show negative m values at the lowest temperature and the highest strain rate for both cycles at a global strain of 0.6. This negative m value is due to flow localisation and shear band formation.

Negative m values for the *fast cycle* are predicted for temperatures above 1200°C and low strain rates. This negative m value can be attributed to dynamic phase transformation, because the phase fraction and morphology are completely different compared to the specimen heat treated and deformed at the higher strain rate.

Figure 83 shows a comparison of the heat treated and deformed specimens at 1220°C and strain rates of $1s^{-1}$ and $0.005s^{-1}$. The micrograph of the specimen deformed at 1220°C and $0.005s^{-1}$ shows the lowest amount of the β_o phase compared to the microstructure of the other two specimens. The γ phase is not globular in the specimen deformed at 1220°C and $0.005s^{-1}$, as shown in Figure 83 (c).

(a) β_o= 16.85vol%, γ_g= 47.35%vol, $\alpha_2+\gamma$ colony= 35.8%vol	(b) β_o= 10.2vol%, γ_g= 54.9%vol, $\alpha_2+\gamma$ colony= 34.9%vol	(c) β_o= 7.8vol%, γ_g= 49.6%vol, $\alpha_2+\gamma$ colony= 42.6%vol
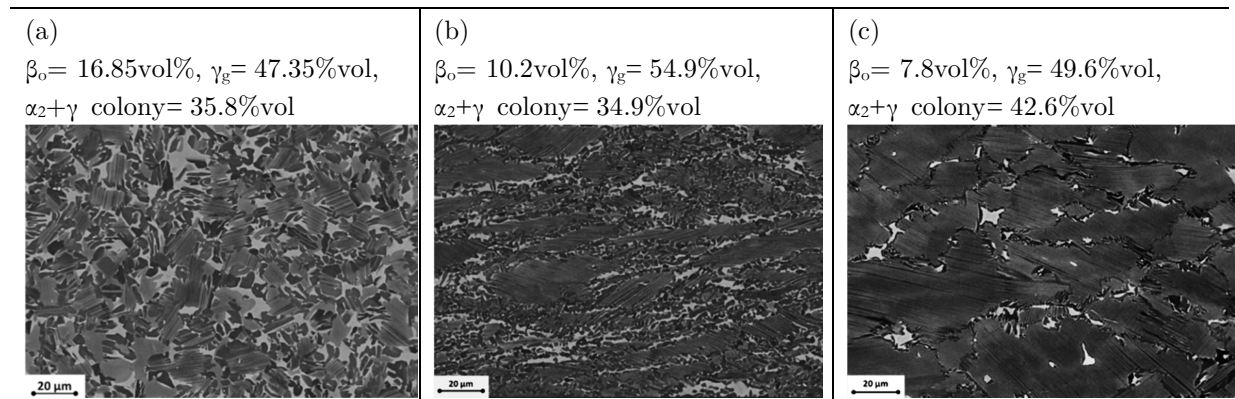
Figure 83: Comparison of microstructures of specimens of the *fast cycle* (a) heat treated, and deformed at (b) 1220°C and $1s^{-1}$ and (c) 1220°C, $0.005s^{-1}$ to a true strain of 0.6 after *fast cycle*.

In general DRV does not occur in the γ phase due to its low SFE (60-90 mJ/m^2) [130]. In the low temperature range the subgrains have formed inside the β and α phases as a result of DRV. The influence of temperature and strain rate on the LAGB fraction is shown in Figure 84. Higher temperatures and lower strain rates lead to the formation of a higher amount of subgrains in the α and β phases. The dominant restoration mechanism in both phases is DRV

in the temperature range from 1140-1260°C. The strain rate sensitivity maps reveal high m values for 1260°C, which indicates highly activated thermal processes.
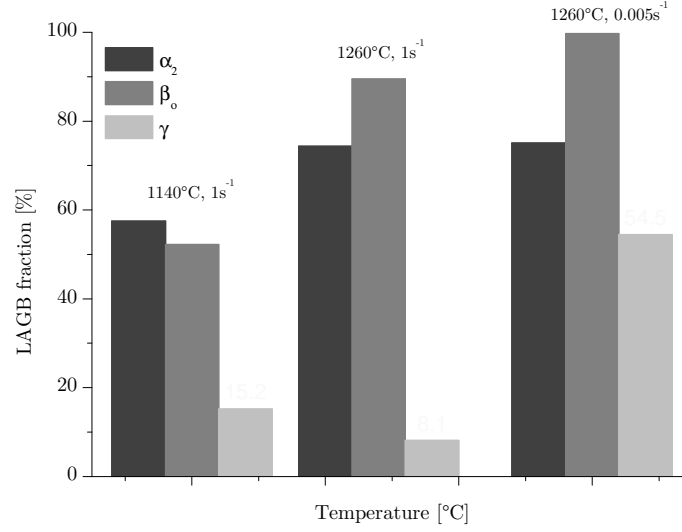
Figure 84: LAGB fraction of the three phases in the specimens deformed (*slow cycle*) at 1140°C, 1s^{-1}, 1260°C, 1s^{-1} and 1260°C, 0.005s^{-1}.

5.1.2 Microstructure evolution

Hot deformation modifies the microstructure of the as-received condition as a function of strain, strain rate and temperature. The as-received condition reveals a homogenous duplex microstructure, consisting of globular γ grains, β$_o$ phase and α$_2$/γ colonies. The microstructure evolution for the *slow cycle* is described below.

The specimen deformed at 1140°C and a strain rate of 1s^{-1} shows a duplex microstructure consisting of γ$_g$ grains, α$_2$/γ colonies and β grains. At this temperature DRX occurs in γ and DRV in α and β. After hot deformation, the α$_2$/γ colonies are oriented parallel to the compression direction. Normally, the lamellar colonies cannot completely break down by thermal and mechanical processing up to the tested strains. After heat treatment remnant colonies are difficult to deform.

The specimens deformed at 1220°C show that colonies are perpendicular to the compression direction, which means that the α or α$_2$ phase has to deform in hardest slip mode. The colonies can be easily deformed via shear parallel to the interfacial planes when they are oriented 45° to the compression direction. The β phase appears elongated at high strain rates, while equiaxed β subgrains are formed at low strain rates. The specimens deformed at lower strain rates reveal a higher degree of DRV, which causes equiaxed β subgrains. After deformation above 1260°C small γ$_g$ fractions are observed due to the high cooling rate, hindering a complete formation of further γ$_g$. These small γ grains are precipitated in the β phase, which is necessary to prevent uncontrolled growth of the α phase [166]. The obtained microstructures above the γ solvus temperature are similar to each other, consisting primarily of α colonies surrounded by β phase within fewer fractions of γ grains.

5.1.3 Softening

Various factors can cause dynamic softening of the alloy such as DRX, phase transformation, crack formation and deformation heating. Thus the flow softening of the analysed alloy is a complex combination of many phenomena. The softening behaviour for the *slow cycle* is described as follows.

a) Flow softening due to DRX

The γ phase has dynamically recrystallised (DRX) in the whole analysed range of strain rates. Lower strain rates caused a larger grade of DRX. The KAM maps of the γ phase with HAGB marked by grey lines, are shown in Figure 85. KAM measurements confirm that the γ phase present no misorientation after deformation. Either the γ phase has dynamically recrystallised or it has not undergone DRV (Figure 85).

The m and η maps reveal high m and η values indicating thermally activated processes such as dDRX. The m map shows a negative m value together with the highest strain rate. This negative m value is due to the high grade of damage even though the γ_g phase has dynamically recrystallised. The SFE values of β and α_2 phases are not exactly known, but they are assumed to be high because of their similarity to the β phase in Ti alloys and the α_2 phase in Ti$_3$Al alloys [4]. It was found that kinked colonies are preferred sites for nucleation of new grains, as confirmed by et al. [167]. In some γ lamellae a few LAGBs can be seen, which indicates that an increase in the strain will cause DRX to carry on in this newly formed grains. The low strain rates region reveal low η_P and m values at low temperatures compared to higher strain rates.
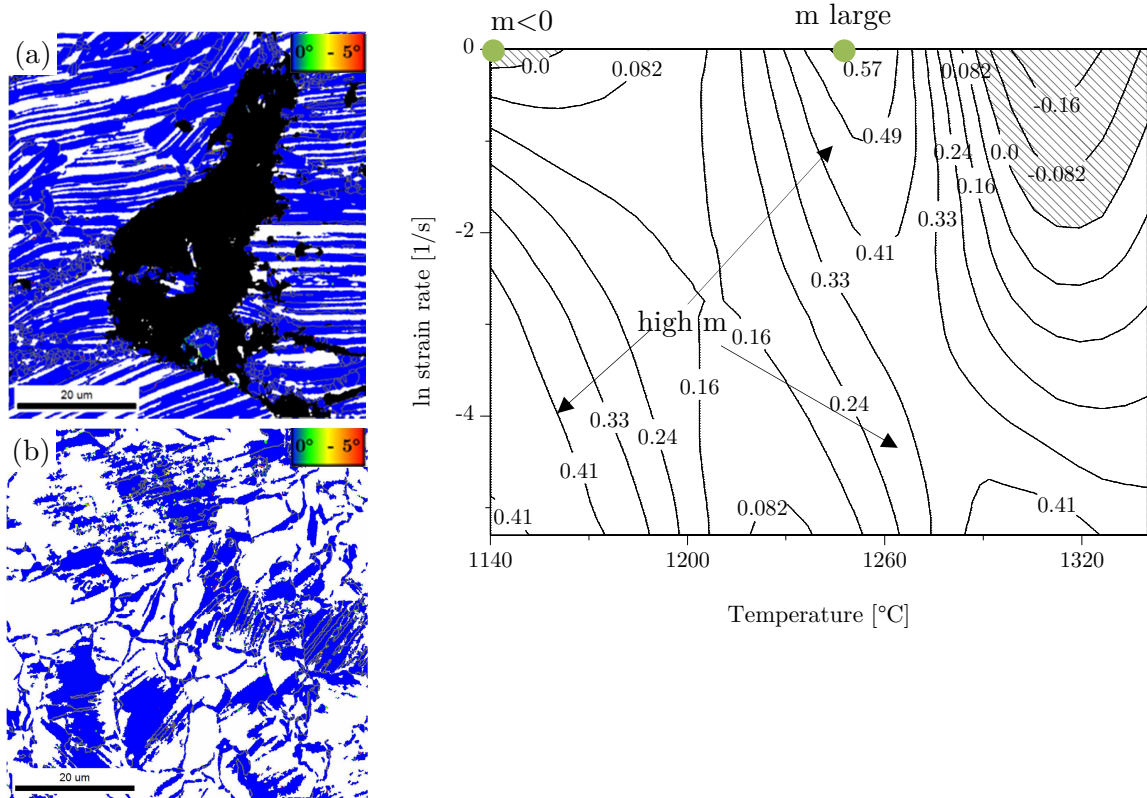
Figure 85: KAM maps of the γ phase in the specimens deformed at (a) 1140°C, 1s^{-1} and (b) 1260°C, 1s^{-1} with the correlating strain rate sensitivity map. HAGB are marked by grey lines.

A comparison of the total kernel average misorientation distributions of the as-received condition, at 1140°C and 1260°C at a strain rate of 1s⁻¹ are shown in Figure 86. Black lines correspond to the 1ˢᵗ nearest neighbour, red lined to the 5ᵗʰ nearest neighbour and 10ᵗʰ nearest neighbour is represented with green lines. The KAM distributions for the different neighbour relations in the specimens show similar distributions for the same testing condition but the same tendency. Deformation shifts the KAM peaks to higher misorientation degrees. The non-deformed material contains a high frequency of 0-1° misorientation angles.
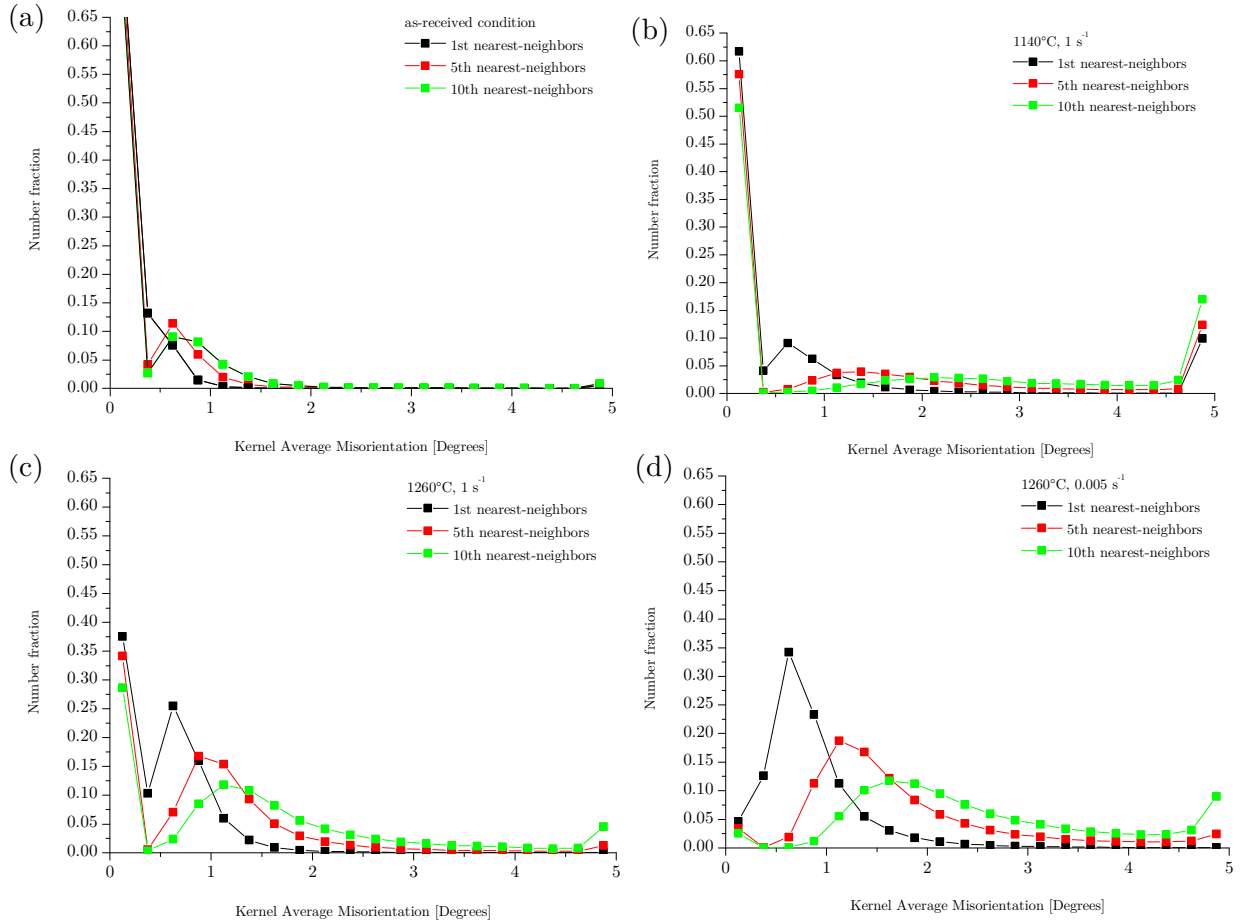
Figure 86: Comparison of total kernel average misorientation profiles (a) as-received condition, deformed specimens at (b) 1140°C, 1s⁻¹, (c) 1260°C, 1s⁻¹ and (d) 1260°C, 0.005s⁻¹.

b) Flow softening due to kinking and fragmentation

At low temperatures (<1180°C) kinking or bending of α_2/γ lamellae along to the compression direction causes further flow softening. This inhomogeneous microstructure is attributed to the plastic anisotropy on lamellar colonies. Inui et al. [168] have shown that the yield stress of lamellar colonies strongly depends on the orientation angle between lamellar boundaries and compression direction. The kinking of lamellae begins at low strain, as can be seen in Figure 52 (b). Later, DRX is induced. At higher strain rates the fraction of kinked lamellae is higher compared to lower strain rates. In many kinked lamellar colonies globularization occurs. At higher temperatures small amounts of β phase, are formed within the colonies, which contributes to the deformation behaviour of titanium aluminides as suggested by Li et al. [169].

c) Flow softening due to damage

Damage is a further process that accounts for the decrement of the flow stress. The observed kinds of damage are micro pores, cracks and wedge cracks. Macro cracks occur mainly at the bulged area of the specimens due to tensile stresses. During compression tensile stress components appear at the bulge as a result of friction, temperature gradient and geometry. At higher temperatures the intensity for macrocrack formation decreases.

Hot deformation at high strain rates and low temperatures produced macro cracks formed in colonies parallel to the compression direction. Many small cracks that have formed parallel to the main crack release the high stress concentration. It is observed that different oriented α_2/γ colonies can act as an obstacle for crack propagation. The observed slip planes are aligned along the main compression direction. The path of cracks of many bridged wedge cracks differs substantially from the known propagation direction. The cracks path is mainly translamellar across the microstructure, but also in some specimens a mixture of interlamellar and intralamellar was observed (see Figure 87). Cracks are hindered mainly by the γ phase. At low strain rates many scientists suggest [76] that wedge cracks are commonly initiated at grain boundaries and triple points, where the stresses cannot be released by matrix slip, grain boundary migration or grain boundary diffusion. At higher strain rates wedge cracks are mainly formed due to the interaction of slip bands with grain boundaries [7], and a lack in the restoration mechanism. Mostly the cracks are stopped in the γ phase, whereby the crack propagation is less hindered in the brittle α_2 phase.
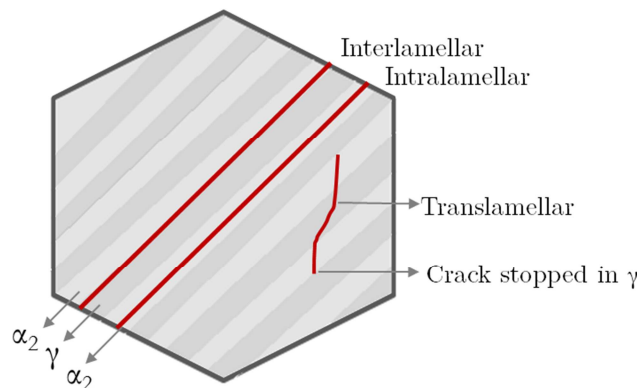
Figure 87: Crack paths: translamellar, interlamellar, intralamellar.

Wedge cracks are the main damage mechanism during deformation in the studied TNM alloy. Most of them are parallel to the compression direction and initiated at the prior α grain boundaries. The experiments reveal that a high amount of wedge cracks are already formed at very low strains (0.2), as can be seen in Figure 88 (a). The wedge cracks are marked by rectangles. Their amount and size increases with increasing strain, as shown in Figure 88 (b). The wedge cracks at grain boundaries are caused by stress concentrations. At higher strain rates the stress is released by formation of wedge cracks [170].
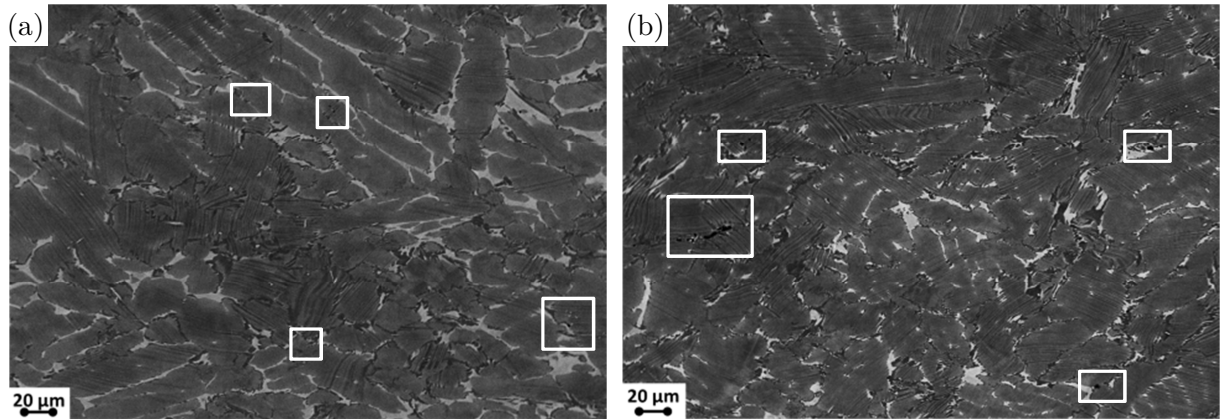
Figure 88: SEM micrographs of the deformed specimen at 1140°C with a strain rate of $1s^{-1}$ up to true strains of (a) ε=0.2 and (b) ε=0.4.

In some deformed specimens it is observed that Ti(Mo,Nb)B precipitates promote damage. Some pores and wedge cracks appear close to the precipitates enriched with Nb, B and Mo due to the strain misfit between the precipitates and the matrix. When the material starts to deform the dislocations accumulate at TiB/matrix boundaries. This high stress concentration is released as pores and cracks.

d) Flow softening due to deformation heating

Flow stress decreases as temperature increases due to self-heating, a phenomenon that is more evident at higher strain rates. The flow stresses corrected to self-heating and the measured ones are compared for the temperature of 1180°C in Figure 89.

At high strain rates the corrected flow curves show higher stress levels. At low strain rates, the difference in the stresses is negligible, because the deformation heating is dissipated into the dies and the environment. The corrected flow curve crosses the measured flow curve in the specimen deformed at 1180°C and $0.5s^{-1}$. This behaviour is due to the methodology used, because for the temperature correction the measured **ΔT** values were considered, which were positive and negative in this case. The **ΔT** values were negative due to the slow temperature control of the Gleeble and the overheating caused a decrement in flow stress.
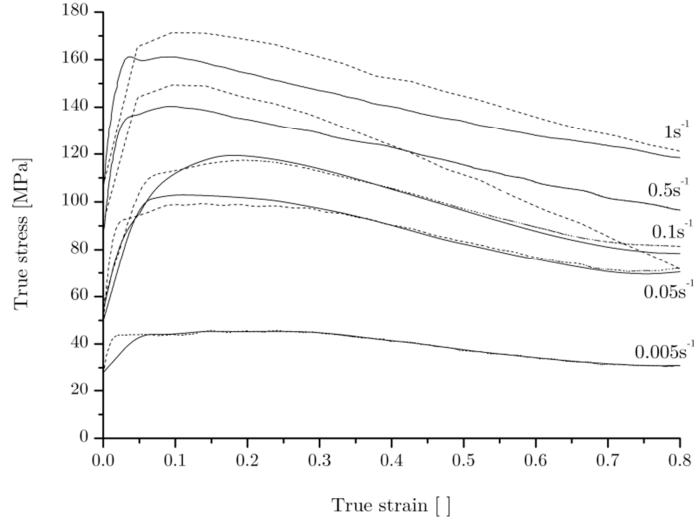
Figure 89: Measured (complete lines) and adiabatic corrected (dashed lines) flow curves of the *slow cycle* for the temperature 1180°C and several strain rates.

The relative softening of the non-corrected σ and corrected flow stresses σ_c due to self-heating are calculated for a total strain of 0.8. High strain rates and low temperatures show in general high values of softening related to self-heating (corrected vs not corrected). The influence of self-heating on softening can be seen in Table 8.

Table 8: Flow softening of the measured and the temperature corrected flow curves.

Temperature [°C]	Strain rate [s⁻¹]	Relative softening corr. $\dfrac{\sigma_{cpeak} - \sigma_{c0.8}}{\sigma_{cpeak}}$	Relative softening $\dfrac{\sigma_{peak} - \sigma_{0.8}}{\sigma_{peak}}$
1140	1	0.39	0.44
1140	0.5	0.24	0.30
1140	0.1	0.49	0.52
1140	0.05	0.46	0.47
1140	0.005	0.71	0.71
1180	1	0.26	0.29
1180	0.5	0.31	0.51
1180	0.1	0.34	0.35
1180	0.05	0.31	0.32
1180	0.005	0.33	0.33

Localisation of plastic flow in form of shear bands has been observed after deformation at high strain rates and low temperatures for both heating cycles. At these testing conditions the highest values of temperature increment (ΔT nearly 20°C) were measured at the surface of the sample. The macrograph in Figure 56 (a) reveals that the shear band extends through the whole deformed specimen.

5.2 Macroscopic damage predictions

During compression tests tensile stress components resulting from friction, temperature gradient and geometry appear at the bulge zones of the samples. The continuous models predict large D values at the bulge of the deformed specimens, validated for strain rates 1 s^{-1} and 0.1s^{-1} and a temperature range of 1140°C to 1300°C. The macroscopic damage prediction is in good agreement with the experimentally determined damage. The applied macro-mechanical damage models have shown large damage at the experimentally determined fracture site. Finally, the damage parameters do not predict damage in the centre of the samples. This is not in agreement with the experimental observations, because adiabatic shear bands or other kind of damage are observed throughout the sample. The disadvantage of those models are that they are based on continuum mechanics and do not consider the microstructure. Therefore the damage values were obtained without considering physical phenomena and the interaction between the mechanical behavior and damage state. The material is regarded as homogeneous and therefore secondary phases, precipitates were considered as distributed homogeneously. The anisotropy effect and non-equilibrium condition of the material are as well not considered. Therefore those models only consider the actual stress conditions of the material. It is a risk to establish damage function as an increasing function of triaxiality.

The values predicted by the macromechanical damage models have to be considered from a qualitative point of view, because the critical damage value D_c is not measured and therefore not considered. As known, damage occurs when the damage factor achieves the critical damage value D_c. However, it is sufficient to gain an overall estimation.

5.3 Process parameter distribution

In this sub-chapter the influence of the process parameter distributions on the flow localisation and macro-scale damage are discussed.

Figure 90 shows the evolution of the flow localisation as a function of temperature, strain rate and strain at the centre of the specimens deformed at 1140°C (red) and 1260°C (green) and strain rates of 1s^{-1}. The strain increases by increasing deformation for both specimens, as shown in Figure 90 (a). The temperature increases due to the strain rate (see Figure 90 (b)). The strain rate also increases with the deformation, which means that the material is deformed faster at every deformation step (Figure 90 (c)).

At small deformations both specimens show large negative α_{SJ} values. It is visible that α_{SJ} increases with strain, strain rate and temperature. Larger positive α_{SJ} values are obtained for 1140°C than for 1260°C (see Figure 90 (d)). This is in good agreement with the shear bands observed at 1140°C. At higher temperatures no flow localisation was observed in the micrographs. Self-heating produces an increment of temperature at higher strain rates. Therefore, the normalised flow softening parameter γ' shows higher softening in the forging cross due to both, strain and temperature softening (see Figure 80). The lowest softening is obtained at the contact area between anvils and specimen. This is in good agreement with the measurements, because the lowest deformation took place there, which is verified by the FEM strain distribution profiles (see Figure 77).

High flow localisation is predicted in the centre of the specimens, because a large softening occurred due to the combination of restoration mechanisms and damage. The deformed specimens always show positive m values, which are high at high temperatures.
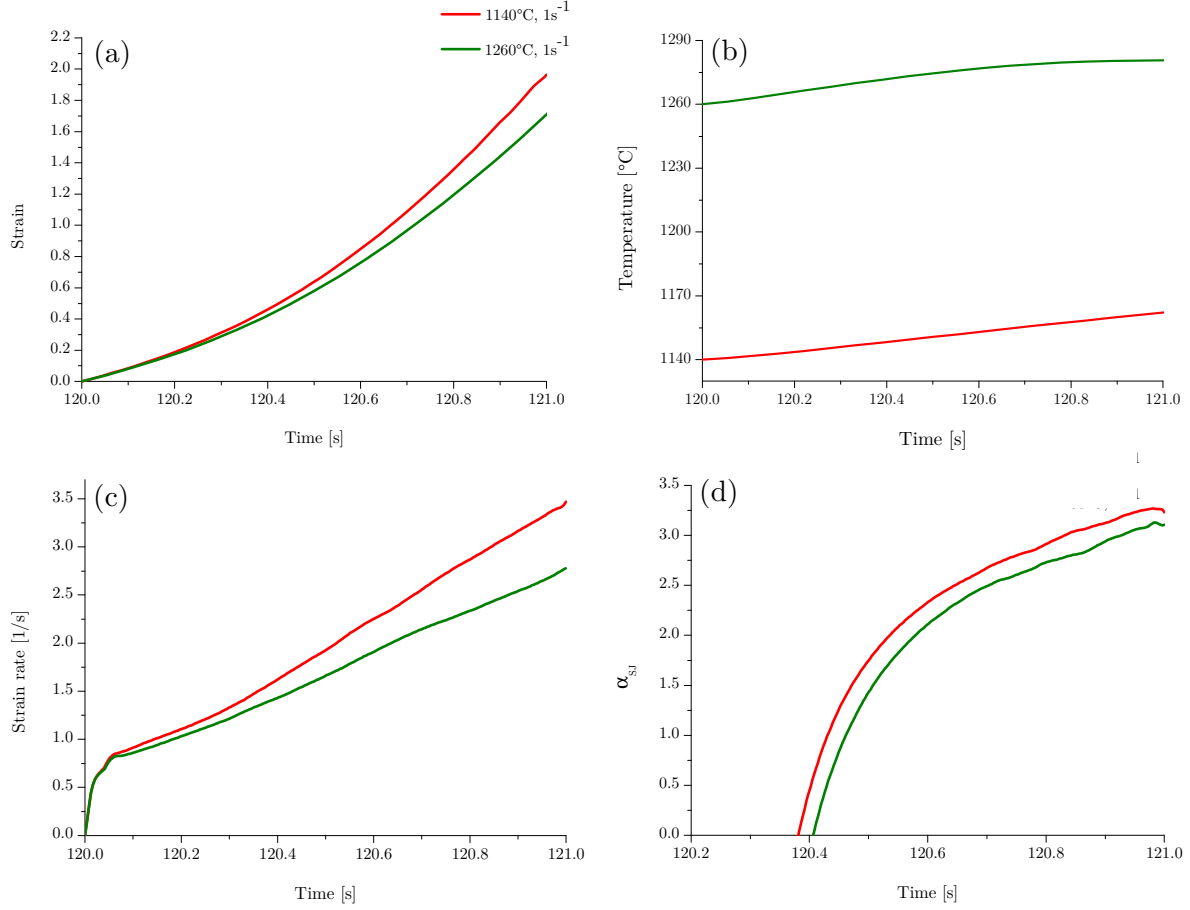
Figure 90: Output FEM analysis distributions of (a) strain, (b) temperature, (c) strain rate, and (d) flow localisation α_{SJ} vs time for the specimens deformed at 1140°C and strain rate 1s[-1] marked with red line and 1260°C and strain rate 1s[-1] indicated by green line.

5.4 Processing windows

5.4.1 Instability parameter

The instability criteria based on DMM. The idea of continuum mechanic basic approaches is that the material is treated as continuum and therefore the defects such as pores, precipitates or secondary phases are accepted as homogeneously distributed within the material. These criteria can be used if the material is homogeneous, and strain and temperature are constant. The η_P, m and α_{SJ} were calculated for the TiAl alloy containing Nb, B and Mo enriched particles. The material does not exhibit ideal plastic flow and is far from the phase equilibrium.

The dissipation efficiency of Prasad is interpretable as m, because $\eta_P = 2m/(m+1)$ with respect to ξ, it was observed that sometimes at lower strains larger instability regions than at higher strains are predicted. This would mean that when the instabilities are once nucleated they are removed by further deformation. The prediction of instability at higher strains do

not involve instabilities introduced at lower strains [171]. The predictions by the other instability parameters such as K and K_j are also not in good agreement with the experimental observations.

Negative m values can be obtained, when the material undergoes strong flow localisation, large damage or dynamic phase transformation (see Figure 91). High flow localisation can be manifested by regions where the strain contributes to the global strain, followed by a drop in the flow stress. The result is that the measured flow curves show lower flow stress at higher strain rates due to adiabatic shear bands.
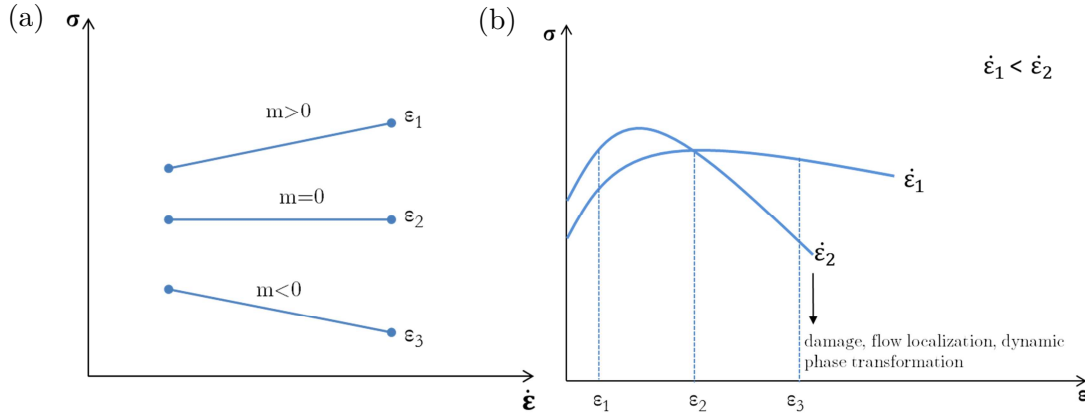
Figure 91: Scheme of the strain rate sensitivity behaviour for several strain rates and flow curves with different softening processes.

The parameter α_{SJ} can be interpreted as flow localisation generally when it is positive and in particular for TiAl alloys when it is larger than 3. The parameter α_{SJ} predicts flow localisation at low temperatures and high to moderate strain rates, producing adiabatic shear bands and brittle cracking. However, microstructural observations have revealed that also restoration processes such as DRX in γ and DRV in β and α_2 occurred. Thereby it can be concluded that the restoration processes are not enough to avoid damage. Both, large thermal and strain softening combined with low restoration result in positive α_{SJ}. Flow localisation induces shear bands and wedge cracks. At high strain rates, stresses cannot be sufficiently reduced by diffusion controlled deformation processes such as recovery and recrystallisation, and this leads to low m values. Previous studies confirm these observations [172,173]. Large m values and negative α_{SJ} are observed at low temperatures and low strain rates. The α_{SJ} parameter predicts better instabilities in contrast to the instability models based on DMM. It should be mentioned that α_{SJ} is not thermodynamically based, but rather mechanically. The α_{SJ} is calculated based on γ' and strain rate sensitivity m. γ' consists of the strain dependent term which is negative in the case of flow softening, and a temperature dependent one, which is negative due to thermal softening. $\gamma'<0$ means softening due to restoration processes and $\gamma'<-1$ predicts instabilities. Furthermore, m>0 and $\alpha_{SJ}>0$ means flow localisation. Semiatin and Jonas [87] have reported based on microstructural observations that for titanium alloys unstable flow occurs when $\alpha_{SJ}>5$. In a more general case, flow instabilities are predicted when α_{SJ} is positive. In the case of TiAl, there is still no stipulated value that should be overcome to obtain failure.

As known from measurements and FE simulations temperature and strain are not constant. Therefore, $\lambda = \int_{t_0}^{t} \alpha_{SJ}\, \dot{\varepsilon}\, dt$ should be used, which takes the history of the deformation into account. Positive λ values are indicating flow localisation, which is increasing with strain with respect to the deformation history of the material. Figure 92 shows the flow localisation parameter λ distributions after the deformation at 1140°C and 1s⁻¹ and 0.1s⁻¹. The specimen deformed at 1140°C and 1s⁻¹ shows larger λ values compared to the slower strain rate.
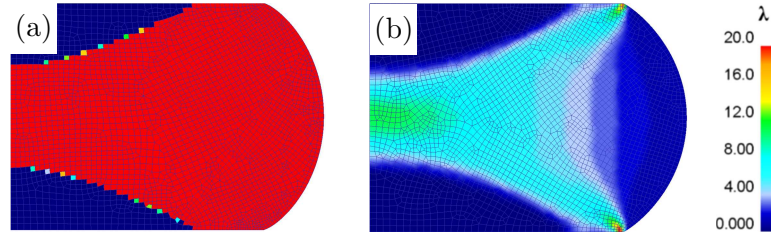
Figure 92: Flow localisation parameter λ distributions after deformation at 1140°C (a) 1s⁻¹ and (b) 0.1s⁻¹.

Is it possible to further interpret the strain rate sensitivity m in terms of microstructure? Since thermally activated dynamic processes are diffusion controlled, they need time. Therefore is given during deformation by their strain rate. Low m values indicate that the occurred processes are not strongly dependent on the strain rate or, in other words, not diffusion controlled [174]. At lower temperatures and strain rates DRX was not enough to avoid damage.

If γ'<0 and m<0 then α_{SJ}>0 is indicating wrongly stable flow behaviour. Therefore γ', m and α_{SJ} should be investigated separately and the microstructure should be investigated in detail. In three cases m can be negative as already mentioned, when flow localisation, dynamic phase transformation or damage occurs. In this study it can be concluded that α_{SJ} >3 indicating high flow localisation while γ'<0 predicts softening. Table 9 summarises softening, strain rate sensitivity and as well as their flow localisation and their physical interpretation. In this table negative strain rate sensitivity values are not considered.

Table 9: Softening, strain rate sensitivity and flow localisation and their physical interpretation

γ'	m	α_{SJ}	Hot deformation behaviour interpretation
<-1	small	>3	Flow localisation, low restoration lead to localised damage. Shear bands and abrupt changes in the microstructure, transition zones
<0	large	>0	No flow localisation, some softening due to restoration mechanisms
>0	small	<3	Stable microstructure and no instabilities
>1	large	<0	Stable microstructure and no instabilities

It can be concluded that general damage estimation of the material under different conditions can be gained by the flow localisation parameter α_{SJ}, which is based on semiempirical approaches. Low and high α_{SJ} should be verified by microstructural investigations. The strain rate sensitivity parameter can be used to describe the thermally activated processes such as recovery, recrystallisation, and phase transformations. However, it does not allow a distinction between the different thermally activated processes. The microstructural investigations by LOM, SEM and EBSD have verified the predictions by α_{SJ} and m. The DMM and the instability parameters should not be applied in future because of the lack of instability predictions due to wrong physical base. The dissipation efficiency parameter η_P is closely related to m and therefore it is sufficient to use only m.

5.4.2 Microstructural and damage map

Figure 93 shows the overlapped strain rate sensitivity m, microstructural and damage maps based on experimental characterisations. The colour black is indicating small m values, while white colour is attributed to large m values.

Low temperatures and high strain rates are characterised by high self-heating that provokes adiabatic shear bands. The adiabatic heating effect decreases with increasing temperature and decreasing strain rate. At this area small m values are observed. At temperatures below the α ordering reaction, deformation bands and kinked lamellae are observed. The sizes of wedge cracks and pores increase with increasing strain. The microstructures revealed that at temperatures below the γ solvus temperature the dynamic restoration mechanisms that appear are dDRX in γ and DRV in α or β. Therefore, lower temperatures and strain rates show large m values due to the high degree of DRX.

Above the γ solvus temperature no wedge cracks are observed. The predicted small m values at higher temperatures and strain rates are not in good agreement with the experimental observations. In this area a stable microstructure is observed.

Higher temperatures are characterised by the restoration mechanism DRV in the α and β phases. The resulting subgrain size is larger at higher temperatures and slower strain rates. It is reported by Liss et al. [168] that a high rate of dynamic recovery and recrystallisation occurring within β grains makes the TNM alloy a suitable material for thermomechanical processing. The optimal processing window for TNM alloy is above the γ solvus due to the high amount of the good deformable β phase and the thermally active restoration processes.
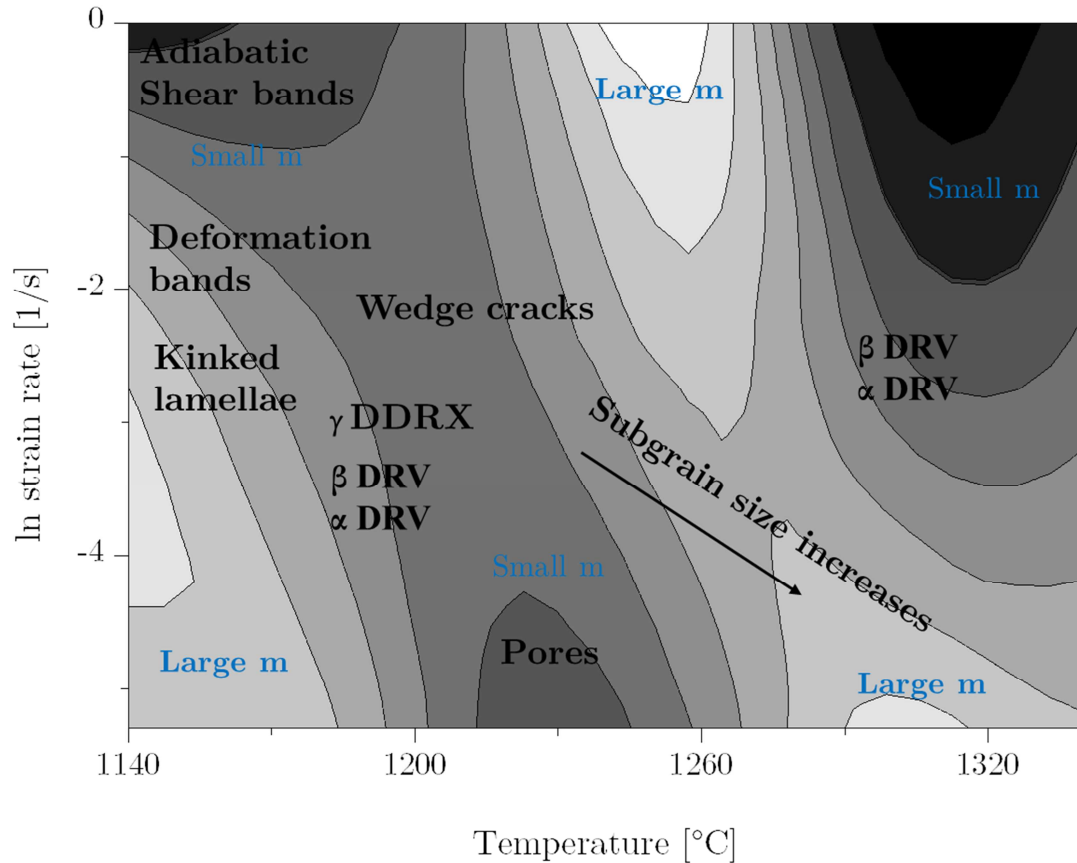
Figure 93: Overlapped microstructural, damage and m maps of the deformed specimens under the *slow cycle* after deformation at 0.9 of strain.

5.5 Discussion about methodology

5.5.1 Gleeble and FEM simulations

a) Gleeble

This sub-chapter provides an overview of the advantages and disadvantages of the use of Gleeble®3800 from a user perspective. One of the most important advantages is that the experiments can be carried out in-situ and nearly all gases, water or oil can be used for quenching. Although one further advantage of Gleeble consists in the fast heating rates, there is always a temperature gradient along the specimen which can be decreased by the use of metallic materials between the sample and the anvils. In this study many lubricant combinations were applied to reduce the friction effect and the temperature gradient, which result in barrelling. The friction effect and the temperature gradient were reduced. Moreover, the cooling is also very fast, but the stepwise cooling with water is difficult to control. Since the temperature measurement is performed locally at the surface, there is no information about the temperature inside the specimens.

b) FEM simulation and modelling

The FEM allowed the calculation of temperature, strain and strain rate distributions of the deformed specimens. It must be mentioned that the results of FEM simulation are strongly influenced by the material properties from the database.

The **flow behaviour** required to use DEFORM™ can be described by experimental flow curves or using a model. The problem when using experimental flow curves is that the "crossing curves" have to be corrected. Another problem faced by using experimental flow curves is that the automatical extrapolation in DEFORM™ is based only on the last two points of stress and strain.

The **modelling of stress** of the multi-phase material TiAl presents a set of challenges. One of the main difficulties in formulating a multi-phase stress model is the description of the phases and their plastic behaviour. Therefore in this work a semi empirical optimised model was developed. However, this semi-empirical model is mainly based on reproducing the thermomechanical experimental tests at different conditions. The prediction of flow stresses for unknown flow curves is limited and this is a main disadvantage of the semi empirical model. One of the advantages of the used model is that it makes possible to predict flow stresses at higher strains. The flow stress prediction up to high strains for the specimen deformed at 1140°C for several strain rates is shown in Figure 94. During deformation of TiAl several metallurgical processes occur such as dynamic restoration including recovery and recrystallisation, phase transformations and damage. The kinds of damage of the TNM alloy include wedge cracks, micro pores, shear bands, and surface connected cracks. During hot compression changes in the phase fraction or morphology occur and these changes are assumed to affect the softening behaviour of the material. The influence of those factors mentioned above cannot be distinguished. The relative softening maps show that the softening behaviour varies with different testing conditions. Therefore it is difficult to model the softening behaviour only due to the damage, because also restoration processes are also different at different testing conditions. At lower temperatures DRX is the dominant restoration mechanism and partially accompanied by DRV of the β and α phase. Another aspect is that the material was deformed under non phase equilibrium conditions. Therefore dynamic phase transformations should be also included. The challenge of the modelling of the used alloy is to sum all this dominating processes with varying intensities in one equation.
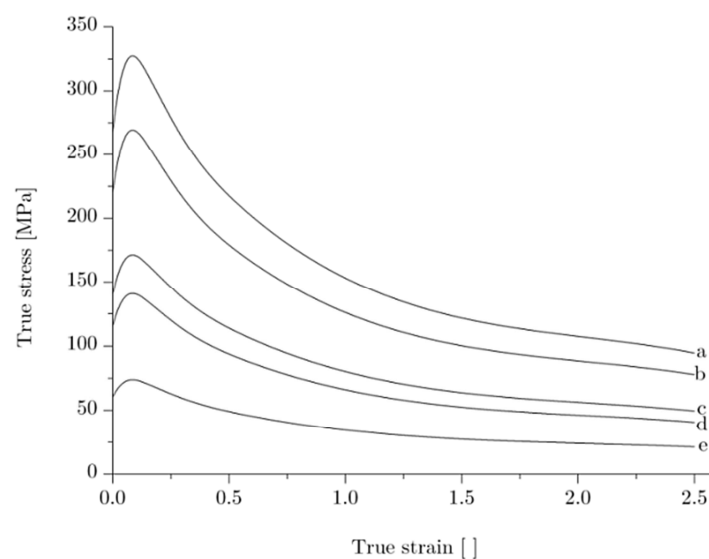
Figure 94: Flow curves modelled (*slow cycle*) for deformations at 1140°C with several strain rates (a) 1s⁻¹, (b) 0.5s⁻¹, (c) 0.1s⁻¹, (d) 0.05s⁻¹ and (e) 0.005s⁻¹.

5.5.2 EBSD

Due to its crystallographic nature, γ phase cannot be correctly indexed. Figures 95 show the orientation maps after (a) tetragonal and (b) face centred cubic indexed γ phase. In many research works the EBSD measurements are indexed as a fcc unit cell, but with this it does not enable a distinction between order variants. The tetragonal indexed IPF map shows differences from the cubic indexed ones. The fcc indexed IPF maps shows orientation differences in the same grain, while the fct indexed maps shows the same orientation for one grain, which is only due to the pseudo symmetry correction. In general the tetragonal indexed orientation maps should be used, because they show the correct reconstruction of the microstructure.
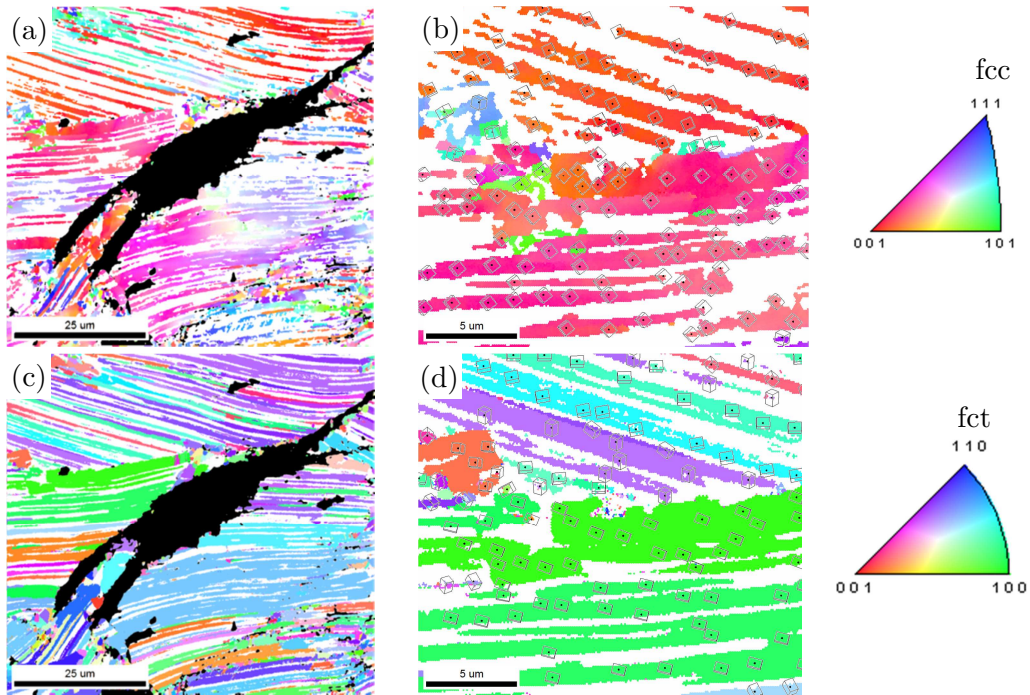
Figure 95: IPF maps of the specimen deformed at 1140°C, 1s^{-1} with (a), (b) face centred cubic and (c), (d) face centred tetragonal indexed.

6 Summary and Conclusions

In this study the hot deformation behaviour of a TiAl alloy was analysed. The hot deformation behaviour of such a brittle material is limited by ductile damage. The main focus was on characterising the damage behaviour under hot compression. The prediction of damage was performed by means of instability models based on DMM and a mechanical criterion by Semiatin and Jonas. Based on these investigations the purpose was to find the optimal processing window under different processing conditions, such as temperature and strain rate in which damage does not occur and homogeneous microstructural changes take place.

Based on **microstructural and damage investigations** it can be concluded that the softening behaviour of TNM alloy is due to a complex interaction of several dynamic processes. Damage is a response to strain localisation and thus, to multiaxial stress concentration, which increases fracture probability. Low temperatures and high strain rates exhibited flow instabilities such as wedge cracks, adiabatic shear bands, surface cracking, deformation bands and kinked lamellae due to tensile stresses. Low ability for restoration processes and adiabatic heating provoked flow localisations. Processing under moderate temperatures are characterised by wedge cracking and dynamic phase transformations, producing a strong decrease in flow stress. No flow localisation was found in the high temperature range and in comparison to low temperatures less cracks occurred at the bulged zone. High temperatures allow both, the activation of more slip systems and the formation of the β phase, which are good for the deformability. The stress can be released by restoration mechanism such as DRV of the β and α phases.

The cracks at the bulged area of the deformed specimens occur due to tensile stress condition during compression. Macro-crack formation depends on the temperature and strain rate: at higher temperatures together with lower strain rates the intensity for macro-crack formation decreases. The tips of the main cracks are areas with a high stress concentration and therefore new cracks were formed close to the tip of the main micro-crack. Cracks are generally located at the interface of γ globular and γ lamellae. No new cracks appear in the globular dynamic recrystallised γ phase. The cracks spread mainly in translamellar direction across the microstructure. However, in few specimens a combination of translamellar, interlamellar and intralamellar cracking is visible. Furthermore, pores and cracks nucleate beside the TiB particles, due to the dislocation pile-up.

The predictions of flow localisation, damage and instabilities were done by means of **DMM, α_{SJ}, m** and macromechanical damage models. The dissipation efficiency η_P by Prasad described exactly the thermomechanical behaviour of the material. The instability criterions based on DMM were not appropriate to predict instabilities due to the many controversies. The α_{SJ} is strongly dependent on the material and is related to strong softening, which is note caused by restoration mechanisms. For the analysed TNM alloy, when m is large, it was estimated that **$\alpha_{SJ}>3$** indicates high flow localisation, which is related to catastrophic failure and $0<\alpha_{SJ}<3$ predicts softening due to several other dynamic processes. The prediction of stable flow behaviour by means of α_{SJ} should be considered carefully, then the physical meanings of negative γ' or m should be questioned.

The behaviour of the material was described well with m. The predictions by m were in good correlation with the experimental observations. The physical meaning of m is well understood. Dynamic processes, which are diffusion controlled, are dependent on the strain rate, which results in high strain rate sensitivity. Negative m values were obtained due to strong flow localisation, damage or dynamic phase transformation.

7 Outlook

The methods used for analysis such as FEG-SEM and EBSD were very useful for the characterisation of damage, but a further method might be helpful for a three dimensional characterisation. In future X-ray computed tomography (XCT) should be used, because spatial mapping of cracks and pores will be useful for a deeper insight into the damage behaviour of the alloy. An even more detailed analysis is necessary to estimate crack shape and size. It should be determined, if there is a relation between the phase constitution and the crack size. The critical crack size, which would cause catastrophic failure, has to be determined.

The α_{SJ} parameter was used to predict flow localisation in the deformed specimens. One disadvantage of this parameter is that it just takes into account the actual values of strain rate, strain and temperature, but not the pre-history of the material. The λ parameter, which is the integration of $\alpha_{SJ}/\dot{\varepsilon}$ with respect to time, allows taking into account the history of the deformation. This parameter is independent of the complexity of the evolution of the processing parameters and is highly recommended to be used in future for the prediction of flow localisation.

Furthermore, a flow stress model should be developed, which concentrates on contrasting the physical mechanisms during deformation of the TNM alloy to empirical models. Physical based models provide a more accurate representation of the deformation behaviour. However, these models require a high experimental effort.

Another possibility is that in DEFORM a user subroutine can be used to implement an adequate extrapolation method. However, the huge amount of different material data requires time to find the optimal extrapolation model and this can be performed in future studies.

Another auspicious approach might be the improvement of processing maps, which should help to choose the optimal forming parameters such as strain rate, strain and temperature. A new model should be developed which is based on thermodynamics.

References

[1]   W. D. Dunfee, "Environmentally enhanced thermal fatigue and cracking of a gamma-based titanium aluminide alloy," Lehigh University, 1994.

[2]   A. Lasalmonie, "Intermetallics : Why is it so difficult to introduce them in gas turbine engines ?," *Intermetallics*, vol. 14, no. 10–11, pp. 1123–1129, 2006.

[3]   F. Appel and R. Wagner, "Microstructure and deformation of two-phase γ-titanium aluminides," *Mater. Sci. Eng. Reports A Rev. Journal, R22*, vol. 22, no. 5, pp. 187–268, 1998.

[4]   M. Peters and C. Leyens, *Titanium and Titanium Alloys*. Weinheim: Wiley-VCH Verlag GmbH & Co. KGaA, 2002.

[5]   D. M. Dimiduk, "Gamma titanium aluminide alloys—an assessment within the competition of aerospace structural materials," *Mater. Sci. Eng. A*, vol. 263, no. 2, pp. 281–288, 1999.

[6]   H. Y. Kim, W. H. Sohn, and S. H. Hong, "High temperature deformation of Ti–(46–48)Al–2W intermetallic compounds," *Mater. Sci. Eng. A*, vol. 251, no. 1–2, pp. 216–225, 1998.

[7]   F. Appel, J. D. H. Paul, and M. Oehring, *Gamma titanium aluminide alloys*. Weinheim, Germany: Wiley-VCH Verlag GmbH & Co. KGaA, 2011.

[8]   T. Tetsui, "A newly developed hot worked TiAl alloy for blades and structural components," *Scr. Mater.*, vol. 47, no. 6, pp. 399–403, 2002.

[9]   S. Knippscheer and G. Frommeyer, "Neu entwickelte TiAl-Basislegierungen für den Leichtbau von Triebwerks- und Motorkomponenten– Eigenschaften, Herstellung, Anwendung," *Materwiss. Werksttech.*, vol. 37, no. 9, pp. 724–730, 2006.

[10]   F. Appel, U. Lorenz, M. Oehring, U. Sparka, and R. Wagner, "Thermally activated deformation mechanisms in micro-alloyed two-phase titanium amminide alloys," *Mater. Sci. Eng. A*, vol. 233, pp. 1–14, 1997.

[11]   F. Appel, M. Oehring, and J. D. H. Paul, "A novel in situ composite structure in TiAl alloys," *Mater. Sci. Eng. A*, vol. 493, no. 1–2, pp. 232–236, 2008.

[12]   M. Takeyama and S. Kobayashi, "Physical metallurgy for wrought gamma titanium aluminides," *Intermetallics*, vol. 13, no. 9, pp. 993–999, 2005.

[13]   U. Hecht, V. Witusiewicz, A. Drevermann, and J. Zollinger, "Grain refinement by low boron additions in niobium-rich TiAl-based alloys," *Intermetallics*, vol. 16, no. 8, pp. 969–978, 2008.

[14]   G. L. Chen, W. J. Zhang, Z. C. Liu, S. J. Li, and J. W. Kim, "Microstructure and properties of high-Nb containing TiAl-base alloys," in *Gamma Titanium Aluminides 1999*, 1999.

[15]   T. T. Cheng, M. R. Willis, and I. P. Jones, "Effects of major alloying additions on the microstructure and mechanical properties of γ-TiAl," *Intermetallics*, vol. 7, no. 1, pp. 89–99, 1999.

[16]   G. Lütjering and J. C. Williams, *Titanium*. 2007.

[17]   P. Gardiner, H. Miguélez, R. Cortés, Y. Lepetitcorps, B. Dodd, and C. Navarro, "Dynamic characterization of TiAl intermetallic in hot compression," *J. Phys.*, vol. 3, no. 8, pp. 593–597, 1997.

[18] B. Zeumer, W. Wunnike-Sanders, and G. Sauthoff, "Mechanical properties and high-temperature deformation behaviour of particle-strengthened NiAl alloys," *Mater. Sci. Eng. A*, vol. 192–193, pp. 817–823, 1995.

[19] N. S. Stoloff, C. T. Liu, and S. C. Deevi, "Emerging applications of intermetallics," *Intermetallics*, vol. 8, pp. 1313–1320, 2000.

[20] G. Sauthoff, *Intermetallics*. Weinheim: VCH Verlagsgesellchaft mbH, 1995.

[21] Y. L. Hao, R. Yang, Y. Y. Cui, and D. Li, "The influence of alloying on the $\alpha_2/(\alpha_2+\gamma)/\gamma$ phase boundaries in TiAl based systems," *Acta Mater.*, vol. 48, no. 6, pp. 1313–1324, 2000.

[22] A. Menand, A. Huguet, and A. Nérac-Partaix, "Interstitial solubility in γ and α_2 phases of TiAl-based alloys.," *Acta Mater.*, 1996.

[23] J. C. Schuster and M. Palm, "Reassessment of the binary Aluminum-Titanium phase diagram," *J. Phase Equilibria Diffus.*, vol. 27, no. 3, pp. 255–277, 2006.

[24] D. Hu and R. R. Botten, "Phase transformations in some TiAl-based alloys," *Intermetallics*, vol. 10, no. 7, pp. 701–715, 2002.

[25] F. Appel, U. Brossmann, U. Christoph, S. Eggert, P. Janschek, U. Lorenz, J. Müllauer, M. Oehring, and J. D. H. Paul, "Recent progress in the development of gamma titanium aluminide alloys," *Adv. Eng. Mater.*, 2000.

[26] F. Appel and R. Wagner, "Microstructure and deformation of two-phase γ-titanium aluminides," *Mater. Sci. Eng. R Reports*, vol. 22, no. 97, pp. 187–268, 1998.

[27] M. J. Blackburn and M. P. Smith, "US patent," 1981.

[28] I. S. Jung, M. C. Kim, J. H. Lee, M. H. Oh, and D. M. Wee, "High temperature phase equilibria near Ti-50 at% Al composition in Ti-Al system studied by directional solidification," *Intermetallics*, vol. 7, no. 11, pp. 1247–1253, 1999.

[29] J. Lin, X. Xu, L. Zhang, Y. Lian, Y. Xu, and G. Hao, "Alloy design concepts for wrought high temperature TiAl alloys," in *TMS (The Minerals, Metals & Materials Society)*, 2014.

[30] B. J. Inkson, C. B. Boothroyd, and C. J. Humphreys, "Boride morphology in a (Fe, V, B) Ti-Al alloy containing B2-phase," *Acta Metall. Mater.*, vol. 43, no. 4, pp. 1429–1438, 1995.

[31] R. M. Imayev, V. M. Imayev, M. Oehring, and F. Appel, "Alloy design concepts for refined gamma titanium aluminide based alloys," *Intermetallics*, vol. 15, no. 4, pp. 451–460, 2007.

[32] D. K. Aspinwall, R. C. Dewes, and A. L. Mantle, "The machining of γ-TiAl intermetallic alloys," *CIRP Ann. Technol.*, vol. 11, no. 2, pp. 2–7, 2005.

[33] J. Lapin, "TiAl-based alloys: Present status and future," in *Metal 2009*, 2009, pp. 1–12.

[34] E. Schwaighofer, H. Clemens, S. Mayer, J. Lindemann, J. Klose, W. Smarsly, and V. Güther, "Microstructural design and mechanical properties of a cast and heat-treated intermetallic multi-phase γ-TiAl based alloy," *Intermetallics*, vol. 44, pp. 128–140, 2014.

[35] W. Wallgram, T. Schmölzer, L. Cha, G. Das, V. Güther, and H. Clemens, "Technology and mechanical properties of advanced γ-TiAl based alloys," *Int. J. Mater. Res.*, vol. 100, no. 8, pp. 1021–1030, 2009.

[36] M. Grujicic and Y. Zhang, "Crystal plasticity analysis of the effect of dispersed β-phase on deformation and fracture of lamellar γ+α₂ titanium aluminide," *Mater. Sci. Eng. A*, vol. 265, no. 1–2, pp. 285–300, 1999.

[37] V. Küstner, "Untersuchungen zur Gefügebildung bei der Erstarrung von γ - Titanaluminid-Legierungen unterschiedlicher Konstitution," Christian-Albrechts-Universität zu Kiel, Germany, 2003.

[38] A. Stark, "Textur- und Gefügeentwicklung bei der thermomechanischen Umformung Nb-reicher γ-TiAl-Basislegierungen," Hamburg University of Technology, 2010.

[39] R. J. Van Thyne, E. S. Bumps, H. D. Kessler, and M. Hansen, "Phase diagrams of the titanium-aluminum, titanium-chromium-iron, and titanium-oxygen alloy systems," Ohio, 1952.

[40] Z. C. Liu, J. P. Lin, S. J. Li, and G. L. Chen, "Effects of Nb and Al on the microstructures and mechanical properties of high Nb containing TiAl base alloys," *Intermetallics*, vol. 10, no. 7, pp. 653–659, 2002.

[41] J. Lapin and M. Nazmy, "Microstructure and creep properties of a cast intermetallic Ti-46Al-2W-0.5Si alloy for gas turbine applications," *Mater. Sci. Eng. A*, vol. 380, no. 1–2, pp. 298–307, 2004.

[42] P. R. Subramanian, M. G. Mendiratta, D. M. Dimiduk, and M. A. Stucke, "Advanced intermetallic alloys-beyond gamma titanium aluminides," *Mater. Sci. Eng. A*, vol. 239–240, pp. 1–13, 1997.

[43] C. T. Liu and P. J. Maziasz, "Microstructural control and mechanical properties of dual-phase TiAl alloys," *Intermetallics*, vol. 6, no. 98, pp. 653–661, 1998.

[44] K. S. Chan and Y. W. Kim, "Effects of lamellae spacing and colony size on the fracture resistance of a fully-lamellar TiAl alloy," *Acta Metall. Mater.*, vol. 43, no. 2, pp. 439–451, 1995.

[45] F. Iqbal, "Fracture mechanisms of γ-TiAl alloys investigated by in-situ experiments in a scanning electron and atomic force microscope," Technische Fakuktät der Universität Erlangen Nürnberg, 2012.

[46] F. Appel, M. Oehring, J. D. H. Paul, C. Klinkenberg, and T. Carneiro, "Physical aspects of hot-working gamma-based titanium aluminides," *Intermetallics*, vol. 12, no. 7–9, pp. 791–802, Jul. 2004.

[47] R. W. Evans, R. J. Hull, and B. Wilshire, "The effects of alpha-case formation on the creep fracture properties of the high-temperature titanium alloy IMI834," *J. Mater. Process. Technol.*, vol. 56, no. 1–4, pp. 492–501, 1996.

[48] W. J. Zhang, Z. C. Liu, G. L. Chen, and Y.-W. Kim, "Deformation mechanisms in a high-Nb containing γ–TiAl alloy at 900°C," *Mater. Sci. Eng. A*, vol. 271, pp. 416–423, 1999.

[49] G. L. Chen and L. C. Zhang, "Deformation mechanism at large strains in a high-Nb-containing TiAl at room temperature," *Mater. Sci. Eng. A*, vol. 329–331, no. 1–2, pp. 163–170, 2002.

[50] M. Ikebuchi, H. Inui, Y. Shirai, M. Yamaguchi, S. Fujita, and T. Nishisako, "Microstructures of some intermetallic compounds deformed by impact loading," *Mater. Sci. Eng. A*, vol. 192–193, pp. 289–300, 1995.

[51] D. Häussler, M. Bartsch, M. Aindow, I. P. Jones, and U. Messerschmidt, "Dislocation processes during the plastic deformation of γ-TiAl," *Philos. Mag. A*, vol. 79, no. 5, pp. 1045–1071, 1999.

[52] C. R. Zambaldi, "Micromechanical modeling of γ-TiAl based alloys," 2010.

[53] R. Porizek, S. Znam, D. Nguyen-Manh, V. Vitek, and D. G. Pettifor, "Atomistic studies of dislocation glide in γ-TiAl," *MRS Proc.*, vol. 753, 2002.

[54] R. v. Mises, "Mechanik der plastischen Formanderung von Kristallen," *Zeitschrift Angew. Math. und Mech.*, vol. 8, pp. 161–185, 1928.

[55] M. Kabir, "Modeling and simulation of deformation and fracture behavior of components made of fully lamellar gamma-TiAl alloy," GKSS-Forschungszentrum Geesthacht, 2008.

[56] U. Andrade, M. A. Meyers, K. S. Vecchio, and A. H. Chokshi, "Dynamic recrystallization in high-strain, high-strain-rate plastic deformation of copper," *Acta Metall. Mater.*, vol. 42, no. 9, pp. 3183–3195, 1994.

[57] M. R. Drury and J. L. Urai, "Deformation-related recrystallization processes," *Tectonophysics*, vol. 172, pp. 235–253, 1990.

[58] R. D. Doherty, D. A. Hughes, F. J. Humphreys, J. J. Jonas, D. J. Jensen, M. E. Kassner, W. E. King, T. R. McNelley, H. J. McQueen, and A. D. Rollett, "Current issues in recrystallization: a review," *Mater. Sci. Eng. A*, vol. 238, no. 2, pp. 14–15, 1997.

[59] F. J. Humphreys and M. Hatherly, *Recrystallization and related annealing phenomena*, 2nd ed. Pergamon Press, 2003, p. 628.

[60] G. Gottstein, *Physikalische Grundlagen der Materialkunde.* 2007.

[61] H. J. McQueen and W. Blum, "Dynamic recovery: sufficient mechanism in the hot deformation of Al (< 99.99)," *Mater. Sci. Eng. A*, vol. 290, no. 1–2, pp. 95–107, 2000.

[62] R. D. Doherty, D. A. Hughes, F. J. Humphreys, J. J. Jonas, D. Juul Jensen, M. E. Kassner, W. E. King, T. R. McNelley, H. J. McQueen, and A. D. Rollett, "Current issues in recrystallization: A review," *Mater. Today*, vol. 1, no. 2, pp. 14–15, 1998.

[63] A. A. Hameda and L. Blaz, "Flow softening during hot comoression of Cu-3.45 wt.% Ti alloy," *Scr. Mater.*, vol. 37, no. 12, pp. 1987–1993, 1997.

[64] S. Gourdet and F. Montheillet, "An experimental study of the recrystallization mechanism during hot deformation of aluminium," *Mater. Sci. Eng. A*, vol. 283, pp. 274–288, 2000.

[65] F. Montheillet, "Dynamic recrystallization: classical concepts and new aspects," *Rev. Métallurgie*, vol. 99, no. 3, pp. 767–776, 2002.

[66] A. Belyakov, H. Miura, and T. Sakai, "Dynamic recrystallization under warm deformation of a 304 type austenitic stainless steel," *Mater. Sci. Eng. A*, vol. 255, no. 1–2, pp. 139–147, 1998.

[67] W. Gao, A. Belyakov, H. Miura, and T. Sakai, "Dynamic recrystallization of copper polycrystals with different purities," *Mater. Sci. Eng. A*, vol. 265, no. 1–2, pp. 233–239, 1999.

[68] D. Ponge and G. Gottstein, "Necklace formation during dynamic recrystallization: mechanisms and impact on flow behavior," *Acta Mater.*, vol. 46, no. 1, pp. 69–80, 1998.

[69]   E. I. Poliakt and J. J. Jonas, "A one-parameter approach to determining the critical conditions for the initiation of dynamic recrystallization," *Acta Metall. Inc.*, vol. 44, no. 1, pp. 127–136, 1996.

[70]   H. J. McQueen, "Development of dynamic recrystallization theory," *Mater. Sci. Eng. A*, vol. 387–389, pp. 203–208, 2004.

[71]   A. Belyakov, H. Miura, and T. Sakai, "Dynamic recrystallization in ultra fine-grained 304 stainless steel," *Scr. Mater.*, vol. 43, no. 1, pp. 21–26, 2000.

[72]   R. A. N. M. Barbosa, "Simulation of hot working of austenitic stainless steels," University of Sheffield, 1983.

[73]   J. Biglou, "Dynamic recrystallization during strip rolling of HSLA steels and prediction of roll forces using artificial neural networks," University of Waterloo, 1997.

[74]   T. Sakai, A. Belyakov, R. Kaibyshev, H. Miura, and J. J. Jonas, "Dynamic and post-dynamic recrystallization under hot, cold and severe plastic deformation conditions," *Prog. Mater. Sci.*, vol. 60, pp. 130–207, 2014.

[75]   S. Gourdet and F. Montheillet, "A model of continuous dynamic recrystallization," *Acta Mater.*, vol. 51, no. 9, pp. 2685–2699, 2003.

[76]   S. L. Semiatin, V. Seetharaman, and I. Weiss, "Hot workability of titanium and titanium aluminide alloys-an overview," *Mater. Sci. Eng. A*, vol. 243, no. 1–2, pp. 1–24, Mar. 1998.

[77]   A. Needleman, "Continuum mechanics studies of plastic instabilities," *Rev. Phys. Appliquée*, vol. 23, no. 4, pp. 585–593, 1988.

[78]   S. V Kailas, Y. V. R. K. Prasad, and S. K. Biswas, "Flow instabilities and fracture in Ti-6AI-4V deformed in compression at 298 K to 673 K," vol. 25, no. 10, pp. 2173–2179, 1994.

[79]   S. V. S. N. Murty and B. N. Rao, "On the flow localization concepts in the processing maps of titanium alloy Ti -24Al -20Nb," *J. Mater. Process. Te*, vol. 104, no. 1–2, pp. 103–109, 2000.

[80]   M. Thlrukkonda, R. Srinlvasan, and I. Weiss, "Instability and flow localization during compression of a flow softening material," *J. Mater. Eng. Perform.*, vol. 3, no. 4, pp. 514–526, 1994.

[81]   T. W. Wright, *The physics and mathematics of adiabatic shear bands*. 2002.

[82]   J. A. Hines and K. S. Vecchio, "Recrystallization kinetics within adiabatic shear bands," *Acta Mater.*, vol. 45, no. 2, pp. 635–649, 1997.

[83]   R. C. Batra, "The initiation and growth of, and the interaction among, adiabatic shear bands in simple and dipolar materials," *Int. J. Plast.*, vol. 3, pp. 75–89, 1987.

[84]   D. Rittel and S. Osovski, "Dynamic failure by adiabatic shear banding," *Int. J. Fract.*, vol. 162, no. 1–2, pp. 177–185, 2010.

[85]   W. S. Lee and C. F. Lin, "Adiabatic shear fracture of titanium alloy subjected to high strain rate and high temperature loadings," *Le J. Phys. IV*, vol. 07, no. C3, pp. 855–860, 1997.

[86]   S. L. Semiatin, V. Seetharaman, and I. Weiss, "Hot workability of titanium and titanium aluminide alloys-an overview," *Mater. Sci. Eng. A*, vol. 243, no. 1–2, pp. 1–24, 1998.

[87]   S. L. Semiatin and J. J. Jonas, *Formability and workability of metals, plastic instability and flow localization*. Ohio: American Society for Metals, Metals Park, 1984.

[88]   J. W. Rudnicki and J. R. Rice, "Conditions for the localization of deformation in pressure-sensitive dilatant materials," *J. Mech. Phys. Solids*, vol. 23, no. 1970, pp. 371–394, 1975.

[89]   M. Cai and S. C. Langford, "Determination of strain localization in aluminum alloys using laser-induced photoelectron emission," vol. 96, no. 12, pp. 7189–7194, 2004.

[90]   E. N. Borodin and A. E. Mayer, "Localization of plastic deformation and mechanical twinning in dynamical channel angular pressing," *IOP Conf. Ser. Mater. Sci. Eng.*, vol. 63, 2014.

[91]   R. Colás Ortiz, "High strain rate, high temperature deformation of stainless steel," 1983.

[92]   J. H. Hollomon, "Tensile deformation," *Trans. AIME*, vol. 162, pp. 268–290, 1945.

[93]   P. Ludwik, *Elemente der technologischen Mechanik*. Julius Springer, 1909.

[94]   E. Voce, "The relationship between stress and strain for homogeneous deformation," *J. Int. Met.*, no. 1948, pp. 537–562, 2005.

[95]   G. Johnson and W. Cook, "A constitutive model and data for metals subjected to large strains, high strain rates and high temperatures," in *Proceedings of the 7th international symposium on ballistics*, 1983, pp. 541–547.

[96]   B. Bonora and E. Brown, *Numerical modeling of materials under extreme conditions*. 2014.

[97]   D. Samantaray, S. Mandal, A. K. Bhaduri, S. Venugopal, and P. V. Sivaprasad, "Analysis and mathematical modelling of elevated temperature flow behaviour of austenitic stainless steels," *Mater. Sci. Eng. A*, vol. 528, no. 4–5, pp. 1937–1943, 2011.

[98]   D. Umbrello, "Finite element simulation of conventional and high speed machining of Ti6Al4V alloy," *J. Mater. Process. Technol.*, vol. 196, no. 1–3, pp. 79–87, 2008.

[99]   D. Umbrello, R. M'Saoubi, and J. C. Outeiro, "The influence of Johnson-Cook material constants on finite element simulation of machining of AISI 316L steel," *Int. J. Mach. Tools Manuf.*, vol. 47, no. 3–4, pp. 462–470, 2007.

[100] M. Sasso, G. Newaz, and D. Amodio, "Material characterization at high strain rate by Hopkinson bar tests and finite element optimization," *Mater. Sci. Eng. A*, vol. 487, no. 1–2, pp. 289–300, 2008.

[101] M. Sima and T. Özel, "Modified material constitutive models for serrated chip formation simulations and experimental validation in machining of titanium alloy Ti-6Al-4V," *Int. J. Mach. Tools Manuf.*, vol. 50, no. 11, pp. 943–960, 2010.

[102] R. Liang and A. S. Khan, "A critical review of experimental results and constitutive models for bcc and fcc metals over a wide range of strain rates and temperatures," *Int. J. Plast.*, vol. 15, no. 9, pp. 963–980, 1999.

[103] M. Calamaz, D. Coupard, and F. Girot, "Numerical simulation of titanium alloy dry machining with a strain softening constitutive law," *Mach. Sci. Technol.*, vol. 14, no. 2, pp. 244–257, 2010.

[104] M. Calamaz, D. Coupard, and F. Girot, "A new material model for 2D numerical simulation of serrated chip formation when machining titanium alloy Ti–6Al–4V," *Int. J. Mach. Tools Manuf.*, vol. 48, no. 3–4, pp. 275–288, 2008.

[105] T. Özel and M. Sima, "Finite element simulation of high speed machining Ti-6Al-4V alloy using modifie material models," *Trans. NAMRI/SME*, vol. 38, pp. 49–56, 2010.

[106] D. Samantaray, S. Mandal, and a. K. Bhaduri, "A comparative study on Johnson Cook, modified Zerilli-Armstrong and Arrhenius-type constitutive models to predict elevated temperature flow behaviour in modified 9Cr-1Mo steel," *Comput. Mater. Sci.*, vol. 47, no. 2, pp. 568–576, 2009.

[107] W. K. Rule and S. E. Jones, "A revised form for the johnson–cook strength model," *Int. J. Impact Eng.*, vol. 21, no. 8, pp. 609–624, 1998.

[108] C. M. Sellars and W. J. M. Tegart, "On the mechanism of hot deformation," *Acta Metall. Inc.*, 1966.

[109] E. Schwaighofer, H. Clemens, J. Lindemann, A. Stark, and S. Mayer, "Hot-working behavior of an advanced intermetallic multi-phase γ-TiAl based alloy," *Mater. Sci. Eng. A*, vol. 614, pp. 297–310, 2014.

[110] H. J. Frost and M. F. Ashby, "Deformation-mechanism maps: the plasticity and creep of metals and ceramics," Pergamon Press, 1982.

[111] R. Raj, "Development of a processing map for use in warm-forming and hot-forming processes," *Metall. Mater. Trans. A*, vol. 12, pp. 1089–1097, 1981.

[112] Y. V. R. K. Prasad, H. L. Gegel, S. M. Doraivelu, J. C. Malas, J. T. Morgan, K.A. Lark, and D. R. Barker, "Modeling of dynamic material behavior in hot deformation : forging of Ti-6242," *Metall. Trans. A*, vol. 15, no. 10, pp. 1883–1892, 1984.

[113] F. Montheillet, J. J. Jonas, and K. W. Neale, "Modeling of dynamic material behavior: a critical evaluation of the dissipator power co-content approach," *Metall. Mater. Trans. A*, vol. 27, no. 1, pp. 232–235, 1996.

[114] S. Ghosh, "Interpretation of microstructural evolution using dynamic materials modeling," *Metall. Mater. Trans. A*, vol. 31, no. 11, pp. 2973–2974, 2000.

[115] S. Ghosh, "Interpretation of flow instability using dynamic material modeling," *Metall. Mater. Trans. A*, vol. 33, no. 5, pp. 1569–1572, 2002.

[116] B. Bozzini and E. Cerri, "Numerical reliability of hot working processing maps," *Mater. Sci. Eng. A*, vol. 328, no. 1–2, pp. 344–347, 2002.

[117] S. Venugopal and P. V Sivaprasad, "A journey with Prasad's processing maps," *J. Mater. Eng. Perform.*, vol. 12, no. 6, pp. 674–686, 2003.

[118] P. E. Wellstead, *Introduction to physical system modelling*. Prentice Hall, 1969.

[119] Y. V. R. K. Prasad and S. Sasidhara, *Hot working guide: a compendium of processing maps*. ASM International, 1997.

[120] L. E. Malvern, *Introduction to the mechanics of a continuous medium*. Prentice-Hall INC., 1977.

[121] S. V. S. N. Murty and B. N. Rao, "Ziegler 's criterion on the instability regions in processing maps," *J. Mater. Sci. Lett.*, vol. 17, no. 14, pp. 1203–1205, 1998.

[122] N. Srinivasa and Y. V. R. K. Prasad, "Hot working characteristics of nimonic 75, 80A and 90 superalloys: a comparison using processing maps," *J. Mater. Process. Technol.*, vol. 51, no. 1–4, pp. 171–192, 1995.

[123] S. V. S. N. Murty and B. N. Rao, "On the development of instability criteria during hotworking with reference to IN 718," *Mater. Sci. Eng. A*, vol. 254, no. 1–2, pp. 76–82, 1998.

[124] S. V. S. N. Murty and B. N. Rao, "On the flow localization concepts in the processing maps of IN718," *Mater. Sci. Eng. A*, vol. 267, no. 1, pp. 159–161, 1999.

[125] H. Ziegler, "Some extremum principles in irreversible thermodynamics with application to continuum mechanics," *Prog. Solid Mech.*, 1966.

[126] L. Briottet, J. J. Jonas, and F. Montheillet, "A mechanical interpretation of the activation energy of high temperature deformation in two phase materials," *Acta Mater.*, vol. 44, no. 4, pp. 1665–1672, 1996.

[127] Y. V. R. K. Prasad, "Processing maps : A status report," *J. Mater. Eng. Perform.*, vol. 12, no. 6, pp. 638–645, 2003.

[128] C. Poletti, S. Großeiber, S. Llie, and H. P. Degischer, "Hot deformation behaviour of low alloyed steel," *Mater. Sci. Forum*, vol. 706–709, pp. 2794–2799, 2011.

[129] K. P. Rao, Y. V. R. K. Prasad, and K. Suresh, "Hot working behavior and processing map of a γ-TiAl alloy synthesized by powder metallurgy," *Mater. Des.*, vol. 32, no. 10, pp. 4874–4881, 2011.

[130] B. Liu, Y. Liu, Y. P. Li, W. Zhang, and A. Chiba, "Thermomechanical characterization of β-stabilized Ti–45Al–7Nb–0.4W–0.15B alloy," *Intermetallics*, vol. 19, no. 8, pp. 1184–1190, 2011.

[131] J. H. Kim, Y. W. Chang, C. S. Lee, and T. Kwon Ha, "High-temperature deformation behavior of a gamma TiAl alloy—Microstructural evolution and mechanisms," *Metall. Mater. Trans. A*, vol. 34, no. 10, pp. 2165–2176, 2003.

[132] G. Wang, L. Xu, Y. Wang, Z. Zheng, Y. Cui, and R. Yang, "Processing maps for hot working behavior of a PM TiAl alloy," *J. Mater. Sci. Technol.*, vol. 27, no. 10, pp. 893–898, 2011.

[133] A. Considère, *Mémoire sur l'emploi du fer et de l'acier dans les constructions.* Annales des Ponts et Chaussées, 1885, pp. 874–775.

[134] K. T. Ramesh, *Nanomaterials: Mechanics and Mechanisms.* 2009, pp. 184–188.

[135] R. E. Smallman and R. J. Bisho, *Modern physical metallurgy and materials engineering.* Butterworth-Heinemann, 1999.

[136] E. W. Hart, "Theory of the tensile test," *Acta Metall. Inc.*, vol. 15, no. 2, pp. 351–355, 1967.

[137] J. Hoffmann, V. H. Vazquez, C. Santiago-vega, and T. Altan, "Prediction of ductile fracture in forward extrusion with spherical dies," *Trans. NAMRI/SME*, vol. XXVIII, pp. 57–62, 2000.

[138] J. Lemaitre and R. Desmorat, *Engineering Damage Mechanics.* Berlin/Heidelberg: Springer-Verlag, 2005, pp. 1–380.

[139] C. M. Sellars and W. J. M. Tegart, "Hot workability," *Int. Metall. Rev.*, vol. 17, pp. 1–24, 1972.

[140] M. G. Cockcroft and D. J. Latham, "Ductility and the workability of metals," *J. Inst. Met.*, vol. 96, pp. 33–39, 1968.

[141] A. Freudenthal, *The inelastic behaviour of engineering metals and structures.* 1950.

[142] P. Brozzo, B. DeLuca, and R. Rendina, "A new method for the prediction of formability limits in metal sheets," in *7th conference of the international deep drawing research group*, 1972.

[143] T. Ayada, K. Higashino, and K. Mori, "Central bursting in extusion of inhomogeneous materials," in *Proceedings of the 1st international conference on technology of plasticity*, 1984.

[144] W. Brocks, S. Hao, and D. Steglich, "Micromechanical modelling of the damage and toughness behaviour of nodular cast iron materials," *Le J. Phys. IV*, vol. 06, no. C6, pp. C6–43–C6–52, 1996.

[145] D. Halici and C. Poletti, "Flow localization modelling in Ti alloys and Ti matrix composites," *Key Eng. Mater.*, vol. 653, pp. 3–8, 2015.

[146] K. H. Huebner, D. L. Dewhirst, D. E. Smith, and T. G. Byrom, *The finite element method for engineers.* 2001.

[147] M. Shirgaokar, G. Ngaile, and G. Shen, "Process modeling in impression-die forging using finite-element analysis," *ASTM Int. Cold Hot Forg. Fundam. Appl.*, vol. 5104, pp. 193–200, 2005.

[148] T. Altan and V. Vazquez, "Status of process simulation using 2D and 3D finite element method 'What is practical today? What can we expect in the future," vol. 71, no. 1, pp. 49–63, 1997.

[149] L. Schaeffer, A. M. G. Brito, and Geier M., "Numerical simulation using finite elements to develop and optimize forging processes," *Steel Res. Int.*, vol. 76, no. 2/3, pp. 199–204, 2005.

[150] J. Seeger, J. Klein, and H. Mecking, "Farbmetallographie an den intermetallischen Phasen γ-TiAl und α_2-Ti$_3$Al," *Prakt. Metallogr.*, 1990.

[151] N. Yao and Z. L. Wang, *Handbook of microscopy for nanotechnology.* 2006.

[152] Y. B. Zhang, A. Elbrønd, and F. X. Lin, "Materials Characterization A method to correct coordinate distortion in EBSD maps," *Mater. Charact.*, vol. 96, pp. 158–165, 2014.

[153] Z. Chen, Y. Yang, and H. Jiao, "Some applications of tlectron back scattering diffraction (EBSD) in materials research," *Scan. Electron Microsc.*, p. 830, 2012.

[154] F. J. Humphreys, M. Materials, and S. Centre, "Grain and subgrain characterisation by electron backscatter diffraction," vol. 6, pp. 3833–3854, 2001.

[155] C. Zambaldi, S. Zaefferer, and S. I. Wright, "Characterization of order domains in gamma-TiAl by orientation microscopy based on electron backscatter diffraction," *J. Appl. Crystallogr.*, vol. 42, no. 111, pp. 1092–1101, 2009.

[156] "http://imagej.net," 2012 [viewed 2013].

[157] M. Kreimer, "Warmumformung von einer TNM-Legierung," Technical University of Graz, 2013.

[158] DSI Systems, *Gleeble users training 2013® Gleeble systems and applications.* 2013.

[159] K. Thayalan, *The Physics of radiology and imaging.* 2014.

[160] J. Zhang, H. Di, X. Wang, Y. Cao, J. Zhang, and T. Ma, "Constitutive analysis of the hot deformation behavior of Fe–23Mn–2Al–0.2C twinning induced plasticity steel in consideration of strain," *Mater. Des.*, vol. 44, pp. 354–364, 2013.

[161] G. Chen, C. Ren, W. Yu, X. Yang, and L. Zhang, "Application of genetic algorithms for optimizing the Johnson-Cook constitutive model parameters when simulating the titanium alloy Ti-6Al-4V machining process," in *Proceedings of the Institution of Mechanical Engineers, Part B: Journal of Engineering Manufacture*, 2012, vol. 226, pp. 1287–1297.

[162] J. Fluhrer, *DEFORM Manual*, no. 614. pp. 1–288.

[163] Böhler Schmiedetechnik GmbH & Co KG, "Material information," 2012.

[164] D. Prodinger, "Untersuchung der Schädigung der γ-TiAl TNM-Legierung während der Warmverformung," Technical University of Graz, 2014.

[165] H. Clemens, H. F. Chladil, W. Wallgram, G. A. Zickler, R. Gerling, K. D. Liss, S. Kremmer, V. Güther, and W. Smarsly, "In and ex situ investigations of the β-phase in a Nb and Mo containing γ-TiAl based alloy," *Intermetallics*, vol. 16, no. 6, pp. 827–833, 2008.

[166] S. Bolz, M. Oehring, J. Lindemann, F. Pyczak, J. Paul, A. Stark, T. Lippmann, S. Schrüfer, D. Roth-Fagaraseanu, A. Schreyer, and S. Weiß, "Microstructure and mechanical properties of a forged β-solidifying γ TiAl alloy in different heat treatment conditions," *Intermetallics*, vol. 58, pp. 71–83, 2015.

[167] U. Fröbel and F. Appel, "Hot-workability of gamma-based TiAl alloys during severe torsional deformation," *Metall. Mater. Trans. A Phys. Metall. Mater. Sci.*, vol. 38, pp. 1817–1832, 2007.

[168] H. Inui, K. Kishida, M. Misaki, M. Kobayashi, Y. Shirai, and M. Yamaguchi, "Temperature dependence of yield stress, tensile elongation and deformation structure in PST crystals of TiAl," *Phil. Mag. A*, vol. 72, pp. 1609–1631, 1995.

[169] J. Lia, Y. Liua, B. Liua, Y. Wangb, X. Lianga, and Y. Hea, "Microstructure characterization and mechanical behaviors of a hot forged high Nb containing PM-TiAl alloy," *Mater. Charact.*, vol. 95, pp. 148–156, 2014.

[170] M. Dao, B. K. Kad, and R. J. Asaro, "Deformation and fracture under compressive loading in lamellar TiAl microstructures.," *Philos. Mag. A*, vol. 74, no. 3, pp. 569–591, 1996.

[171] P. K. Sagar, D. Banerjee, and Y. V. R. K. Prasad, "Unstable flow during hot deformation of Ti-24AI-20Nb alloy," *Mater. Sci. Technol.*, vol. 13, pp. 755–760, 1997.

[172] D. Halici, D. Prodinger, C. Poletti, D. Huber, M. Stockinger, and C. Sommitsch, "Modelling of the ductile damage behaviour of a beta solidifying gamma titanium aluminide alloy during hot-working," in *Materials Science Forum*, 2014, pp. 556–561.

[173] D. Halici, H. A. Zamani, D. Prodinger, C. Poletti, D. Huber, M. Stockinger, and C. Sommitsch, "Studies on ductile damage and flow instabilities during hot deformation of a multiphase γ-TiAl alloy," in *Key engineering materials*, 2014, pp. 99–105.

[174] M. Dikovits, "Study of the hot deformation behaviour of metal-based alloys under consideration of processing maps," Technical University of Graz, 2014.